Imperial College London

THEORY OF SURFACE MODES IN STRUCTURED PLASMONIC ARRAYS

John Jesse Wood

Thesis submitted for the degree of Doctor of Philosophy

Condensed Matter Theory Department

Blackett Laboratory

Department of Physics

Imperial College London

December 2015

Statement of originality

I, John Jesse Wood, state that the work and ideas presented in this thesis are the result of my individual endeavours during my PhD studies at Imperial College London. To the best of my knowledge, the results herein constitute original work except where otherwise referenced within the thesis itself. The thesis has not previously been submitted for the completion of higher degree at any other university.

Abstract

Metamaterials can provide many different functionalities and striking optical properties, whereby the optical control often comes from metallic building blocks which exhibit plasmonic resonances in the optical and infra-red frequency regimes. However, one of the major obstacles in the use of metallic elements is the overcoming of the losses in plasmonic structures. In this thesis, we consider how mode hybridisation can be used to circumvent these losses using cut-wire plasmonic arrays coupled to photonic slab waveguides. The resulting hybrid modes can have low loss characteristics and we investigate how the geometric parameters of the structure can be used to control the transmission and dispersion properties. We then investigate finite arrays finding they can support modes with extremely high quality factors (Q$\sim$ 4000), which is highly unusual in plasmonic systems, and that the individual loss mechanisms can be controlled via the geometry.

In the second part of the thesis we consider another type of surface mode, the spoof SPP. Theoretical methods for describing spoof SPPs in perfectly conducting materials are well established, enabling the design of an arbitrary spoof plasma frequency. However, for dispersive materials there have been a lack of theoretical studies. We begin by considering first how small changes to the spoof plasmon geometry affect the characteristics of spoof SPP waves, adapting the coupled mode method to slanted geometries and even right-angled triangular indentations, a structure not normally associated with spoof SPPs. We then develop a formalism based on the coupled mode method allowing the dispersion of real metal spoof SPPs to be understood and tuned, thus enabling control of the optical spoof SPP characteristics via both the geometry and the incorporated materials. This method also enables an in depth look at the modal losses which occur once dispersive materials are incorporated into the spoof plasmon dispersion relation and vary drastically with the groove width.

Acknowledgments

Firstly I would like to thank Professor Ortwin Hess for the opportunity of studying for my PhD within his research group at Imperial College London. His professional and personal support throughout the PhD has been invaluable and I will always be grateful to him.

I am indebted to Joachim Hamm with whom I worked closely on the first part of my project and who provided ideas, support and technical knowledge.

I am very grateful to Sang Soon Oh for his continued support over the second part of my project. His help, feedback and expertise have been invaluable. I would also like to thank Sang Soon specifically for providing the FDTD simulations that form the basis of the comparison to theory of figures 6.4 and 6.11.

I would like to thank Joachim, Sang Soon, Andreas Pusch and Fouad Ballout for proof reading my thesis and providing me with valuable feedback.

My particular thanks go to Rupert Oulton and Lucas Lafone for their collaboration on the first part of my thesis where they contributed ideas, discussion and help with the writing of our paper in scientific reports.

I am very grateful to Antonio Fernandez-Dominguez who introduced me to plasmonics during my masters project and gave me the opportunity to write my first paper.

Other than the people mentioned above, I am also grateful to Doris Reiter, Angela Demetriadou, Sebastian Wuestner, Tim Pickering, Zeph Davies, Fabian Renn, Freddie Page and Ollie Curtin for making the research group a warm and friendly place.

Now I would like to give thanks to my office-mates; Tim, Zeph, Tristan, James, Freddie, Fabian, Ollie, Peter and Joel. The interesting discussions, coffee breaks and social outings were a constant source of merriment throughout my PhD. I would also like to thank Fouad, Andreas, Seb, Paulo, Peter and Joel for being part of the triumphant CMTH football team; and Lee and Carlos for their

help with organising the weekly football events and post-graduate tournaments. Finally, Stefano, Andreas, Doris and James have my thanks for our weekly boardgame evenings.

Finally I would like to thank my family and friends. Sue and Nick for their constant support in all of my endeavors. To Granny, Hilary and Lakota for always supporting and encouraging me in their own way. My Uncle Paul for lecturing me on the importance of the scientific method, and, in particular, endowing me with the ability to identify a stick from a boomerang. To Gabriel, Sophie, James, Mandy, Olly and Helen; for putting up with my complaining over these last 4 years. To Danny and Frank for being the best of brothers, and in particular for showing me that plasmonsters can't dance.

Of course, I am also indebted to Yuko, whose love, support and drive continues to bring joy to my life.

Contents

List of Figures

List of Tables

List of Abbreviations

c	Speed of light in vacuum
ε_0	Vacuum permittivity
μ_0	Vacuum permeability
CDA	Coupled dipole approximation
CMM	Coupled mode method
CMTH	Condensed matter theory
CROW	Coupled resonator optical waveguide
EBL	Electron beam lithography
EIT	Electromagnetically induced transparency
EM	Electromagnetic
EOT	Extraordinary optical transmission
FBZ	First Brillouin zone
FDTD	Finite difference time domain
FEM	Finite element method
FWHM	Full width half maximum
IR	Infra-red
LSPR	Localised surface plasmon resonance

MIM Metal-insulator-metal

PEC Perfect electric conductor

SIBC Surface impedance boundary condition

SPP Surface plasmon polariton

TE Transverse electric

THz Terahertz

TM Transverse magnetic

WPP Waveguide plasmon polariton

1 Introduction

Throughout the 20^{th} century the development of the telecommunications industry has caused a growing interest from the scientific community in electromagnetic (EM) surface waves. The works of Sommerfeld [1] and Zenneck [2] just over 100 years ago demonstrated the propagation of guided EM waves along the surface of wires with finite conductivity. Around the same time Wood [3] demonstrated the appearance of dips in the intensity of the spectra of diffraction gratings (the Wood's anomaly) but it was not until 1941 that this phenomenon was connected with the prior theoretical work of Zenneck and Sommerfeld [4]. In the 1950s, plasma losses in thin metal films, much increased over the losses in thick metal films, were explained by Ritchie [5] as a consequence of the excitation of surface waves; which was then confirmed experimentally [6]. At the same time, the excitation of the Sommerfeld's surface wave was demonstrated using prism coupling with visible light [7] and thus the EM phenomena of these works were unified with the description of surface plasmon polaritons (SPPs) giving birth to the field of plasmonics.

SPPs are surface waves that exist at the interface between a conductor and a dielectric and have several interesting features. The high confinement of the EM energy to this interface enables large field enhancements on a sub-wavelength scale, whilst the waves can propagate along the interface for several hundred wavelengths [8]. Since SPPs arise in conductors due to the collective oscillations of the free electrons they constitute a hybrid light-matter wave, providing an avenue to combine both photonic and electronic elements within the same platform. As technology is advancing, electronic devices are fast approaching the fundamental limits of speed and bandwidth, and a substantial effort is being made to try and circumnavigate these. One potential solution is the use of photonic circuitry, whereby propagating EM waves are converted into SPPs, processed using SPP based logic devices and converted back into EM waves. In other words, SPPs could be used to provide the functionality of optical circuits through SPP-based photonics [9].

Over the last 15 years the study of metamaterials has emerged as a new sub-field of physics. The metamaterial paradigm asserts that by incorporating structure and design into the arrangement of material building blocks we can create new materials with properties that are unattainable for the composite parts alone. For instance, the pioneering work of John Pendry in this field has demonstrated materials with negative magnetic responses [10], and explorations of negative index devices enabling perfect lensing [11] and cloaking [12]. The creation of metamaterials at optical and infra-red (IR) frequencies has often involved plasmonic materials as meta-atom building blocks due to their strong interaction with light. This has directly led to the consideration of structural design in plasmonic research. As early as 1998 Ebbesen and co-workers demonstrated the extraordinary optical transmission phenomena through a plasmonic metamaterial [13], leading to a thorough examination, both theoretical and experimental of the surface modes that were supported by the 2D array of holes [14]. Amongst other things, the electromagnetic modes of wire arrays [15], particle arrays [16] and stacked fishnet structures [17] have been explored demonstrating negative index materials [18] and enhanced electromagnetic fields useful for sensing applications [19, 20].

In this thesis, we continue this exploration of electromagnetic surface modes supported on structured plasmonic arrays. The thesis is split into three main parts. In the first part (chapter 2) the relevant fundamental concepts of EM theory are reviewed, including Maxwell's equations, SPPs and waveguide modes. We also cover some of the methods used throughout the thesis, including finite element and finite difference time domain numerical methods.

One of the major challenges in plasmonics, particularly for photonic circuitry applications, is overcoming the losses that accompany surface plasmon modes. One way of overcoming the losses is the incorporation of gain materials into the system, thereby compensating for the losses at source [21, 22]. Another way; investigated in the second part of this thesis, is to hybridise the plasmonic modes with photonic ones, generating a new modes that posses some of the qualities of both [23]. Firstly, in chapter 3, we, introduce the waveguide plasmon polariton as a specific example of the mode hybridisation scheme. Then we develop the cut-wire as a plasmonic particle with a highly tunable resonance before hybridising this structure with a dielectric waveguide and investigating the narrow transmission bands that can be produced.

In chapter 4, we move onto the dispersion bands of this structure. In particular, we consider how this structure resembles a coupled resonator optical waveguide and how the geometrical

parameters can be used to tailor the dispersion relation. Then, our focus shifts to finite arrays of cut-wires which display Fabry-Perot resonances with highly varying modal losses. We investigate how the decay to individual loss channels can be systematically designed and the effect of disorder on the mode properties. Finally, we consider the potential of finite cut-wire array for slow-light applications.

One of the early examples of the metamaterial paradigm was the demonstration of spoof SPPs, whereby surface waves that mimic the SPP characteristics are produced in perfectly conducting metals by periodically structuring the surface [24]. Interestingly, this enables the transfer of SPP based devices into lower frequency regimes where SPPs are not supported by planar conducting surfaces. Intriguingly, even local surface plasmon resonances (LSPRs) can be spoofed by texturing the surface of metallic particles [25]. In the third section of this thesis we investigate these spoof SPP modes. More specifically, in chapter 5 we briefly review the history of spoof SPPs, explaining the theoretical methods used to explore them. We then investigate how varying the groove geometry affects the spoof SPP characteristics by considering both slanted and triangular grooves, demonstrating that structures with geometries that are extremely different from those traditionally investigated still support spoof SPPs. It should be noted that the work presented in this chapter was begun during my masters project and continued during the beginning of my PhD.

Whilst theoretical methods have been developed for spoof SPPs in perfectly conducting structures, there has been a lack of studies of spoof SPPs in real metals. Although natural SPPs exist for metals in the IR and optical frequency ranges, it would still be useful to be able to tune these SPP modes through surface structuring. In chapter 6, we first review the existing studies, using surface impedance boundary conditions [26] and the effective index technique [27], before developing our own theoretical technique based on the coupled mode method [14]. We show that, particularly in the IR and optical regimes, our method provides a much better match to numerical simulations and enables, for the first time, an analysis of the loss dispersion of spoof SPP modes. We consider how these losses vary with geometry before finally moving on to discuss the potential loss compensation of the spoof SPP modes, and the application of our method to extraordinary optical transmission structures.

2 Background and methods

2.1 Introduction

Since the dawn of civilisation, electromagnetic phenomena, from St Elmo's fire to the electric shocks of catfish and eels [28], have excited people and aroused scientific curiosity. For instance, Thales of Miletus investigated the static electricity effects observed when fur and amber were rubbed together [29]. Throughout the middle ages and the renaissance period a plethora of scientists contributed to the advancement of electromagnetism, producing, amongst many things, the dry compass and the electrostatic generator. Perhaps the most crucial developments in electromagnetic theory came with the discovery of the relationship between electric and magnetic charges and their associated fields. The solidification of these relationships into physical law's by Gauss, Ampere and Faraday paved the way for Jame's Clerk Maxwell's seminal paper of 1865 [30] in which what we now know as *Maxwell's equations* first appeared. Whilst we have come along way since then, Maxwell's equations are still the basis for much of our understanding of the behavior of electromagnetic systems.

In this chapter we provide an overview of the relevant electromagnetic theory. Firstly we review Maxwell's equations, both microscopic and macroscopic, considering the inclusion of linear isotropic media and the continuity equations that must be satisfied at boundaries between different media. We then move on to consider surface waves at a planar interface including surface plasmon polaritons and waveguide modes. Then the localised surface plasmon resonance (LSPR) is considered before we introduce the coupled dipole approximation to investigate arrays of LSPRs. Finally, we take a brief look at the finite element and finite difference time domain methods, as tools for the numerical investigation of electromagnetic phenomena.

2.2 Maxwell's equations

The formulation of Maxwell's equations remains one of the crowning achievements of modern physics. They govern the dynamics of the electric and magnetic fields in media, either due to the presence of sources (such as charges or currents) or due to incident fields from elsewhere. They have been used extensively to study light interactions over a whole range of length scales from the radiation of electrons [31] at one end to the propagation of light through space over cosmological distances at the other. The world we inhabit is quantum and, in some sense, the classical theory of electromagnetism has been superseded with the invention of quantum electrodynamics in the mid 20$^{\text{th}}$ century. However, whilst Maxwell's equations cannot accurately predict quantum phenomena, such as photon squeezing and single photon statistics, in many cases (particularly at larger length scales) the differences from quantum theory are immeasurably small. They are a classical approximation to a quantum world and, for our purposes, an extremely good one.

The microscopic Maxwell's equations determining the dynamics of the electric, $\mathbf{E}(\mathbf{r}, t)$, magnetic, $\mathbf{H}(\mathbf{r}, t)$, electric displacement, $\mathbf{D}(\mathbf{r}, t)$, and the magnetic induction, $\mathbf{B}(\mathbf{r}, t)$, fields are

$$\begin{aligned} \nabla \cdot \mathbf{D}(\mathbf{r}, t) &= \rho, \\ \nabla \times \mathbf{H}(\mathbf{r}, t) - \frac{\partial \mathbf{D}(\mathbf{r}, t)}{\partial t} &= \mathbf{J}(\mathbf{r}, t), \\ \nabla \cdot \mathbf{B}(\mathbf{r}, t) &= 0, \\ \nabla \times \mathbf{E}(\mathbf{r}, t) + \frac{\partial \mathbf{B}(\mathbf{r}, t)}{\partial t} &= 0, \end{aligned} \tag{2.1}$$

where ρ is the electric charge density and $\mathbf{J}$ is the electric current density. These four equations can be considered to give the fields in all space and time provided that all sources are accounted for. However, when considering macroscopic media where every atom is a source, solving the microscopic Maxwell's equations becomes impractical. Furthermore, we are often much more interested in the variation of the fields over larger length scales than that of the inter-atomic distance. So, whilst we are not interested in individual atoms we are now interested in the average response of the medium. The macroscopic fields are of the same form as above except that $\mathbf{E}$ and $\mathbf{B}$ now represent the averaged fields with $\mathbf{H}$ and $\mathbf{D}$ derived from these. For a linear isotropic medium with

no magnetic response we find that

$$\begin{aligned} \mathbf{D} &= \varepsilon_0 \mathbf{E} + \mathbf{P}, \\ \mathbf{H} &= \frac{1}{\mu_0} \mathbf{B}, \end{aligned} \tag{2.2}$$

where ε_0 is the permittivity of free space, μ_0 is the permeability of free space and $\mathbf{P}$ is the polarisation response of the medium. In vacuum there is no polarisation response thus equations (2.2) collapse to $\mathbf{D} = \varepsilon_0 \mathbf{E}$ and $\mathbf{H} = \mathbf{B}/\mu_0$, the well known vacuum constitutive relations. Furthermore, for isotropic linear media, the polarisation response of the material is parallel to the electric field. Thus, $\mathbf{P} = \varepsilon_0 \chi_e \mathbf{E}$, where χ_e is the electric susceptibility of the medium. Using this, we can rewrite Maxwell's equations in terms of only the $\mathbf{E}$ and $\mathbf{H}$ fields yielding (for a source-free medium)

$$\begin{aligned} \nabla \cdot \varepsilon_0 (1 + \chi_e) \mathbf{E}(\mathbf{r}, t) &= 0, \\ \nabla \times \mathbf{H} - \varepsilon_0 (1 + \chi_e) \frac{\partial \mathbf{E}(\mathbf{r}, t)}{\partial t} &= 0, \\ \nabla \cdot \mu_0 \mathbf{H}(\mathbf{r}, t) &= 0, \\ \nabla \times \mathbf{E}(\mathbf{r}, t) + \mu_0 \frac{\partial \mathbf{H}(\mathbf{r}, t)}{\partial t} &= 0. \end{aligned} \tag{2.3}$$

Finally we can replace the term $1 + \chi_e$ with ε_r, the relative permittivity of the region. It is possible to combine the two curl equations, under the assumption that the permittivity is constant in space (i.e. $\varepsilon_r(\mathbf{r})$ = constant), to reveal the wave equations as

$$\nabla^2 \mathbf{E} = \mu_0 \varepsilon_0 \varepsilon_r \frac{\partial^2 \mathbf{E}}{\partial t^2}, \tag{2.4}$$

$$\nabla^2 \mathbf{H} = \mu_0 \varepsilon_0 \varepsilon_r \frac{\partial^2 \mathbf{H}}{\partial t^2}. \tag{2.5}$$

Importantly, we can use one of these wave equations to solve for either the $\mathbf{E}$ or $\mathbf{H}$ field within a region and then utilise equations (2.3) to find the other. For frequency domain numerical electromagnetic solvers the time dependence is assumed to be harmonic, such that $\partial/\partial t \rightarrow -i\omega$, and the wave-equation becomes the well known Helmholtz equation. In contrast, time domain solvers such as FDTD use Maxwell's curl equations.

However, most systems involve several different materials with a step-wise ε_r that depends on the position. In order to solve these we can instead solve the wave equation in each individual medium and then knit the fields together at the boundaries. That is, despite the fact that any

electromagnetic system is unlikely to be homogeneous, its individual components are. So we can solve the wave equation within these regions before matching the fields at the interfaces. This process is known as mode matching and for the majority of the analytical calculations within this thesis it is the route we will take.

2.2.1 Boundary conditions

In order to stitch together the solutions of Maxwell's equations in separate regions of space we need to know how these solutions should match at the interfaces between different media. Using the divergence theorem and Stoke's theorem equations (2.1) can be recast into integral form and from these the continuity of the fields can be derived [31]. They are

$$(\mathbf{D}_2 - \mathbf{D}_1).\mathbf{n} = \rho_s, \tag{2.6a}$$

$$(\mathbf{B}_2 - \mathbf{B}_1).\mathbf{n} = 0, \tag{2.6b}$$

$$(\mathbf{E}_2 - \mathbf{E}_1) \times \mathbf{n} = 0, \tag{2.6c}$$

$$(\mathbf{H}_2 - \mathbf{H}_1) \times \mathbf{n} = \mathbf{J}_s, \tag{2.6d}$$

where ρ_s and $\mathbf{J}_s$ are the surface charge density and the surface current at the interface between the two regions (1 and 2) and $\mathbf{n}$ is the surface normal. Within dielectric media the charge carriers (electrons and ions) are fixed in position, thus surface charges and currents are absent. In this case it is possible to deduce the conditions involving the normal components of the **D** and **B** fields from the conditions imposed on the parallel **E** and **H** fields. Thus, it is sufficient to consider only that the parallel magnetic and electric fields must be continuous across the boundary, with the other conditions being automatically satisfied when this is true.

2.2.2 Maxwell's equations in 2D

When considering electromagnetic phenomena along interfaces and the modes supported by a surface it is often possible to simplify Maxwell's equations. If we are dealing with a structure that is continuous in one direction, and the modes are not propagating into this direction, then Maxwell's equations decouple to form two sets of waves. To see this, let the fields be propagating in either the x, or the z direction and the medium be continuous in the y direction. From this we can see

that $\partial/\partial y \to 0$ and the curl equations decouple; meaning that the two uncoupled sets of fields are the transverse magnetic waves (TM) (E_x, H_y, E_z) where the magnetic fields are only perpendicular to the propagation direction, and the transverse electric waves (TE) (H_x, E_y, H_z) [32] where the electric fields are only perpendicular to the propagation direction. This will aid our analysis of surface and waveguide modes, where the sets of waves can be categorised as TE or TM.

2.3 Metals and dispersive media

As we have already seen, the susceptibility of a medium can be used to link the **D** and **E** fields, allowing Maxwell's equations to be cast in the form of equations (2.2). Thus, when using these equations, the important physics of these materials should be captured within the susceptibility. One of the simplest forms for the susceptibility is the Lorentz-type approach [33] whereby the electrons of the material are treated as a harmonic oscillator, obeying the equation of motion:

$$m\frac{d^2\mathbf{x}(t)}{dt^2} + \gamma m\frac{d\mathbf{x}(t)}{dt} + K\mathbf{x}(t) = -e\mathbf{E}(t), \tag{2.7}$$

where the terms represent the resultant, damping, restoring and driving forces respectively. Fourier transforming and solving for $\mathbf{x}(\omega)$ before substituting for the dipole moment, as $\mathbf{p} = -e\mathbf{x}$, gives **P** as a function of **E**. Finally to link the dipole moment to the polarisation we have

$$\mathbf{P}(\omega) = n\mathbf{p}(\omega) = \frac{ne^2}{m}\frac{\mathbf{E}(\omega)}{K/m - i\gamma\omega - \omega^2} = \varepsilon_0\chi_e\mathbf{E}(\omega). \tag{2.8}$$

As we are interested mainly in plasmonics, and as such deal with noble metals, we can employ the Drude model, whereby the electrons in the metal are assumed to be free, i.e. there is no restoring force since the electrons are not bound to ions, such that $K = 0$. Combining our expression for the susceptibility above, with $\varepsilon_r = 1 + \chi_e$ yields the Drude permittivity

$$\varepsilon_{Drude} = 1 - \frac{\omega_p^2}{\omega^2 + i\omega\gamma}, \tag{2.9}$$

where the plasma frequency is $\omega_p = \sqrt{ne^2/m\varepsilon_0}$. By using the free and independent electron approximations the Drude model neglects both the electron-electron interactions and the electron-ion

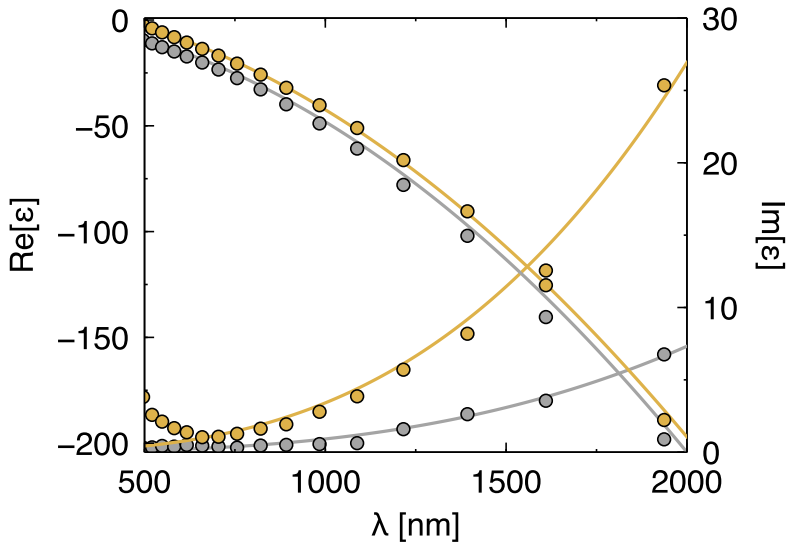

Figure 2.1: Comparison of the Drude model (lines) of the metal permittivity using the parameters in table 2.1 and the experimental results (circles) of Johnson Christy [35]. The silver lines (circles) are for silver and the gold lines (circles) for gold.

interactions, without which many of the properties of metals cannot be even qualitatively understood [34]. Despite this, the Drude model is surprisingly successful in capturing the electromagnetic response of metals. In general, real metals deviate from the Drude response. In order to produce accurate results whilst still employing a Drude model, equation (2.9) is modified to

$$\varepsilon_D = \varepsilon_{\text{inf}} - \frac{\omega_p^2}{\omega^2 + i\omega\gamma}. \tag{2.10}$$

For materials such as gold and silver we can use these parameters (ω_p, ε_{inf}, γ) to fit the experimental data. Table 2.1 shows the parameters used for gold and silver, materials used in this thesis. A comparison of the complex permittivities to experimental data is shown in figure 2.1.

Table 2.1: The parameters for the Drude like permittivity of gold and silver.

	ε_{inf}	ω_p	γ
Silver	4.06	1.36×10^{16}	3.31×10^{13}
Gold	9.00	1.37×10^{16}	1.22×10^{14}

2.4 Surface plasmon polaritons

We now move on to waves confined to the boundary between two different media. Consider an interface at $z = 0$ with dielectric constants $\varepsilon_1(\omega)$ for $z > 0$ and $\varepsilon_2(\omega)$ for $z < 0$. The wavevector is defined as $k = \omega/v_p$ from the phase velocity of the wave, giving the rate of change of the phase of the wave as it propagates in space. Solving the wave equation in each medium for a TM mode gives us fields of the form $\mathbf{E}_i = \mathbf{A}_i \exp[ik_x x - k_{z,i} z]$ where k_x and $k_{z,i}$ are the wavevectors in the z and x axes and the index i is either 1 or 2 for the field in medium 1 and 2 respectively. Using equations (2.6) and (2.3) we can eliminate the expansion coefficients ($\mathbf{A}_i$) and, after some rearranging, we find that

$$k_x = k_0 \sqrt{\frac{\varepsilon_1 \varepsilon_2}{\varepsilon_1 + \varepsilon_2}}, \tag{2.11}$$

where $k_0 = \omega/c$ is the free space wavevector and c is the speed of light in a vacuum. If we take a TE solution to the wave equation we find that no surface wave exists.

Inspecting equation (2.11) we can see that k_x diverges at the point $\varepsilon_1 \to -\varepsilon_2$. In other words, when the dielectric functions have opposite signs and equal magnitude the dispersion relation will cause the wavevector of the surface wave to be infinite. If we now consider a loss-less Drude metal ($\gamma = 0$) we can see that it has a negative permittivity if $\omega < \omega_p$. Taking one medium as air, $\varepsilon_1 = 1$, and the second medium as a loss-less Drude metal we can solve equation 2.11 to find that $\omega^2 = \omega_p^2/2 + c^2k^2 \pm \sqrt{\omega_p^2/4 + k^4c^4}$, where ω is the angular frequency of the surface wave.

This dispersion of the surface plasmon polariton (SPP) is given by the negative square root of this equation and is shown in figure 2.2 (b) by the red line. From this it is easy to observe its dual polariton-plasmon type behaviour; at low wavevectors the wave is polariton-like as it stays close to the light line, for higher wavevectors the solution asymptotically approaches $\omega_p/\sqrt{2}$, and becomes plasmon like. The positive square root gives the plasmon (or volume plasmon) [32], and is shown by the blue line in figure 2.2 (b).

Hence, the interaction of light and matter at the surface between a metal and a dielectric leads to the SPP, a surface wave confined to the interface between the dielectric and metal, that propagates along the interface and decays perpendicular to it. It is a hybrid light matter wave due to the interaction between light and the coherent free electron oscillations in a conducting material [8].

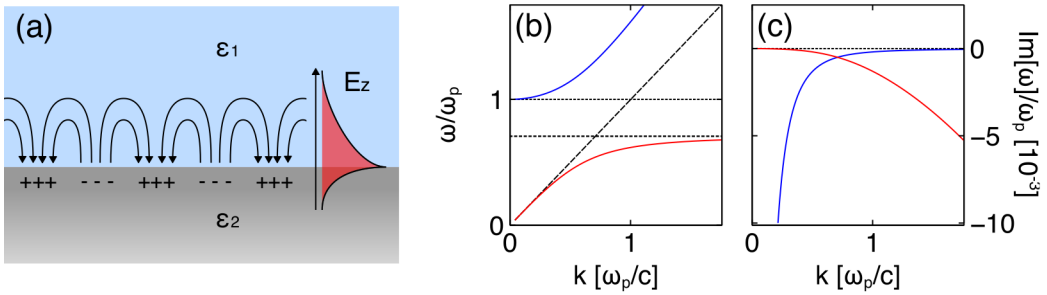

Figure 2.2: (a) A schematic representation of a surface plasmon polariton at a metal dielectric interface, including the decaying field profile perpendicular to the interface. (b) Dispersion of SPP for the Drude gold, inset showing the associated modal losses.

Schematically, the SPP is shown in figure 2.2 (a), where the oscillating charge of the bulk electrons gives rise to the interaction with EM fields at the surface.

Amongst the remarkable features of SPP modes are their high field enhancements (at the interface between metal and dielectric) and their subwavelength nature [8]. The high field enhancements close to the metal surface also mean that SPP modes have associated losses, as shown by figure 2.2 (c). These losses arise from the damped oscillations of the electrons within the metal surface. The SPP decays exponentially away from the interface in both the dielectric and metal media (see figure 2.2 (a)) but the length of this tail depends on the frequency of the mode. When the mode is polariton-like the tail in the dielectric lengthens, thus the field confinement of the mode decreases. Additionally, the propagation length of the mode increases as the proportion of EM energy residing in or close to the metal (causing absorption) is decreased. Conversely, plasmon-like modes are well confined yet experience high losses and low propagation distances as a result. Thus, the propagation of a SPP depends greatly on the frequency of the mode, whether it is more plasmon-like or polariton-like, and there is always a trade-off between loss and confinement.

Finally, one should note that the SPP always appears to the right of the light-line in the dispersion relation meaning there is a momentum mismatch between the SPP and the plane wave propagating in the dielectric medium. Thus SPPs do not radiate and in order to be excited by external EM fields a momentum mismatch must be overcome. Many matching schemes exist in order to do this, such as prism coupling, grating coupling and coupling by other surface inhomogeneities.

2.5 Dielectric slab waveguide modes

Having considered the modes at a single interface the picture can be extended to consider modes where multiple interfaces are involved. A particularly important example of this is the planar dielectric stack (or slab) waveguide. When considering plasmonics and plasmonic systems for on-chip applications then silicon-on-insulator (SOI) platforms are usually involved. Thus, it is important to understand how the photonic modes within these structures behave and propagate. The simplest of these is a three layer slab with permittivities ε_1, ε_2 and ε_3, where central layer thickness is a, see figure 2.3. Assuming a separable solution we find the fields; for TE modes as

$$E_y = e^{iqx} \begin{cases} Ce^{\gamma_1 z} & z < -a/2 \\ (Ae^{ipz} + Be^{-ipz}) & -a/2 < z < a/2 \\ De^{-\gamma_3 z} & z > a/2 \end{cases}, \tag{2.12}$$

and we can derive H_x, H_z from equations (2.1). For TM modes we can substitute H_y for E_y. We should note that one can derive that $p^2 + q^2 = \varepsilon_2 k_0^2$ and $q^2 - \gamma_i^2 = \varepsilon_i k_0^2$, where $i = 1, 3$, from the Helmholtz equation. Matching the parallel field components at the boundaries in the z-direction allows us to derive the relation

$$e^{2ipa} = \left(\frac{p + i\gamma_1}{p - i\gamma_1}\right)\left(\frac{p + i\gamma_3}{p - i\gamma_3}\right), \tag{2.13}$$

for TE modes. Since p, γ_1 and γ_3 are only dependent on the wavevector q, the free space wavevector k_0 and the known material permittivities ε_i this gives us an implicit relation for $q(k_0)$. In the case of a symmetric slab, such that $\varepsilon_1 = \varepsilon_3$ and $\gamma_1 = \gamma_3 = \gamma$, equation 2.13 becomes $\exp[ipa] = \pm(p + i\gamma)/(p - i\gamma)$ which can be rearranged to

$$\tan(pa/2) = \begin{cases} \frac{\gamma}{p} & \text{odd solution} \\ \frac{-p}{\gamma} & \text{even solution} \end{cases}, \tag{2.14}$$

where odd and even denote the solutions to the + and − equations respectively. Furthermore, the odd and even designations refer to the constants A and B with $A = B$ for the odd solution and $A = -B$ for the even. This causes the field in the propagation direction, H_x to be proportional to

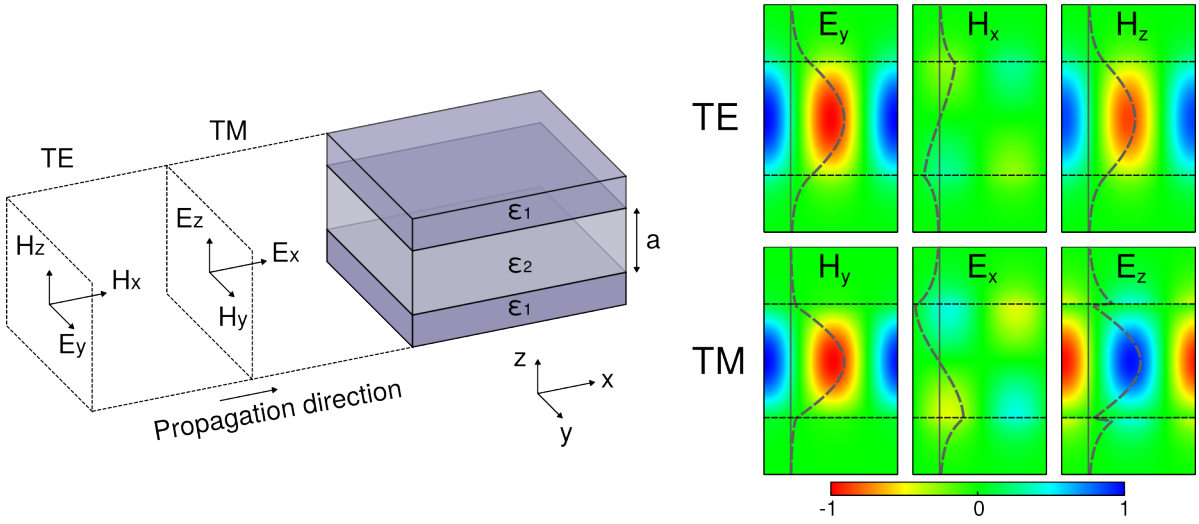

Figure 2.3: The lowest order waveguide modes of a tri-layered dielectric slab. The left shows the general layout of a symmetric waveguide slab and the two polarisations TM and TE. The right shows the field distributions (colour plots) and profiles (dashed grey lines) of the modes TE_0 and TM_0. All the plots are in the same colour scale which ranges from -1 to 1 in arbitrary units, note that the field amplitudes of the magnetic components have been scaled by a factor of 100 so that they are visible. The dashed lines indicate the interfaces between the slabs.

$\sin(pz)$ in the odd case and $\cos(pz)$ in the even.. As the tangent function is a periodic function there are a set of modes $q(k_0)$ that satisfy these equations, the TE waveguide modes of the waveguide slab.

For the case of TM modes we find a very similar set of modes, except that $p \rightarrow p\varepsilon_1$ and $\gamma \rightarrow \gamma\varepsilon_2$. As an example, the field profiles of the lowest odd mode solution for both TE and TM polarisations are shown in detail for a symmetric slab waveguide ($\varepsilon_2 = 4\varepsilon_1$, and $\varepsilon_1 = 1$) in figure 2.3. Note that the TE mode profiles are continuous for all three field components whereas the normal TM component demonstrates discontinuities.

Through the substitution, $q \rightarrow n_{eff}k_0$, it is possible to describe the waveguide slab by means of an effective refractive index. Under this substitution $p = k_0\sqrt{n_2^2 - n_{eff}^2}$ and $\gamma = k_0\sqrt{n_{eff}^2 - n_1^2}$. If we now reconsider our solution again for the symmetric three layered slab, we have at no point enforced that γ is real. In order for a waveguide mode to propagate it is required to be bound to the structure, i.e. it must decay away in the z-direction within the cladding regions. The larger γ is, the faster this decay will be and the greater the field localisation within the central layer. Such modes are called *bound* as the electric fields are tightly bound to the central layer.

However, we can see that if the effective index of the stack were to fall below n_1 then γ would

become imaginary, producing waves that propagate away from the central layer in the z-axis. Thus as $n_{eff} \to n_1$ from above the evanescent tail of the modes into the top and bottom layers increases and the modes become less and less bound until eventually they are no longer bound at all. At this point, the energy in the modes can be quickly radiated out of the waveguide and as such these modes are described as *leaky* [36]. Depending on the particular geometry and materials under consideration $n_{eff}(\omega)$ is a function of the frequency of light, and so for each mode in general there will be a frequency at which it changes from a bound to a leaky mode. This is known as the cut-off frequency. From our definition of γ it is possible to derive the cut-off for each mode. At each cut-off the associated γ of each mode will become 0. Thus, from equation (2.14) $\tan(pa/2) = 0$ for the odd modes and $\tan(pa/2) = \infty$ for the even. As such we find that the cutoffs are:

$$\omega_{co} = c \begin{cases} \frac{2m\pi}{a\sqrt{n_2^2 - n_1^2}} & \text{odd} \\ \frac{(2m+1)\pi}{a\sqrt{n_2^2 - n_1^2}} & \text{even} \end{cases}, \tag{2.15}$$

where $m = 0, 1, 2, ...$ meaning that there is only one mode which has no lower frequency cut-off, the m=0 odd mode. For every other mode there is a ω_{co} above which it is bound and below which it is leaky.

2.6 Plasmonic arrays

Over the past decade there has been great interest in plasmonic arrays and surfaces of plasmonic nanoparticles. The discovery of extraordinary optical transmission (EOT) by Ebbesen et al in 1998 [13], whereby the classical diffraction limit of the hole size is overcome and transmission can approach unity, marked the start of this era. For several years the theoretical nature of this problem was not understood until it was shown that SPPs are involved in the resonant process channeling light through the structure [37]. Since this time there have been many investigations into plasmonic arrays including, amongst others, lasing in strongly coupled arrays [38] and loss-compensated negative index materials [18, 39].

Many of these consider the interaction of several localised surface plasmon modes. The coherent electron oscillations that give rise to the bulk plasmon within a metal, and thus the SPP at the metal-dielectric interface, still exist in a metallic nanoparticle. In this situation the light-matter

interaction results in the localised surface plasmon resonance (LSPR) of the nanoparticle. In the following we will derive the LSPR of a spherical metallic nanoparticle.

2.6.1 Local surface plasmons and dipole polarizability

The susceptibility is defined through the relationship $\mathbf{P}(\mathbf{r}) = \varepsilon_0 \chi_e \mathbf{E}(\mathbf{r})$ where $\mathbf{E}(\mathbf{r})$ is the macroscopic electric field. In sparse media, where the molecules are relatively spread out, the contributions to the field at a molecule, m, from the other molecules within the medium is small and the local field is dominated by the macroscopic field. However, where media are more dense the polarization of molecules within the vicinity causes an internal field $\mathbf{E}_i(\mathbf{r})$; i.e. the total field, $\mathbf{E}_l(\mathbf{r})$, felt by molecule m is the sum of $\mathbf{E}(\mathbf{r})$ and $\mathbf{E}_i(\mathbf{r})$. To get the correct value for $\mathbf{E}_i$ we can subtract away the smoothed macroscopic contribution from the local field m and add in the contribution of molecules close to m, $\mathbf{E}_{near}(\mathbf{r})$, to give

$$\mathbf{E}_l(\mathbf{r}) = \mathbf{E}(\mathbf{r}) + \mathbf{E}_i(\mathbf{r}) = \mathbf{E}(\mathbf{r}) + \mathbf{E}_{near}(\mathbf{r}) - \mathbf{E}_{far}(\mathbf{r}). \tag{2.16}$$

In other words we have artificially created a region of radius r around the molecule m. Within that region we remove the macroscopic field and instead replace it with the contribution of all molecules close to m. The macroscopic electric field withing a uniformly polarised sphere is -$\mathbf{P}/3\varepsilon_0$. In the special case of a lattice with cubic symmetry the microscopic local field inside the region near to the ion $\mathbf{E}_n^{mic}(\mathbf{r})$ vanishes on all lattice points, removing the term from the equation above and using the fact that $\mathbf{P} = \varepsilon_0 \chi_e \mathbf{E}$ the local field at $\mathbf{r}$ can be written in terms of the total macroscopic field

$$\mathbf{E}_l(\mathbf{r}) = \mathbf{E}(\mathbf{r}) \frac{\varepsilon_r + 2}{3}. \tag{2.17}$$

Finally, we can link the polarisation of the region near the ion to the local field through the dipole polarizability. The dipole polarizability α links the response of an electric dipole to the electric field via $\mathbf{p}(\mathbf{r}) = \alpha \mathbf{E}(\mathbf{r})$; and the total polarisation is the sum over all the dipole moments within the region $4\pi/v \sum \mathbf{p}_i$ so we find that $\mathbf{P}(\mathbf{r}) = 4\pi\alpha \mathbf{E}_l(\mathbf{r})/v$. This gives the polarizability as

$$\alpha = 4\pi a^3 \frac{\varepsilon_r - 1}{\varepsilon_r + 2}, \tag{2.18}$$

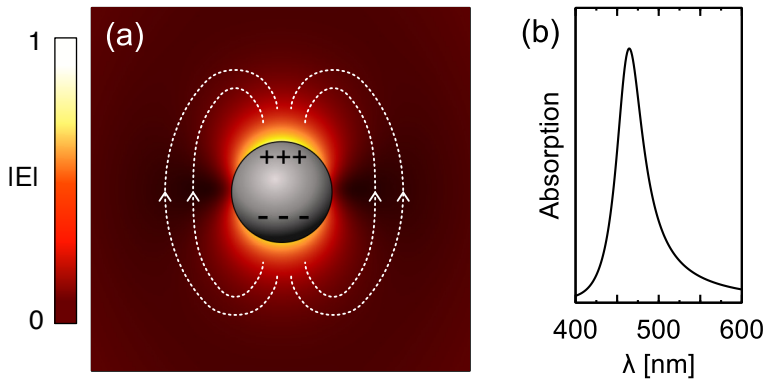

Figure 2.4: (a) Schematic of the $|E|$ of an excited dipole (or LSPR); also plotted is a snapshot of the charge distribution and the associated field lines. (b) Example of the dipole absorption spectrum, as calculated using the dipole polarizability equation (2.18) for a silver nanoparticle.

which is the well known Clausius-Mossotti relation (also sometimes known as the Lorentz-Lorenz relation)[1] relating the atomic polarizability of a material to the useful material parameter ε_r thus allowing a link between the microscopic and macroscopic regimes [34]. Traditionally this relation would be used to predict the optical properties of insulators from an α that had already been calculated from microscopic theory. However, we can turn this situation around and use it to calculate the dipolar response of a medium given a particular relative permittivity. Considering a sphere of material with dielectric permittivity ε_r, and assuming that the electric field is constant across the sphere the optical response of the nanoparticle can be understood from equation 2.18. It should be noted that this quasi-static approximation is restrictive, only allowing the dipole modes and not higher order modes of the system.

An example of the dipolar response of a gold metal nanoparticle is shown in figures 2.4 (a) and (b). If we take the loss-less Drude model and insert it into equation 2.18 we find that

$$\alpha = 4\pi a^3 \left(\frac{3\omega^2}{\omega_p^2} - 1 \right)^{-1}, \tag{2.19}$$

which diverges at the point $\omega = \omega_p/\sqrt{3}$. This is the localised surface plasmon resonance (LSPR) of the nanoparticle.

[1] For further details on this derivation, see Ashcroft and Mermin [34] chapter 27 *Theory of the local field* or Jackson [31] chapter 4.5.

2.6.2 Coupled dipole approximation

When considering a system of multiple separate plasmonic resonances that have the capacity to interact the situation becomes more complex. For instance, within a system of two nanoparticles each one will be affected by the other nanoparticle's response to the electric field. Thus the polarisation of one dipole causes a response from the other particle. The electric field can be modeled using the Green's dyadic

$$\mathbf{G} = \frac{1}{4\pi\varepsilon}\left[\left(\frac{1}{|\mathbf{r}|^3} - i\frac{k}{|\mathbf{r}|}\right)\left(3\frac{\mathbf{r}\otimes\mathbf{r}}{|\mathbf{r}|^2} - \mathbb{1}\right) + \frac{k^2}{|\mathbf{r}|}\left(\mathbb{1} - \frac{\mathbf{r}\otimes\mathbf{r}}{|\mathbf{r}|^2}\right)\right] e^{i\mathbf{k}|\mathbf{r}|}, \tag{2.20}$$

where ε is the permittivity of the background medium, $k = \omega\sqrt{\varepsilon_r\varepsilon_0\mu_0}$ is the wavevector within the background medium and $\mathbb{1}$ is the identity matrix. Thus, the dipole moment induced on the jth nanoparticle within an system of n nanoparticles is

$$\mathbf{p}_j(\mathbf{r}_j) = \alpha\left[\mathbf{E}_{incident}(\mathbf{r}_j) + \sum_{i\neq j}^{n}\mathbf{G}(\mathbf{r}_j - \mathbf{r}_i)\cdot\mathbf{p}_i(\mathbf{r}_i)\right]. \tag{2.21}$$

In other words, this is a system of n coupled equations, where each dipole is dependent on the fields produced by all the others. In order to solve such an equation we can put it into matrix form and collect all the dipole terms on the left hand side yielding:

$$\mathbf{SP} = \mathbf{E}, \tag{2.22}$$

where $\mathbf{P} = \{\mathbf{p}_1(\mathbf{r}_1), \mathbf{p}_2(\mathbf{r}_2), \ldots, \mathbf{p}_n(\mathbf{r}_n)\}^T$ is a vector of all the 3 dimensional dipole moments, $\mathbf{E} = \{\mathbf{E}_1(\mathbf{r}_1), \mathbf{E}_2(\mathbf{r}_2), \ldots, \mathbf{E}_n(\mathbf{r}_n)\}^T$ is a vector of the incident electric fields on each dipole. The matrix $\mathbf{S}$ is composed of 3×3 block matrices where:

$$\begin{aligned} S_{ii} &= \alpha^{-1}\mathbb{1}, \\ S_{ij} &= -\mathbf{G}^{-1}(\mathbf{r}_i - \mathbf{r}_j). \end{aligned} \tag{2.23}$$

Importantly, this method effectively decouples the electric dipoles, meaning we can imagine each of the dipoles as acting independently of the others, with the fact that it now experiences a modified incident field $\mathbf{p}_1 = \mathbf{E}_1' = \mathbf{S}^{-1}\mathbf{E}$. It should be noted that the above equation is for a spherical dipole

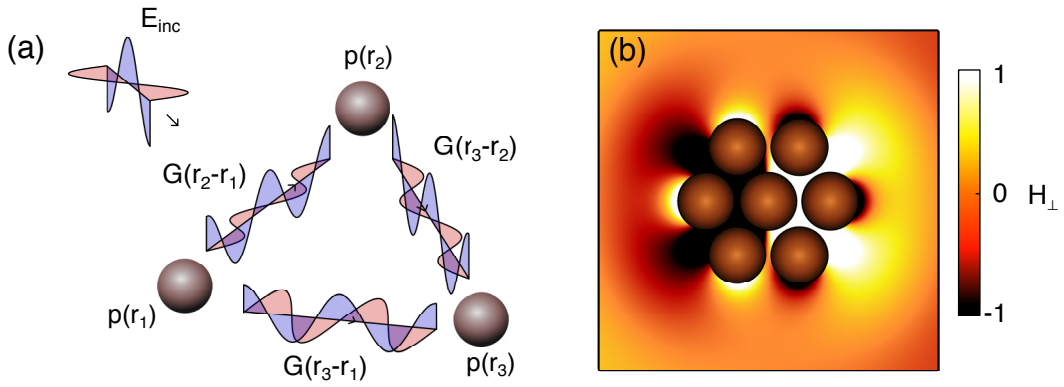

Figure 2.5: (a) Schematic of the coupled dipole approximation and the propagation of the various dipole fields. (b) Example of a magnetic field profile (perpendicular to the oligomer plane) that can be produced for the sub-resonant mode of a plasmonic heptamer [40] as calculated using CDA.

polarizability. For non-spherical particles, where the polarizability is no longer isotropic and α becomes a tensor, the equations still hold except that $\alpha^{-1}\mathbb{1}$ is replaced with the inverse of the polarizability tensor. The two standard ways of solving this equation are:

1. Assuming a zero incident field yielding **SE** = 0 which implies that det[**S**] = 0, which can be then be solved through minimisation techniques.

2. Inject an incident field into the system and solve for the dipole moments of each particle and solving for each dipole moment in the system. Then, the spectral response of the system can be calculated, for instance, the absorption cross-section $C_{abs} = k_0 \mathrm{Im}[\alpha]$ [33]

Thus, CDA can be used to calculate the effective modes of a system of n dipoles and can give us a great deal of insight into the properties of plasmonic surfaces.

The simplest structures that can be considered using the CDA are dipole chains or 1D chains of nanoparticles. For a dipole chain the vector between dipoles is $\mathbf{r} = d\hat{\mathbf{u}}$ where the unit vector $\hat{\mathbf{u}}$ is parallel to the chain axis. Analysing equation (2.20) shows that for dipoles orientated along the axis there is no far-field interaction. Thus, there are two types of mode; longitudinal (L), aligned along the axis and transverse (T), aligned perpendicular to the axis.

There have been several studies on these modes on the dipole chain [41, 42, 43, 44, 45, 46, 47, 48, 49, 50, 51, 52] and in particular they find that the dispersion relation reveals several features. Firstly, the two modes, T and L, resolve into two separate dispersion bands. L (T) changes from the lower (higher) energy symmetric mode to the higher (lower) energy anti-symmetric mode as

the Brillouin zone is traversed. This is precisely the analogue of the coupling of two individual resonances, see for example [53]. Secondly, the T mode has a distinctive character in that it includes the far-field coupling of the particles which leads to a dipping of the mode around the light-line (for instance, see figure 2 in [47]). It is this far-field coupling of the particles which has led to the phenomena of extremely narrow absorption peaks in dipole chains [43]. This occurs when the lattice spacing is equal to a multiple of the free-space wavelength, provided that this falls within the broad resonance of the plasmonic wires. Note that at these typically large lattice spacing the particles can be approximated as independent (i.e. that the near-field coupling is negligible) and essentially the absorption cross-section is a superposition of the individual particle resonances and that of the lattice resonance.

The coupled dipole approximation has been used to study many plasmonic structures, from chains to arrays [54] of more complex layouts such as oligomer type structures [55] and also to investigate the potential of 3D metamaterials with magnetic and electric resonances [56]. In chapter 3 we will consider the CDA to understand the cut-wire resonator and how it can be spectrally controlled.

2.7 Numerical methods

As well as using theoretical methods we have used numerical methods to investigate the properties and electromagnetic phenomena of plasmonic surface structures. Numerical methods can be efficient methods for the design and optimisation of systems or the scientific investigations of new structures. Typically, they solve Maxwell's equations on a grid (or mesh) and within this thesis we make use of both finite element methods (FEM) and the finite difference time domain method (FDTD).

2.7.1 Finite element method

FEM can be used to find approximate solutions to the boundary value problems of specific partial differential equations [57]. The system under consideration is sub-divided into a finite number of elements, and the partial differential equations are applied at each of these elements. One major advantage of FEM is the subdivision of the system into the finite elements (also known as the *mesh*)

which allows for different parts of the system to have a higher number of elements where higher accuracy is needed. Similarly, this meshing allows more complicated shapes to be simulated as the mesh can adapt to complicated surfaces. Within this thesis FEM methods are primarily used to find solutions to two types of problems, eigenvalue problems and scattering problems. The software package used is COMSOL Multiphysics (www.uk.comsol.com), a commercially available solver. Finally, we have used the frequency domain solver, whereby a solution of the form $\exp[-i\omega t]$ is assumed such that $\partial/\partial t \rightarrow -i\omega$ in equation (2.4).

The eigenvalue problem considers the system isolated from electromagnetic sources. By assuming an initial guess frequency of the mode the partial differential equation becomes an eigenvalue equation. Such a problem can be solved iteratively until the discrete eigenvalues of the system have converged to within the specified error parameters. For isolated finite systems such a simulation returns the eigenmodes of the structure. Importantly, we can consider a unit cell of a structure and enforce periodic boundary conditions that require the fields at each boundary to be identical except for a pre-determined phase. This phase, ϕ, is linked directly to the wavevector $k = \phi/d$. Thus by changing the phase from $0 - \pi$ and, for each phase, performing an eigenmode analysis of the system, the frequency of the mode as a function of wavevector, i.e. the band structure, can be calculated.

The scattering problem inserts a time harmonic source into the system, which can be anything from a plane-wave to a dipole source to a waveguide mode, and then calculates the response of the system. From such simulations transmission, reflection and absorption parameters can be calculated via the Poynting vector. The Poynting vector $\mathbf{S} = \mathbf{E} \times \mathbf{H}$ represents the rate of energy transfer of the electromagnetic field per unit area. To calculate the time-averaged transfer of energy, S, through an area, A, we can integrate the Poynting's flux

$$S = \int_A \mathrm{Re}[\mathbf{E} \times \mathbf{H}^*] \cdot \mathbf{dA}. \tag{2.24}$$

Calculating the transmission and reflection coefficients is simply a matter of calculating the flux S due to the scattered fields and dividing it by the flux due to the incident fields.

In chapter 4 the eigenmode solution is used to calculate the individual decay channels of the mode. This can be done using Poynting's theorem which states that the rate of change of the

energy (u) contained within the electromagnetic system is equal to the rate of energy transfer out of the system, through radiation and absorption. Mathematically we have that

$$-\frac{\partial u}{\partial t} = \nabla \cdot \mathbf{S} + \mathbf{J}.\mathbf{E}. \tag{2.25}$$

To calculate the time-averaged individual decay rates from the numerical simulation we need to integrate over the electric and magnetic fields, in the frequency domain, accounting for the fact that the metal is a dispersive medium, for full details see appendix A. For these finite sized simulations the boundary conditions are important and care has to be taken to ensure they don't impact on the solution returned by the simulations. In order to avoid back reflections of the fields scattered by the mode we use scattering boundary conditions which allow out-going electric fields to pass through.

When deciding which method to use where in the thesis it is important to understand how each method will solve Maxwells equations

- The Eigenmode method will solve Maxwells equations with a complex frequency component. Thus for either periodic systems (where the phase-vector is ofrced to be real), or isolated systems the imaginary frequency corresponds to the modal decay.

- The scattering method will force an incident wave upon the system, thereby (in general) ensuring a real frequency of the incoming wave and thus producing a complex wave-vector, where the imaginary wave-vector corresponds to the decay of the excited modes in space.

In this Thesis, the eigenmode method is predominantly used in chapters 4, 5 and 6; in particular in the numerical results of figures 4.3, 4.4, 4.5, 4.6, 4.7, 4.8, 5.5, 5.8, and 6.4. Whereas the scattering method is used in chapters 3 and 4; in particular the numerical results of figures 3.3, 3.4, 3.5 and 4.2.

2.7.2 Finite difference time domain method

Whilst the finite element method, and the theoretical approaches we have covered above, work in the frequency domain the finite difference time domain method solves the time-dependent Maxwell's equations. FDTD has several advantages over frequency domain methods such as FEM. FEM requires solving the linear algebra of the Fourier transformed Maxwell's equations, and

as such the computational memory scales quadratically with system size. Within FDTD, the computational memory only scales linearly with system size as it relies on the using the evaluated fields at time t to calculate the fields at $t+\delta t$. Therefore, the computational cost of increasing the number of grid points (or refining the mesh) is much less for FDTD method than FEM. FDTD also allows the direct visualisation of the evolving electric and magnetic fields, offering an intuitive and insightful picture into the underlying physics. Perhaps most importantly, FDTD allows the direct treatment of non-linear effects as other differential equations (such as those for non-linear media) can be directly included. This makes FDTD an extremely valuable tool for considering loss-compensated and lasing plasmonic systems.

In FDTD Maxwell's equations are discretised on a 3D grid. The derivatives are discretised using the central difference theorem, whereby the differentials become

$$\frac{df_n}{dx} = \frac{f_{n+1} - f_{n-1}}{2\delta x} + O(\delta x^2) \approx \frac{f_{n+1} - f_{n-1}}{2\delta x}, \tag{2.26}$$

which is accurate to second order in the discretisation parameter δx. However, from Maxwell's equations we know that the temporal derivatives of the **E** (**H**) fields are dependent on the spatial derivatives of the **H** (**E**) field. Thus, we do not need to evaluate all fields at each grid point. Instead a staggered grid is used, the so called Yee-cell, as defined by K. S. Yee [58], see figure 2.6. In this, the electric and magnetic fields are evaluated at subsequent time steps, in order to make full use of Maxwell's curl equations. Overall this means that the propagation of fields can be calculated as

$$\begin{aligned} E_x|_{n+1}^{i+1/2,j,k} = E_x|_n^{i+1/2,j,k} &+ \frac{\delta t}{\delta y\, \varepsilon_0 \varepsilon|^{i+1/2,j,k}} \left(H_z|_{n+1/2}^{i+1/2,j+1/2,k} - H_z|_{n+1/2}^{i+1/2,j-1/2,k} \right) \\ &- \frac{\delta t}{\delta z\, \varepsilon_0 \varepsilon|^{i+1/2,j,k}} \left(H_y|_{n+1/2}^{i+1/2,j,k+1/2} - H_y|_{n+1/2}^{i+1/2,j,k-1/2} \right) \\ &+ \frac{1}{\varepsilon_0 \varepsilon|^{i+1/2,j,k}} \left(P_x|_{n+1}^{i+1/2,j,k} - P_x|_n^{i+1/2,j,k} \right), \end{aligned} \tag{2.27}$$

$$\begin{aligned} H_x|_{n+1/2}^{i,j+1/2,k+1/2} = H_x|_{n-1/2}^{i,j+1/2,k+1/2} &- \frac{\delta t}{\delta y\, \mu_0} \left(E_z|_n^{i,j+1,k+1/2} - E_z|_n^{i,j,k+1/2} \right) \\ &+ \frac{\delta t}{\delta z\, \mu_0} \left(E_y|_n^{i,j+1/2,k+1} - E_y|_n^{i,j+1/2,k} \right), \end{aligned} \tag{2.28}$$

where $\varepsilon|^{i,j,k}$ is the permittivity of the medium at the grid point (i, j, k).

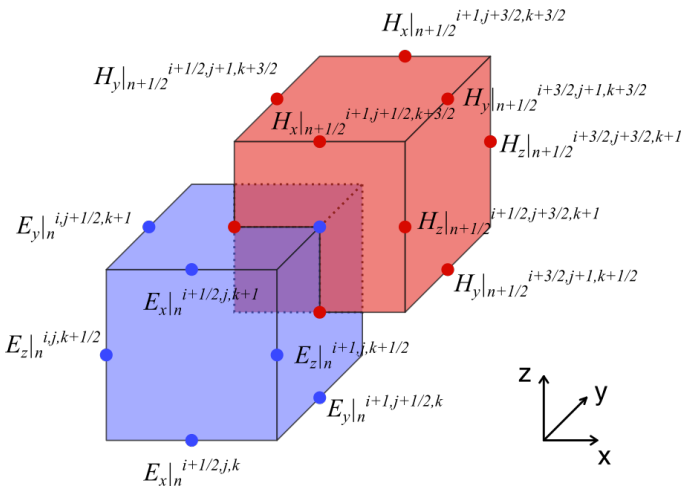

Figure 2.6: Schematic of the Yee cell demonstrating the discretised electric and magnetic field components.

To take account of the dispersive metallic response in time domain, the equation $\mathbf{P}(\omega) = \varepsilon_0 \chi_e(\omega)\mathbf{E}(\omega)$ needs to be Fourier transformed into the time domain. For a Lorentz-type material response (of which the Drude model is an example) $\chi_e \propto (a - ib\omega - c\omega^2)^{-1}$. Fourier transforming the polarisation recovers a second order differential equation

$$c\frac{d^2\mathbf{P}}{dt^2} + b\frac{d\mathbf{P}}{dt} + a\mathbf{P} \propto \mathbf{E}. \tag{2.29}$$

From Ampere's law the electric field is driven by the curl of the magnetic field and the time derivative of the polarisation. To solve this the polarisation is also discritised and solved within the FDTD formalism, much like equations (2.27) and (2.28). The FDTD method will be used in chapter 6 to compare theoretical results with numerical ones, in the case of spoof SPPs.

2.8 Note on the theoretical methods used in this thesis

Throughout this thesis we have studied two structures, cut-wire arrays (chapters 3 and 4) and 1D metallic grooves (chapters 5 and 6). In both of these cases we have considered only the wave-vector along the arrays (which we will define as the y-axis), ignoring in our analysis the out of plane wave-vectors (which we will define as the x-axis).

In the case of the 1D metallic grooves, the structure is completely continuous in the x direction and thus supports no periodic band structure in this direction. Instead, a non-zero k_x would

be expected to have a similar effect as is the case for photonic crystal structures, for instance see reference [59]. We have ignored it in our analysis as we have been focused on how the array geometry - particular the periodicity and the groove geometry - affect the band structure and in particular the plasmon-like modes that appear. It would be possible to extend our theory by considering a transverse wave-vector, for instance by assuming a plane-wave solution for the transverse fields.

For the cut-wire arrays, the structure is periodic in the x direction and so does support a Bloch-wave solution along this direction. In chapters 3 and 4 we only consider the cut-wire to be excited along the wire axis - i.e. in the longitudinal mode. It is well known that the band-structure of a single dipole-chain longitudinal mode varies smoothly from the symmetric to the antisymmetric mode across the FBZ, e.g. see references [47, 51]. In this thesis we have been only concerned with the interaction of 1D waveguide modes with the cut wire array - modes which have $k_x = 0$, and thus assuming the cut-wires to be excited in the symmetric longitudinal mode - where all the dipoles are in phase. Whilst this is not the total solution of these structures, where k_x would be expected to vary, due to the symmetry of the system modes with different k_x would not couple, and thus it is valid to consider only a single k_x value at a time. Thus, this work can be considered a starting point towards a general solution with a non-zero k_x.

3 Waveguide plasmon polaritons and cut-wires resonators

3.1 Introduction

The concept of hybridising plasmonic resonances was first described by Prodan and co-workers [60] who showed that the complex response of a plasmonic nanostructures can be viewed as the interaction of the LSPRs of the constituent components, leading to hybridised plasmonic modes. Importantly, hybridisation of plasmonic modes can lead to interesting and novel optical properties such as negative magnetic responses [61], plasmonic electromagnetically induced transparency [62] and extraordinary optical transmission [13, 63]. Using this hybridisation many plasmonic systems have also been shown to exhibit asymmetric Fano-type resonances [64] with the potential for applications in sensing and opto-electronic devices.

One of the drawbacks of plasmonic systems is the cripplingly high resonator losses with accompany LSPRs and effectively limits their potential. Mode hybridisation is one method by which these parasitic material losses can be circumvented. Plasmonic and photonic modes have contrasting size/loss characteristics. Whilst plasmonic modes offer subwavelength confinement of light and high material losses, photonic modes are typically much larger ($\approx \lambda$) whilst incurring far lower material losses. One method of hybridisation is utilising photonic modes to mediate the coupling between plasmonic resonators, for example, through a dielectric waveguide [23].

In this chapter we consider one example of a photonic-plasmonic mode hybridisation scheme, the so-called waveguide plasmon polariton (WPP). So far, the bulk of the work on WPPs has been using TM waveguide modes and there has been little interesting in utilising TE waveguide modes. After describing the origins of the WPP we consider the differences between TM and TE waveguide

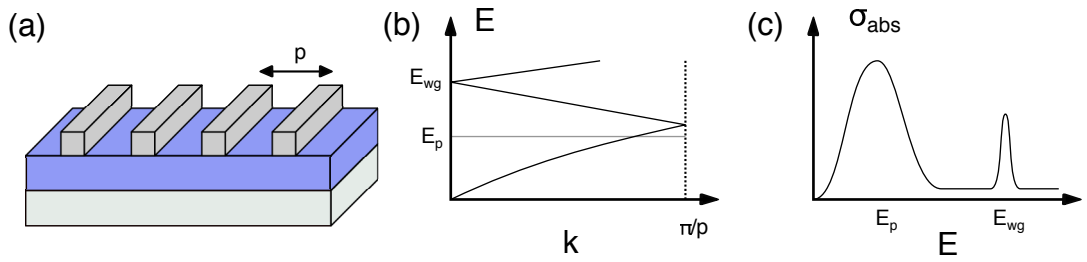

Figure 3.1: (a) Schematic of the typical WPP structure consisting of an array of plasmonic wires on top of a waveguide slab, where p is the periodicity of the array. (b) Dispersion realtion of the waveguide slab, including also the energy of the plasmonic-wire mode (grey line). (c) Example of a typical absorption spectra of the WPP structure when illuminated with normal incidence TM waves.

modes and the potential benefits that TE modes can offer. Then we discuss the plasmonic cut-wire resonator and its spectral response before combining the two to analyse TE WPPs. Finally, we demonstrate how this system can form arbitrary narrow transmission peaks and discuss whether these can be used for high contrast sensing applications.

3.2 Waveguide plasmon polaritons

What is a WPP? The WPP is a hybrid mode produced by the interaction of plasmonic and waveguide modes in a 1D plasmonic array. It was first considered by Christ et al. in 2003 [15] and the general structure used to induce WPPs is shown in figure 3.1(a). It consists of a slab waveguide and a 1D periodic grating. It is generally excited by an incident wave from the top. The periodic grating produces a back-bending of the waveguide mode as shown in figure 3.1(b), where the energy of the plasmonic wire mode is also shown. When illuminated from normal incidence with a TM wave the structure shows two distinct peaks, as shown in figure 3.1(c), corresponding to the new hybrid WPPs which appear close to the uncoupled plasmonic and waveguide resonances. By altering the period, *p*, of the array the wavelength of the waveguide mode is altered. As the two resonances approach one another the absorption spectra displays anti-crossing behaviour where the spectral line shape is transferred between resonances, demonstrating the creation of a hybrid mode which mixes the plasmonic and photonic elements.

In 2009, Zentgraf et al [65] demonstrated that the mechanism which creates the WPP could also enable the formation of a low-loss mode. Importantly, they showed that the degeneracy of the

waveguide modes at the edges of the Brillouin zone causes the creation of a hybrid mode that is purely photonic, but this is only possible through the interaction of the resonant plasmonic structure. In effect, at a particular frequency, the electric fields destructively interfere at the locations of the plasmonic particles. Thus, the plasmonic nanowires are not excited don't cause system losses. This is the plasmonic analogue of the electromagnetically induced transparency (EIT) phenomena [66] first observed in atomic systems. This occurs at the array resonance, where the incident light is resonantly coupled into the waveguide modes of the structure, at $\lambda = 2n_{eff}p$, producing constructive interference due to the Bragg condition. However, the WPP structure differs from the Bragg resonance in that the component that gives rise to the periodic structure (i.e. the plasmonic nanowire) is optically active causing the creation of the third, high transmission, mode. Whereas, in a standard Bragg mirror structure the structural component has no optical excitation.

The high transmission modes appear in the frequency gap between the anti-crossing WPP modes and can be made extremely narrow by tuning the plasmonic resonance close to the waveguide mode cut-off. Such sharp spectral features can be extremely useful for sensing as small shifts due to surface refractive index changes can cause a relatively large change in the optical properties. Although the waveguide mode cut-off can be arbitrarily designed through the waveguide geometry, it would require being able to produce accurate waveguides of variable thickness and composition. Typically, dielectric waveguides are composed of commercial wafers, and come in well defined sizes, hence it can be difficult to arbitrarily tune the cut-off frequency of the waveguide modes. In contrast, the plasmonic nanowires are usually placed on the surface through techniques which allow for the tailoring of the geometric parameters, for example using electron-beam lithography. As the LSPR of the nanowire depends on both the structure and material it is much easier to tune than the waveguide mode cut-off.

Until now the WPP has been mainly explored using TM waveguide modes. One potential reason for this is the ease at which metallic nanowires can be created. TE waveguide modes have their electric field components parallel to the axis of the nanowire, and thus would need to excite the LSPR along the nanowire. However, nanowires do not exhibit a LSPR along their axis due to their continuous nature. Hence, in order to utilise TE waveguide modes within the WPP we would need to consider a different plasmonic resonator. In the next section we consider first the differences between TE and TM waveguide modes, before considering the cut-wire, a plasmonic

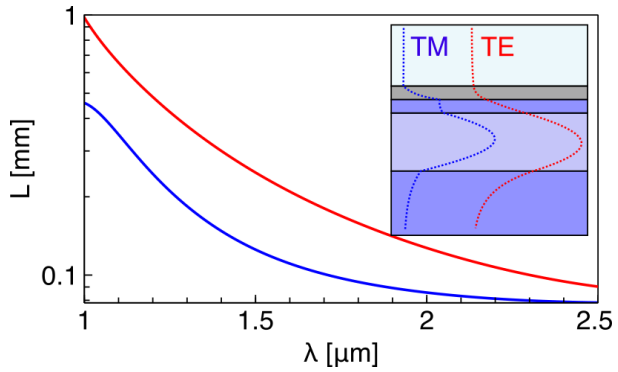

Figure 3.2: The effect of an additional metallic layer on waveguide modes. The propagation distance L is plotted as a function of the wavelength λ. Both TE (red) and TM (blue) waveguide modes are considered. The inset shows the schematic of the metal-covered waveguide as well as the modal profiles at λ = 1550nm for both TE and TM modes.

resonator that allows LSPRs parallel to the wire axis.

3.3 TE waveguide modes

An important effect of incorporating a metallic nanowire on top of the dielectric slab waveguide is the introduction of loss into the system. The new waveguide modes of the metal covered dielectric waveguide have a complex wavevector and thus, an associated propagation length. The propagation length, L, is defined as $L = 1/(2\text{Im}[\beta])$ where β is the wavevector of the waveguide mode, in the direction of propagation.

To consider the effect of the metal layer on both TE and TM waveguide modes, we solve for the new waveguide modes, as in section 2.5. The test structure can be seen in the inset of figure 3.2. It incorporates 5 layers; the semi-infinite substrate n_1, the central waveguiding layer of n_2 of width 220nm, a buffer layer n_1 of width 50nm, a metal layer ε_m of width 50nm and a semi-infinite superstrate composed of air $\varepsilon = 1$. The refractive indices of the cladding, n_1, and core, n_2, are assumed to be 1.5 and 3.5 respectively.

From figure 3.2 we can see how the propagation length alters as the wavelength is changed from 1μm to 2.5μm. As the wavelength increases the propagation lengths of both the TM (blue line) and TE (red line) modes are reduced and throughout this spectral range (and generally) the TE waveguide mode has a higher propagation distance than the TM waveguide mode[1].

[1]The propagation length is also strongly dependent on the height of the buffer layer, which controls the strength of the effect of the metal on the waveguide modes.

The profile of the waveguide modes is also affected by the presence of the metal layer on top of the dielectric stack. The inset of figure 3.2 shows the waveguide mode profiles at λ = 1550nm. Comparing to the case of a bare dielectric waveguide (see figure 2.3) the change in the TE mode profile is relatively small. The mode maximum is no longer exactly in the centre of the central waveguiding layer, instead it has been pushed down slightly away from the metal surface. In contrast, the change in the TM mode profile is dramatic. A large amount of energy is concentrated within the buffer layer, between the central waveguide layer and the metal, contributing to the increased modal loss.

Finally, we consider the effective indices of the TE and TM modes respectively. By considering equation (2.14), and replacing the mode wavevectors with the effective index of the TE and TM modes we have that

$$\tan(k_0 a/2\sqrt{n_2^2 - n_{eff}^{TM\,2}}) = \frac{n_2^2}{n_1^2}\tan(k_0 a/2\sqrt{n_2^2 - n_{eff}^{TE\,2}}). \tag{3.1}$$

As the core layer has a higher refractive index than the cladding layers we can conclude that $n_{eff}^{\mathrm{TM}} < n_{eff}^{\mathrm{TE}}$. Thus, the effective wavelength of the TE mode is shorter than that of the TM mode, allowing structures that rely on TE modes to be contracted compared to their TM counterparts.

Considering these factors, we can see that TE modes can have many appealing advantages over their TM counterparts, such as increased propagation lengths and less disruption of the modal profile. Furthermore, the TE mode only interacts with the metal through the evanescent tail of the mode, and can almost be considered unaffected by the presence of the metal [67].

3.4 Cut-wire resonators

Within this thesis, a cut-wire is defined as a wire with rectangular cross-section that is cut into segments of length l with gaps of length g in between. This structure repeats periodically with a total periodicity $g+l$, see figure 3.3 (a). The cut-wire is similar to the dipole chains considered in the previous chapter, whereby each segment of wire can be considered as an electric dipole and thus the whole wire is simply a chain of dipoles. However, the segments within the wire are cuboidal in shape, in contrast to the nanospheres we had previously considered, and as such the Clausius-Mosotti relation for the polarizability is no longer valid. Most importantly, the three dimensions of

the oblong are no longer equal, and as such the polarizability is no longer isotropic.

To obtain a simple model for the polarizability of the cut-wire segments we approximate them as prolate spheroids where the long axis a_1 is greater than the two other axes a_2, a_3, see figure 3.3 (b). Thus the polarizability tensor becomes

$$\alpha = \begin{pmatrix} \alpha_1 & 0 & 0 \\ 0 & \alpha_2 & 0 \\ 0 & 0 & \alpha_3 \end{pmatrix}, \qquad \alpha_i = \frac{4\pi a_1 a_2 a_3(\epsilon - 1)}{3\epsilon_r + 3Gi(1 - \epsilon_r)}. \tag{3.2}$$

The geometrical factors G_i, i = 1, 2, 3 are used to calculate the change of the dipole polarizability due to the relative scales of the 3 principle axes (a_1, a_2, a_3), where

$$G_i = \frac{a_1 a_2 a_3}{2} \int_0^\infty \frac{dx}{(a_i^2 + x)\sqrt{(a_1^2 + x)(a_2^2 + x)(a_3^2 + x)}}, \tag{3.3}$$

which can be analytically calculated for prolate spheroids [33]. Figure 3.3 (c) shows how G_1 and G_3 and thus the plasmonic response of the spheroid changes as the relative dimensions of the spheroid are altered. Importantly, exciting the spheroidal particle along the long axis (a_1) produces a red-shifted dipolar resonance whereas exciting it along one of the two shorter axes (a_2, a_3) produces a blue shifted resonance.

Considering the coupled modes of the cut-wire, there is the transverse and longitudinal modes of a dipole chain. As such, the red shifting of the individual segment element resonance associated with the lengthening of the segment length *l* only affects the longitudinal mode, whereas the blue shifting affects the transverse mode. It is here where the cut-wire differs from a standard *un-cut* wire; it allows the presence of a LSPR orientated along the wire axis that can interact with TE waveguide modes. It's modal frequency can be altered through the geometric parameters *l* and *g*. Whilst the segment length *l* controls the shifting of the individual segment resonance, *g* controls the coupling between individual segments and thus the red-shift of the longitudinal mode away from the individual segment resonance. Thus, increasing *l* and decreasing *g* both lead to a red-shift of the cut-wire resonance, whilst the opposite is true for a blue-shift in the resonance. In figure 3.3 (d) we have shown this change in the modal frequency with *l* and *g* for a silver cut-wire with cross-section 30 $\times$ 50nm. The inset of figure 3.3 (d) demonstrates the typical cut-wire resonance

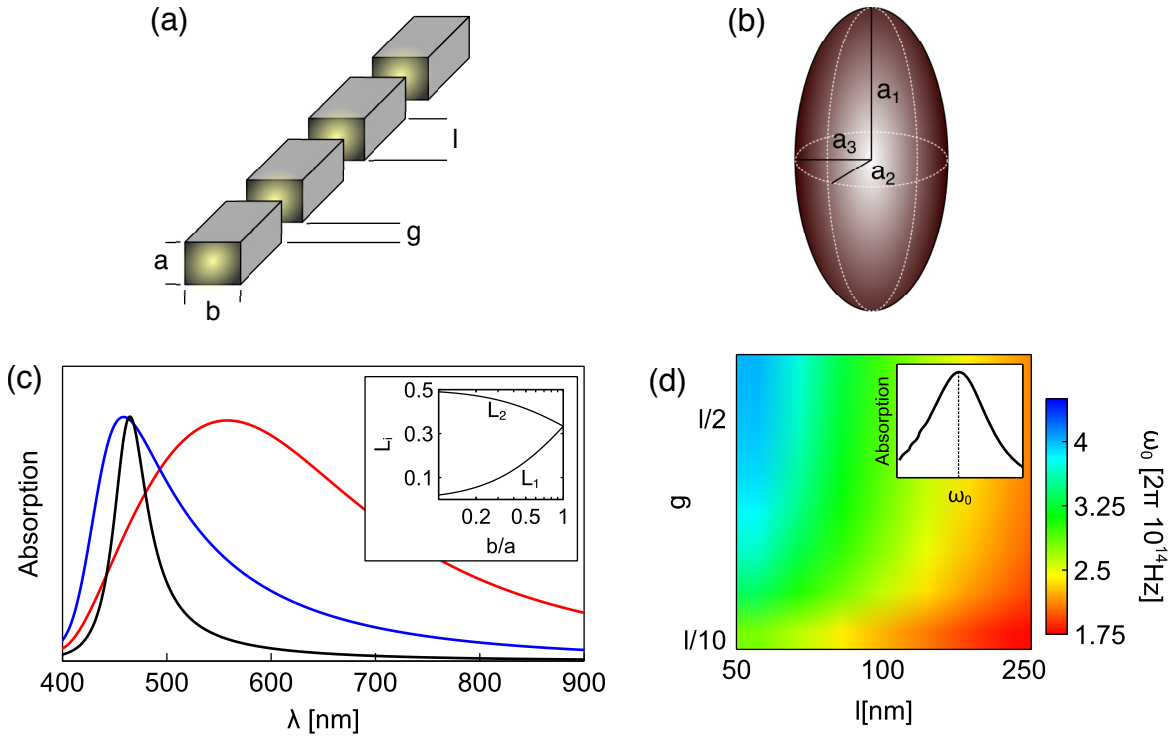

Figure 3.3: (a) Schematic of the cut-wire labeling the relevant parameters. (b) Schematic of a prolate spheroid. (c) Shift in the absorption spectra of a prolate spheroid for an incident field polarised along a_1 (red line) or a_2 (blue line) for the ratio $a_1/a_2 = 1.5$ (and $a_1 = a_2$, black line). The inset shows the change in the geometrical factors G_i as the ratio of the axes is changed. (d) Variation of the resonant frequency of the cut-wire as the parameters l and g are altered, for a constant cross-section of $a \times b = 30 \times 50\text{nm}^2$.

line shape.

Approximating the cut-wire as a prolate spheroid and using the coupled dipole equations of section 2.6 means we can calculate the absorption spectra of the cut-wire and fit these to numerical results to the inset of figure 3.3 (d).

3.5 Arbitrarily narrow transmission

We now move on to the interaction and mode hybridization of a TE waveguide mode with an array of cut-wires. To do this it is useful to consider a coupling matrix approach. We take a simpler approach, approximating the cut wire as a Lorentzian resonator with an energy E_p and a linewidth γ_p. Thus, E_p and γ_p can be calculated from fitting a lorentzian to the numerically calculated resonance. Furthermore, we consider only a single propagating TE waveguide mode being supported by the dielectric waveguide. The introduction of a periodic structure causes a

reflection of the waveguide mode at the band edge. Thus, within the first Brillouin zone, there are several branches of this TE waveguide mode, and at the band edges these are degenerate. The coupling between the branches of the waveguide mode and the LSPR of the cut-wires will only be significant when the frequencies of these resonances overlap. Thus, we need to consider three different modes, the two branches of the TE waveguide mode and the localised SP of the cut-wire. The coupling matrix can be defined as

$$\mathbf{H}\Psi = \begin{pmatrix} E_1 & V_{12} & V_{1p} \\ V_{21} & E_2 & V_{2p} \\ V_{p1} & V_{p2} & E_p + i\gamma_p \end{pmatrix} \begin{pmatrix} \psi_1 \\ \psi_2 \\ \psi_p \end{pmatrix}, \tag{3.4}$$

where E_1 and E_2 are the energies of the two unperturbed waveguide modes which are assumed to be loss-less (i.e. bound), E_p is the energy of the plasmonic mode, γ_p is the damping of the plasmonic resonance, V_{ij} represents the coupling of the modes i and j and ψ_i are the individual mode functions. There is no direct interaction between the two TE waveguide modes of the structure, i.e. $V_{12} = V_{21} = 0$, allowing the matrix to be somewhat simplified. If we now consider the special case that occurs when the waveguide modes are degenerate (setting $E_1 = E_2$) and coupling to the plasmonic mode is also symmetric (as occurs at the band edge) then diagonalising and solving for the eigenvectors (u) and eigenvalues (e) yields

$$\begin{aligned} u_1 &= \{\psi_1, -\psi_2, 0\}, & e_1 &= E_1, \\ u_2 &= \{V\psi_1/(e_2 - E_1), V\psi_2/(e_2 - E_1), \psi_p\}, & e_2 &= \frac{E_1 + E_p + i\gamma_p}{2} + \frac{\sqrt{\delta_{1p}^2 + 8V_{1p}^2}}{2}, \\ u_3 &= \{V\psi_1/(e_3 - E_1), V\psi_2/(e_3 - E_1), \psi_p\}, & e_3 &= \frac{E_1 + E_p + i\gamma_p}{2} - \frac{\sqrt{\delta_{1p}^2 + 8V_{1p}^2}}{2}, \end{aligned} \tag{3.5}$$

where $\delta_{1p} = E_p + i\gamma_p - E_1$ is the detuning between the waveguide and plasmonic modes. The modes of the WPP are u_2 and u_3, as we can see they are centered on the average of the energies and split by the factor of $\pm\sqrt{4\delta_{1p}^2 + 2V_{1p^2}}$. Thus, on resonance, the splitting is determined only by the coupling between the modes.

Interestingly, the third eigenmode which is only composed of bare TE waveguide modes and has an energy corresponding to that of a bare TE waveguide mode. This is, in theory, a loss

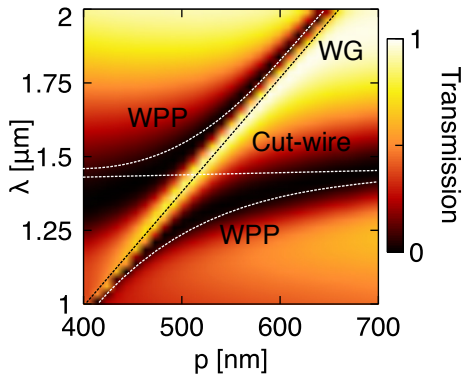

Figure 3.4: The transmission spectra of a cut-wire array on top of a waveguide when excited from the top by a plane wave as a function of wavelength λ and array period p, where l = 200nm and g = 40nm. The dashed lines show the position of the WPP modes and the positions of the original uncoupled waveguide and cut-wire resonances.

free mode, that corresponds to the high transmission seen in between the two WPP resonances [65, 15].

In figure 3.4 we plot the transmission spectra for an array of cut-wire resonators on top of the waveguide stack. This is calculated numerically using COMSOL. The dashed lines shows the energies of the bare cut-wire and waveguide modes, which are calculated and fitted numerically, as well as the modes from equation 3.5, which are fitted to the spectra by using the unknown coupling V_{1p}/δ_{1p} as a parameter.

The appearance of the WPP is shown in the in the transmission spectra of figure 3.4, where the cut-wire array is excited at normal incidence via a plane wave with the electric field parallel to the wire axis. The dips in the transmission spectra indicate the position of the hybridised WPP resonances (the geometric parameters of the waveguide are the same as used in figure 3.2). Also plotted are the frequencies of the cut-wire mode and bare-waveguide mode. The WPP resonances display the typical anti-crossing type behaviour of coupled resonances where the mode transfers from being plasmon-like to wave-like and vice versa. Finally, we can also see the appearance of a high transmission peak in between the two hybrid WPP modes, the EIT mode.

Narrow spectral plasmonic feature are potentially useful for sensing applications as small changes in the background refractive index can cause the transmission or reflection spectra to significantly alter [68]. Depending on the particular sensing application it can be useful to tune the resonant spectral features to the appropriate wavelength range. Through the parameters l and g the cut-wire

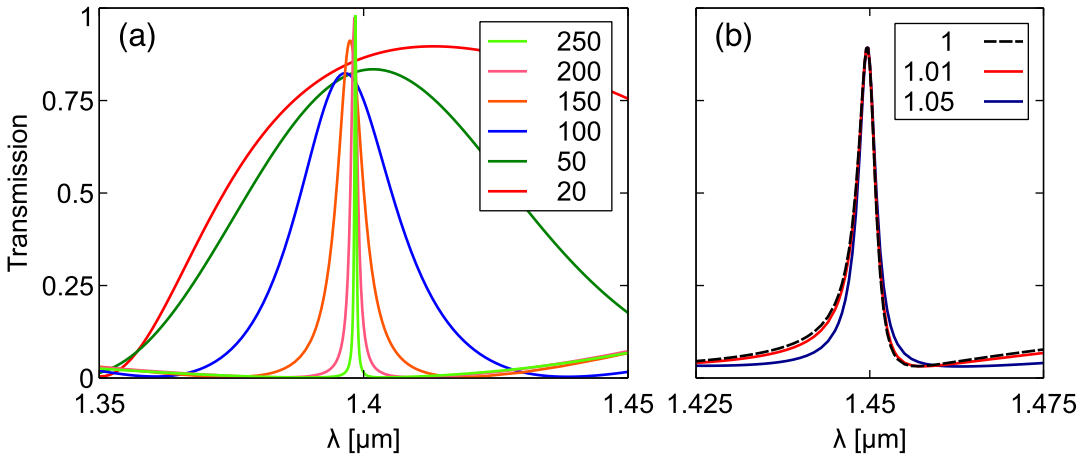

Figure 3.5: (a) Change in the transmission spectra with as the buffer height is altered from 20nm to 250nm. (b) Change in the transmission spectra as the refractive index of the area above the cut-wires is altered slightly from $n = 1$ to $n = 1.05$.

resonance can be shifted, whilst through the array periodicity p the TE waveguide mode can also be altered. Hence, the position of the transmission peak can be shifted over a wide range simply by the tuning of the geometric parameters. The narrowness of the transmission peak depends on the damping within the structure. As the cut-wires are only evanescently coupled to the TE waveguide mode the strength of their interaction scales exponentially with the buffer height. Thus, by tuning the buffer height it should be possible to reduce the strength of the interaction, decreasing the splitting between the two WPP branches whilst squeezing the transmission peak in between.

In figure 3.5(a) the height of the buffer layer is varied from 20nm to 250nm for an array with p = 500nm, l = 250nm and g = 50nm. As the buffer height increases strength of the coupling between the TE waveguide mode and the cut-wires decreases, causing the transmission peak to narrow and sharpens. In fact, such a mode can be reduced to have almost an arbitrarily narrow peak with a FWHM less than 1nm. Furthermore, in figure 3.5(b) we see the appearance of a Fano-type line shape. The Fano resonance occurs when background and a resonant scattering conditions interact. In this case, the spectrally broad cut-wire resonance acts as the background, interacting with the sharp Bragg resonance of the array. Thus, as the spectral position of these two resonances come closer together the shape of the peak shifts from a Fano-type shape towards a more Lorentzian line-shape. In general, the EIT transmission peak observed in WPP systems is a Fano-type resonance.

In figure 3.5 (b), the background refractive index of the superstrate layer is increased slightly

above 1 to analyse the change in the transmission spectrum. We can see that despite a change in the profile of the peak it's central wavelength does not shift due to the increase in background refractive index. Reconsidering our analysis of the WPP, the transmission peak comes from a mode that displays no plasmonic character and is independent of the cut-wire resonance. Therefore, although the LSPR of the cut-wire will be affected by the changed in background refractive index the bare waveguide modes are only slightly affected and thus the transmission spectrum only displays small changes. Slightly off-resonance there is a small change in the transmission peak of $\approx 5\%$ for $\delta n = 0.05$. However, typically these changes are of the order $\delta b = 0.01$ or smaller [68], and shifts based on SPP resonances can be an order of magnitude higher. This suggests that the EIT transmission peak of WPPs would not be useful for sensing of refractive index changes. However, recently there has been work [69] suggesting that the correct way to measure the improvement in sensitivity from the WPP is not to look at the direct change in spectral response. Rather, the effect of the WPP should be analysed by considering the relative change in the extinction spectra between a system with and without a WPP. As shown by Zhang and co-workers [69], this brings the enhancement in sensing of periodic plasmonic nanowire devices much closer to that of SPP based sensors.

However, recently there has been work suggesting that the correct way to measure the improvement in sensitivity from the WPP is not to look at the direct change in spectral response. Rather, the effect of the WPP should be analysed by considering the relative change in the extinction spectra between a system with and without a WPP. As shown by Zhang et al. [69], this brings the enhancement in sensing of periodic plasmonic nanowire devices much closer to that of SPP based sensors.

3.6 Summary

We have considered the differences between TE and TM waveguide modes with the conclusion that TE waveguide modes offer higher propagation distances and display changes to their modal profile whilst TM modes strongly couple to the metal and thus a large proportion of the mode energy resides in the buffer layer between the waveguide and metal. We have then considered the cut-wire plasmonic resonator, demonstrating its tunability using a spheroidal dipole modal and

CDA. Finally, we have shown the WPP is formed from he hybridisation of the plasmonic cut-wire mode with the TE waveguide mode and investigated the low-loss transmission mode which arises.

There are many other interesting properties of WPPs, such as their ability to slow light [65] and produce tailored photonic band splitting [70]. In the next section we shall consider this hybridised plasmonic-photonic mode further in the design of coupled resonator optical waveguides.

4 Cut-wires arrays as plasmonic CROWs

Cut-wires placed side by side
make a coupled resonator optical waveguide
The modes interact
to produce a band gap,
with the CROW mode resting inside

For arrays of increasing sizes
the quality factor rises
By tweaking this and that
we can make the band flat
and tune for potential devices

4.1 Introduction

Since their inception in 1999 [71] coupled resonator optical waveguides (CROWs) have emerged as an exciting technology that have the potential to revolutionise the integrated optics community. CROWs have the capacity to guide light on-chip and, as they enable dispersion control, have led to interesting phenomena in slow-light and enhanced light-matter interactions [72, 73, 74, 75, 76]. In particular, CROW designs have been extensively explored with a view to applications in areas such as optical switching [77], filters [78], delay lines [79], sensing [80] and wavelength conversion [81]. In general CROWs have been designed for photonics applications, using dielectric resonators such as photonic crystals and micro-ring resonators. Such resonances have narrow line-widths allowing

prospective CROW losses to be minimised.

In stark contrast to dielectric resonators plasmonic nanoparticles have broad lossy resonances yet allow the subwavelength confinement of light. When we are considering systems of directly coupled resonators the resonator loss impedes the waveguiding performance of such structures. For instance, typical propagation lengths along coupled dipole chains are less than 10 dipoles [82, 83]. As such, if we were to consider a directly coupled plasmonic CROW we would expect that the losses could render such a device useless for practical applications. However, not all CROW designs involve directly coupled resonators; the side-coupled scheme [84, 85, 86, 87], for example, enables the resonators to be coupled via a separate channel meaning that only a small fraction of the energy actually enters the resonators and no material losses occur in between resonator sites. Typically this extra channel is formed by using a waveguide and placing the resonators on top or to the side of it. In other words, the resonators are hybridised with the underlying waveguiding structure to produce new hybrid modes.

In this chapter we investigate the possibility of using cut-wire resonators to produce a plasmonic CROW. The broad lossy resonances of plasmonic nanoparticles interact strongly with light over a large frequency range. This strong interaction can be used to allow the tuning of the CROW over a wide range of frequencies as the cut-wire resonance is brought closer to the sharp waveguide resonance of the structure. Furthermore, the subwavelength size of plasmonic resonators at optical and infra-red frequencies would allow for a highly compact CROW design and stops the resonator size becoming a limiting factor in the design of CROW devices. By utilising the hybrid nature of the WPP in the side-coupled CROW scheme we expect to be able to minimise the impact of the plasmonic loss on the devices, in particular through the avoided coupling of the EIT. We then move on to investigate the resonant modes of a finite CROW structure before looking into how disorder (of both the resonator dimensions and resonator position) affects the characteristics of these cavity modes.

4.2 Coupled resonator optical waveguides

The term CROW was coined by Yariv in 1999 [71]. By taking a background material with a natural photonic band-gap and periodically introducing a resonance that has a frequency residing

within the band gap a new mode can be realised. The shape and the dispersion of the mode are dependent only on the resonant frequency of the resonator and the coupling between resonators.

This tunable dispersion has been a key driver in the potential application of CROWs to photonic circuitry. In particular, the ability to tune and design the group velocity of light propagating through a CROW has led to theoretical investigations on the stopping and storing of light coherently [75, 88, 76]. Slow light applications have also been of interest, in particular, optical buffering and delay lines, whereby the light passing through the CROW is stopped and later released. Moreover, reducing the group velocity of light can lead to vanishing dispersion [89] and enhanced non-linear interactions [90].

However, despite the clear interest in CROWs there are major difficulties when dealing with slow and stopped light. Disorder induced in the manufacturing process can limit the achievable slow-light group velocity as well as causing large losses in the propagation of light through the structures [91]. In particular, disorder can lead to extra extrinsic losses that are not present in ideal structures, namely scattering out of the slow-light waveguide [92] and field localisation at points with a local slow-group index [93]. These losses are predicted to increase with the inverse of the square of the group velocity [92]. It has been proposed that in-line amplification of the disordered slow-light waveguide could be used to compensate the losses due to the vertical scattering of light away from the waveguide [94], however, this would also coherently amplify any localised fields.

It is interesting to note that CROWs have so far generally been investigated using high quality resonators. As such, the potential benefits that lossy plasmonic resonators can bring to the configuration have been overlooked. There are obvious reasons for this, in systems where loss has to be carefully managed any intrinsic resonator losses can inhibit the system, and hence would be dis-regarded at the first instance. However, this ignores the benefits that broad resonances could bring to a CROW design. The broad spectral width of a plasmonic resonator provides a coupling constant that is active over a wide spectral range, allowing for a wide range in tunability of the potential mode dispersion. This has not been an issue for standard CROWs where the central mode is independent of the others and so can be almost tuned at will, but for side-coupled CROWs their is no natural band-gap for the resonator to reside and as such this wide range of coupling can lead to increased tunability. Furthermore, it is possible that broad plasmonic resonators may render the plasmonic CROW devices less susceptible to potential fabrication imperfections. The

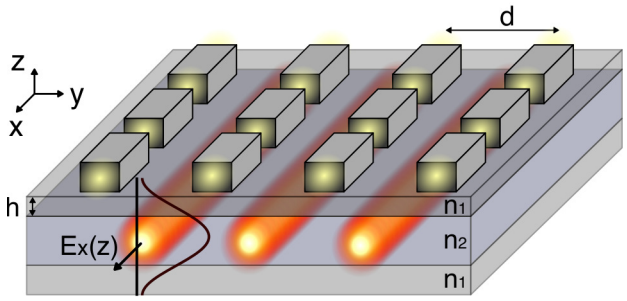

Figure 4.1: Schematic of the plasmonic CROW structure. The cut-wires are periodically spaced a distance *d* apart, with dimensions defined by *g*, *l* and a cross-section of 30×50nm. The slab waveguide has a central layer of height 100nm and index n_2, encased by two semi-infinite outer layers of index n_1. The cut-wires are situated in the top layer, a distance *h* from the central slab. Finally the expected field profile of the plasmoic CROW mode is also illustrated in the figure with the waveguide field hotspots appearing in between the cut-wires.

broad resonances are active over a wide spectral range and so, if small variations in the waveguide period occur, the plasmonic resonator will still be active at the corresponding frequency, mitigating the losses from the structure due to potential disorder.

Figure 4.1 shows the plasmonic CROW system that we have investigated. The cut-wires, with dimensions given by *g* and *l* and a constant cross-section of 50×30nm, are spaced periodically a distance *d* apart. The slab waveguide consists of a central layer of index $n_2 = 3.47$ (for example Si or GaAs) and height 100nm sandwiched between two semi infinite slabs of index $n_1 = 1.47$ (for example SiO_2). The cut-wires are located in the top slab, a distance *h* from the central layer. The field profile of the plasmonic CROW mode is also illustrated by figure 4.1 where we expect the coupling of the cut-wires and waveguide modes to produce the low loss EIT mode that avoids the cut-wire resonance.

4.3 Mode hybridisation theory

In order to understand the modes supported by the structure we first construct a simple model to investigate the expected behaviour of the system. If we treat each cut-wire as a harmonic oscillator that is driven by a time harmonic electric field of a waveguide mode we find that

$$\ddot{p} + \gamma\dot{p} + \omega_0^2 p = gEe^{-i\omega t}, \tag{4.1}$$

where p is the harmonic oscillator, E is the inclident electric field amplitude, ω_0 is central frequency of the oscillator, γ is the oscillator decay rate and g gives the coupling strength between the field and the oscillator. The harmonic oscillator equation is derived from the balancing of the forces on the oscillator; the total force (first term), the damping force (second term), the restoring force (third term) and the driving force (right-hand side). By rewriting the electric field as $Ee^{-i\omega t} = E_{tot} - E_{rad} - E_{res}$ we can match up the radiated electric field from the dipole E_{rad} with the damping term in the harmonic oscillator equation, i.e. $gE_{rad} = -\gamma\dot{p}$.

The excited oscillator can lose energy in any of three ways; either radiating energy away from the array, emitting directly back into the waveguide modes or dissipating the energy internally through Ohmic losses within the oscillator. By splitting the loss term $\gamma \rightarrow \gamma' + \kappa$, where κ is the decay rate of the mode back into the waveguide, then the electric field that is scattered back into the waveguide mode (E_s) can be written as

$$E_s = -\frac{\kappa}{g}\dot{p}. \tag{4.2}$$

After solving the harmonic oscillator equation this can be rewritten as

$$E_s = \frac{i\kappa\omega}{\omega_0^2 - \omega^2 - i\gamma\omega} Ee^{-i\omega t} = rEe^{-i\omega t}. \tag{4.3}$$

This allows us to write the reflection coefficient r in terms of the parameters of the cut-wire. As the field scattered into the waveguide scatters equally into both directions the transmission coefficient is $t = 1 + r$ and then the total transmission and reflection can be calculated as $T = |t|^2$ and $R = |r|^2$. To then consider the effect of the whole array we use a simple transfer matrix method to propagate the modes through each unit cell. Figure 4.2 illustrates how the modes entering a unit cell of the structure propagate through the period.

Within the transfer matrix formalism we describe the modes incident on the cut wire from either side of the unit cell. The waveguide modes (A_n and B_{n+1}) enter the cell from the left and right before propagating to the cut-wire, acquiring a phase of $\exp(ik_{wg}d/2)$ where k_{wg} is the wavevector of the waveguide modes of the slab, $k_{wg} = n_{eff}\omega/c$. At the center of the cell the modes are incident on the cut-wire, thus they are reflected, transmitted or absorbed through the losses of the resonator

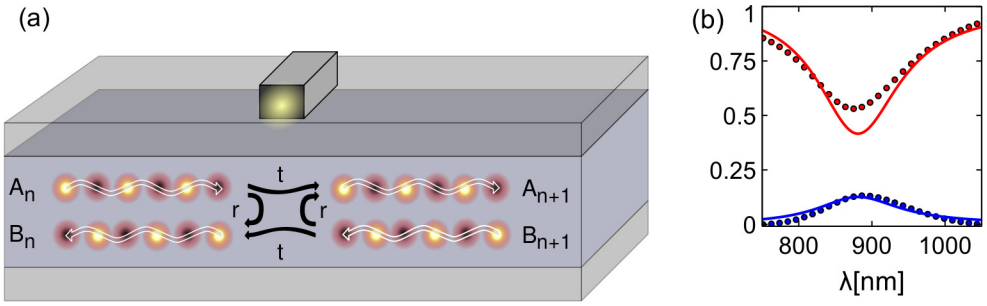

Figure 4.2: (a) Schematic of the interaction of the waveguide modes and cut-wire particle within a unit cell. The waveguide modes A_n and B_{n+1} enter the unit cell from either side and propagate towards the cut-wire where they couple to it. Part of the energy is reflected, part transmitted and part absorbed, before the waveguide modes exit the cell as A_{n+1} and B_n. (b) Example of the transmission (red) and reflection (blue) spectra of a single cut-wire excited by a waveguide mode given by the fitted theoretical model (lines) and numerical simulations (circles).

(γ'). After this the fields are propagated along the rest of the unit cell, acquiring another phase of $\exp(ik_{wg}d/2)$ before exiting (as A_{n+1} and B_n). By writing this as a matrix we have

$$\begin{pmatrix} A_{n+1} \\ B_{n+1} \end{pmatrix} = \begin{pmatrix} (t - r^2/t)e^{ik_{wg}d} & r/t \\ -r/t & e^{-ik_{wg}d}/t \end{pmatrix} \begin{pmatrix} A_n \\ B_n \end{pmatrix} = \mathbf{T} \begin{pmatrix} A_n \\ B_n \end{pmatrix}. \tag{4.4}$$

It should be noted that this equation is of the same form reported in other works for similar side-coupled resonator systems [84, 88, 95]. In order to calculate the band structure of the system we apply the Bloch boundary conditions $A_{n+1} = A_n e^{ik_y d}$ and $B_{n+1} = B_n e^{ik_y d}$. From the above equation it is clear that the eigenvalues of $\mathbf{T}$ must be equal to the Bloch vectors $e^{\pm ik_y d}$. We can simplify $\mathbf{T}$ by defining $C = r/(1 + r)$; solving for the dispersion relation of the structure gives

$$\cos(k_y d) = \cos(k_{wg} d) + iC \sin(k_{wg} d). \tag{4.5}$$

Thus we can use such a model to fit our results by varying the harmonic oscillator parameters (ω_0, γ and κ). In all that follows (unless otherwise stated) the periodicity of the array is d = 164nm such that the wavelength of the bare waveguide modes at the band edge is given by $\lambda_s = 1.0/(2dn_{eff})$ = 875nm and the buffer height h = 10nm. In general the results are normalised such that the frequency of the modes is divided by the frequency $\omega_s = 2\pi c/\lambda_s$.

Importantly, to provide a check on the model and our fitted parameters, we can also compare

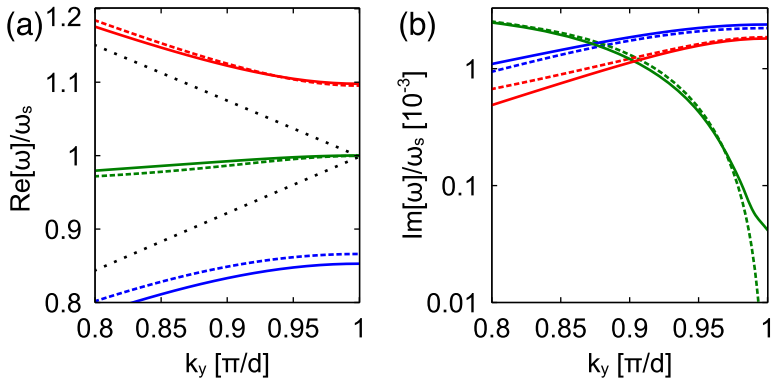

Figure 4.3: The dispersion relation for an infinite array of cut-wires with g = 20nm and l = 80nm. (a) The real and (b) imaginary parts of the dispersion band for numerical calculations (solid lines) and theory (dashed lines). Also shown are the bare slab waveguide modes (dashed black lines).

the single cut-wire transmission and reflection spectra to numerical simulations, an example of which is shown in figure 4.2 (b), where the parameters are $\omega_0 = 0.95\omega_s$, $\gamma' = 0.1\omega_0$ and $\kappa = 0.05\omega_0$. From this we can see that whilst the parameters do not produce a perfect match they do reproduce accurately the features of an individual resonator, only slightly overshooting on the transmission profile. One of the major reasons for this discrepancy is the inclusion of higher order waveguide modes in the numerical simulation which are not present in the analytical calculation. For all the fitted dispersion bands the fitted parameters of the decay rate κ and the cut-wire frequency ω_0 vary only slightly. However, the parameter γ' is an order of magnitude smaller. This is because in the single wire simulation the scattering of electric fields out of the system is large, whereas in an array interference effects from the scattering of other wires drastically reduce this parameter. In the next section we look at the dispersion bands calculated using COMSOL and fitted with our model.

4.4 Dispersion and tunability

The hybridization of the cut-wire array and the slab waveguide results in new modes which are illustrated by the coloured lines in 4.3 (a), for cut-wire dimensions of l = 80nm and g = 20nm. Both numerical (solid) and theoretical (dashed) results are shown, whilst the waveguide modes of the bare slab are also illustrated by the black dashed lines. As expected, the waveguide modes and the resonators hybridise to produce a band-gap where there is a large splitting due to the strong inter-mode coupling. Interestingly, a flat central band emerges. At the edge of the FBZ this central

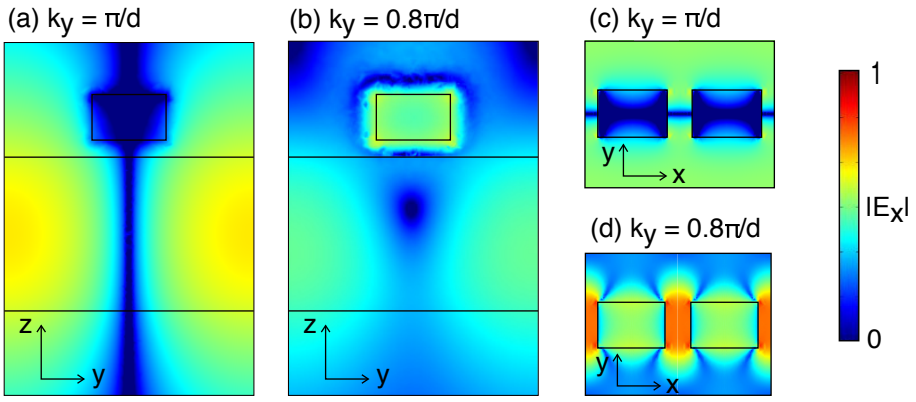

Figure 4.4: The numerically calcuated electric field profile $|E_x|$ of the central CROW mode (the green line in figure 4.3) at $k_y = \pi/d$ in the y-z (a) and x-y (c) planes and at $k_y = 0.8\pi/d$ in the y-z b) and x-y (d) planes. The colour scale is the same in all panels and it ranges linearly from 0 to 1 in arbitrary units. In panels (a) and (b) the field plot is taken vertically through the centre of the cut-wire segment . In panels (c) and (d) it is taken horizontally through the cut-wire segment.

band is composed entirely of forward and backward propagating waveguide modes with very little involvement of the cut-wires. This is to be expected as at this point the degeneracy in the forward and backwards waveguide modes leads to the formation of the WPP mode that is independent of the plasmonic resonator. It is important to note that this only strictly occurs at the band edge as elsewhere the waveguide modes are not degenerate.

This is further illustrated by field plots given in figure 4.4 where the magnitude of E_x is plotted in both the y-z (figures 4.4 (a) and (b)) and x-y (figures 4.4 (c) and (d)) planes for two different points along the central CROW band. At the band edge, $k_y = \pi/d$ the cut-wires are not excited as they sit in field nodes (see figures 4.4 (a) and (c)). However, it should be stressed that the central band is only present due to the cut-wire resonance enabling the coupling of the waveguide modes.

As the central mode is lacking its plasmonic character this suggests it could be low loss, as confirmed from the small imaginary part of the dispersion relation 4.3 (b). On the other hand, the central band only loses its plasmonic character close to the band-edge. At $k_y = 0.8\pi/d$ the losses associated with the central band are much higher as the CROW mode is at this point dominated by the cut-wire resonance, as demonstrated by the field plots in figures 4.4 (b) and (d). In the following we are mainly focused on the low-loss mode that appears in the system and as such we will focus our discussion on the central CROW band in the vicinity of the FBZ.

The simple transfer matrix model developed in the previous section provides a good match to

the dispersion relation as predicted by the rigorous numerical FEM calculations. There are some discrepancies between the two, notably the theory predicts a completely flat band, whereas, the "flatness" of the band is limited within the numerical simulations. These small discrepancies arise from modes that are not considered in the 3-band transfer matrix, namely the higher order waveguide modes. It is well known that a slab like waveguide supports many waveguide modes, and the higher order modes present in our system perturb the band structure due to their interactions with the cut-wire resonators. To check that this discrepancy arises from higher order waveguide modes we can expand the transfer matrix method to include these, as in appendix B, with the result being that the inclusion of more waveguide modes results in a curved dispersion of the central CROW mode, like those shown in figure 4.5.

Furthermore, the theory breaks down in its prediction of the loss of the central mode at the edge of the FBZ, see figure 4.3 (b). The theory predicts rapidly decreasing loss, which will actually produce a loss free mode at the band edge; in contrast the numerical simulations show that the band has finite losses. This discrepancy arises from the differing size of the cut-wires in simulation and theory. In the theory the cut-wires are considered as point-like resonators, whereas, in reality, the cut-wires have a finite spatial extent. As the mode profile of the fields at the band edge produces a node at the centre of the cut-wire the theory suggests this mode should be loss-free, but the loss of this band must be non-zero due to the finite overlap of the fields and cut-wires close to the nodal point, see figure 4.4 (a). Interestingly, this suggest that the loss of the mode will be sensitive to the cross-section of the cut-wire resonator, hence it could in principle be further decreased by reducing the resonator dimensions, whilst maintaining the resonator modal frequency.

A key feature of the central dispersion band is its gradual change in character as k_y is varied from across the FBZ. At $k_y = 0.8\pi/d$ the band is predominantly the cut-wire plasmonic mode, whereas when $k_y = \pi/d$ it has become solely a combination of waveguide modes, as shown by the field profiles of figure 4.4. This dramatic change of modal characteristics across the FBZ enables the shape of the mode to be manipulated through the variation of the geometric parameters controlling the resonance frequencies of the cut-wires and waveguide modes at the edge of the FBZ. Whilst the position of the band at the edge of the FBZ is fixed by the pitch of the array the cut-wire resonance determines the dispersion for $k_y < \pi/d$. Hence, by varying the frequency of the cut-wire mode ω_0 through the parameters g and l whilst keeping ω_s constant it is possible to

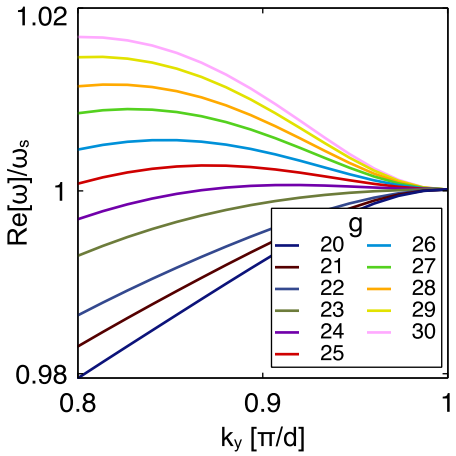

Figure 4.5: Change in the dispersion of the central CROW mode as g is changed linearly from g = 30nm (pink) to g = 20nm (dark blue), for an array with dimension l = 80nm. Calculated using COMSOL where all waveguide mode orders are present.

tune the shape of the band.

Figure 4.5 demonstrates how the central dispersion band can be altered by varying the cut-wire resonance ω_0 through the gap-length g over a small range. As we expected, the real part of the dispersion band changes and notably the sign of the gradient close to the band edge can be shifted from positive to negative values. This makes it possible to engineer the shape of the band whilst making it flat over a range of wavevectors. Clearly the ability to engineer this flatness is still limited as it is only possible to make the band completely flat close to the band edge due to the higher order waveguide modes that exist in the system and distort the band structure.

However, it is not possible to tune the loss dispersion through the cut-wire resonance (i.e. the parameters l and g). Considering all the bands in figure 4.5, the corresponding imaginary components of the dispersion are negligibly altered from the profile shown in figure 4.3 (b). This is to be expected as the loss of the central mode is due to the cut-wire resonances. The central mode still transitions from the high-loss cut-wire resonance to the low-loss waveguide modes as the FBZ is traversed, independently from ω_0 and as such it will always change from a high loss to a low loss mode.

Despite this, as the loss is mainly determined by the physical overlap of the electric field with the cut-wires it is possible to engineer the imaginary part of the dispersion by moving the cut-wires further away from the field hot-spots. In figure 4.6 we steadily increase the height of the buffer layer between the central waveguide slab and the cut-wires (h), whilst maintaining the condition

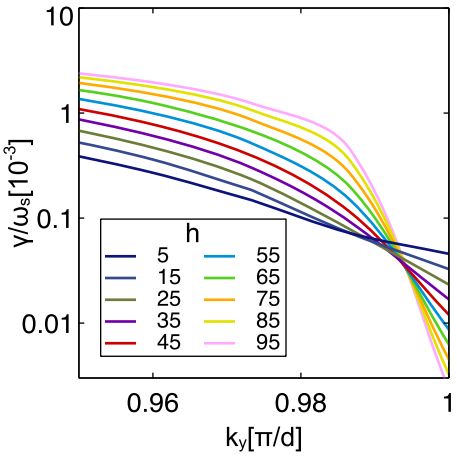

Figure 4.6: Change in the imaginary part of the dispersion relation of the central CROW mode as *h* is increased from 5nm (dark blue) to 95nm (pink) in steps of 10nm, for an array with dimensions *l* = 80nm and *g* = 20nm. Calculated using COMSOL where all waveguide mode orders are present.

that $\omega_0 \approx \omega_s$. As shown, the loss of the mode can be further reduced, but only very close to the edge of the FBZ where the loss reduces exponentially with *h*. Counter-intuitively, when we are away from the band edge the increased buffer height leads directly to an increase in modal loss. This occurs because when the spacer layer becomes larger we are reducing the coupling between the plasmonic and waveguide system modes, allowing the central mode to maintain its cut-wire character further along the FBZ.

4.5 Cavity modes

We now turn our focus towards finite arrays of cut-wires and the modes that result. Considering the band structure of the plasmonic CROW device, we can see that their will be an impedance mismatch between the CROW modes and a bare waveguiding structure. Thus, the boundary at the edge of the CROW will inevitably induce reflections due to this modal mismatch [96]. Despite the fact that the frequency mismatch between the central CROW mode and the bare waveguide modes (see figure 4.9 (a)) the differences in band curvature lead to a mismatch in the group velocity which causes the mode reflection. In other words, the flat nature of the central band, and its associated slow group velocity, originates from the interference of the two counter-propagating waveguide modes. This interference pattern cannot be matched to the bare waveguide modes. These modal reflections at the edge of the array suggest that a finite array of cut-wires coupled to

the multilayer waveguide will support Fabry-Perot (FP) modes. Thus, as with all FP resonators, the modes exist at frequencies which cause an $n\pi$ phase change from one end of the resonator to the other (where m is an integer). By defining the start and enf of the finite CROW structure to be the centre of the first and last cut-wires we find that the expected wavevectors of the modes are

$$k_n = \frac{n}{n_w - 1}\frac{\pi}{d}, \qquad \text{n} = 1,\ 2\ n_w - 2, \tag{4.6}$$

where n_w is the number of cut-wires in the array. We can use this to compare the modes of both the infinite and finite structure, as shown in figure 4.7 (a) where modes n = 18, 17 and 16 (dots) are compared with an infinite array (solid lines) for n_w = 20, l = 80nm and g is 20nm (blue), 25nm (grey) and 30nm (green). The eigenmodes of the finite structure agree well to the dispersion bands of the infinite structure using the wavevectors provided from equation 4.6. The electric field profiles of modes 18, 17 and 16 are shown in figures 4.7 (b), (c) and (d) for g = 30nm, corresponding to the green dots in figure 4.7 (a). From this we can see that, for the FP resonances of the finite cut-wire arrays, the avoided coupling of the central dispersion band is retained by the finite modes. The field hotspots of the modes are located within the central waveguiding layer, in between the cut-wire resonances. However, due to the nature of the FP resonances, the phase change across the array means that this avoided coupling is not preserved across the whole array. The array acts like a closed cavity, with the modes clamped at either end, producing standing wave resonances. The higher order modes (such as modes 16, 17 and 18) are the modes with the most nodes in their standing wave envelope, but the standing wave would need 20 nodes in order to to have nodes at all the cut-wires within the array. Thus, it is not possible for the avoided coupling mode profile of the infinite CROW central band to be completely preserved in the finite array FP resonances.

There are several loss mechanisms that dissipate energy from the finite CROW cavity mode. We divide these into three categories; radiation losses to to free-space (γ_r), Ohmic losses within the metallic cut-wires (γ_d) and coupling of the energy into waveguide modes (γ_{wg}). For a useful device is important to understand how these loss mechanisms can be controlled. Whilst the losses to free-space and metallic dissipation permanently remove energy from out system, losses to the waveguide modes can be utilised in a potential device. The scattering out of the array and the Ohmic losses come from the excitation of the cut-wire particles. We note that the finite modes

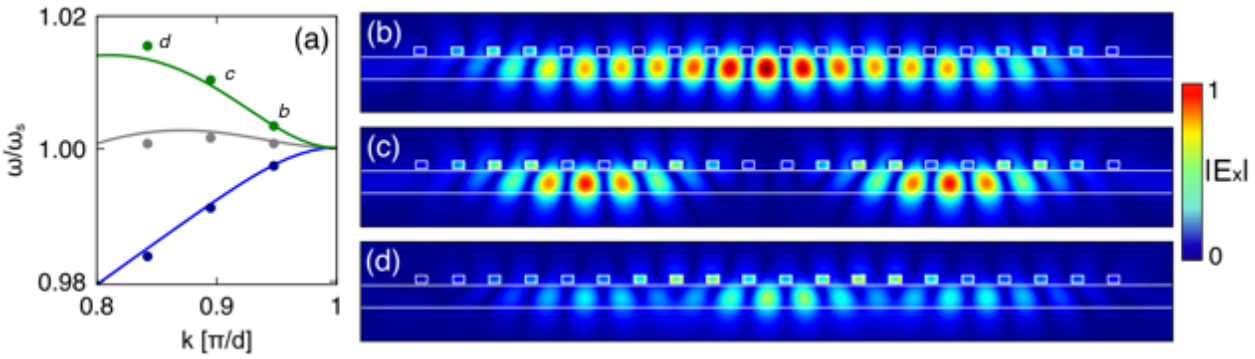

Figure 4.7: (a) Comparison of the dispersion relation (lines) and eigenmodes (dots) for arrays with g = 20nm (blue) g = 25nm (grey) and g = 30nm (green). The eigenmodes are found for finite arrays with 20 cut-wires. (b), (c) and (d) $|E_x|$ of the three highest order modes of an array 20 cut-wires with g = 30nm. From Equation 4.6: (b) mode 18, (c) mode 17 and (d) mode 16. The colour scale ranges from blue (minimum) to red (maximum).

have envelope functions, and the nodes in the envelope functions correspond to excited cut-wires. The number of nodes in the envelope function corresponds to $n_{nodes} = n_{wires} - n$, thus the overall loss rate off the modes will be highly dependent on the mode number n. Interestingly, in the context of loss compensation, this leads to strong modal discrimination whereby the highest order modes is favoured due to its decreased loss rate. This could be desirable when designing laser cavities [97]. The quality factors (Q = Re[ω]/2Im[ω]) of modes 18, 17 and 16 from figure 4.7 are 544, 242 and 195 respectively, displaying the high dependence of modal loss on the number of nodes in the envelope function.

Figure 4.8 (a) shows how the highest order mode loss rates are affected by the number of wires in the array. Perhaps most remarkably, the overal total loss rate decreases with increasing array sizes. This is despite the fact that silver is a lossy material, which is counter intuitive as an increased amount of silver does not equal an increased modal loss. Instead, the increased number of wires causes the highest order mode to be displaced, shifting the field hotspots further into the centre of the gaps between the cut-wires. Thus, the increased number of wires leads to a decrease in the overlap between the highest order mode and the cut-wires, reducing the modal loss. Not only does the dissipative Ohmic loss decrease, but the radiative and waveguide losses also decrease with an increasing array size. As the array size increases, the position of the highest order mode along the dispersion band shifts towards the WPP resonance at $k_y = \pi/d$. Thus the mode comes closer to the zero group velocity point, leader to an increasing mismatch between the

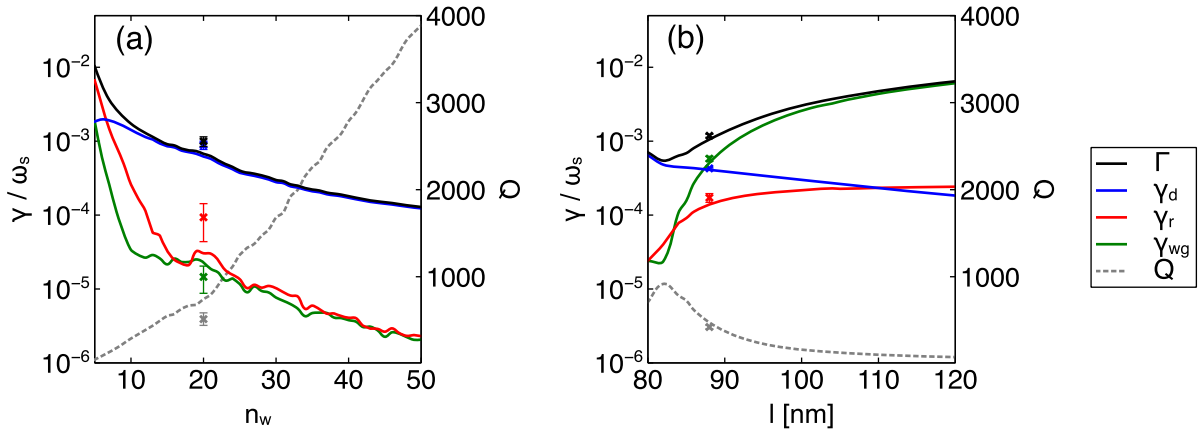

Figure 4.8: Change in the fundamental mode loss rates. The four rates are: Γ, total losses, γ_d, dissipative losses, γ_{wg}, losses into TE_0 waveguide mode and γ_r, other radiative losses, and Q is the Q-factor. (a) Change in the loss rates with increasing number of wires in the array; the results shown are for an array of wires with l = 80nm and g = 25nm. (b) Change in the loss rates with an increasing cut-wire detuning; the results shown are for an array of 20 wires and g = 25nm. The points and error bars represent the mean and standard deviation of the randomly disordered CROW from table 4.1 with δ_y = 2.5nm

highest order mode and those outside the array, causing the decrease in modal loss rates. From figure 4.8 (a) we can also see the Q-factor of the highest order mode, which for an array of 50 cut-wires is approximately 4000. This is very high for a plasmonic structure, but it is not an upper limit. As the array size continues to increase so would the modal losses, until they reached the theoretical minimum displayed in the infinite system[1].

Now we focus our attention on tuning the separate loss parameters through the CROW geometry. For figure 4.8 (a) the dissipative loss dominates and there is very little scattering, either out of the array or into the waveguide modes. However, the ratio of these losses can be tuned through the geometry of the system. By slightly detuning the plasmonic resonator away from the WPP point, i.e. $\omega_s \neq \omega_0$, the ratio of the losses can be shifted, as shown in figure 4.8 (b). We detune the cut-wire by steadily increasing the segment length l whilst keeping fixed g = 20nm and n_w = 20. As shown in figure 4.8 (b), this detuning can drastically shift the losses away from the dissipative absorption in the metal to coupling out of the array via waveguide modes. As the cut-wire resonance is detuned from the WPP point it becomes decreasingly excited by the modes

[1]The losses in the finite system will always remain higher than in the infinite system because it is only in the finite CROW where scattering losses out of the array exist. However, even in the case of only 20 wires the loss can be dominated by the dissipative loss in the metal, and the overall loss of the finite array is very close to that of the infinite array (at the wavevector given by equation (4.6)).

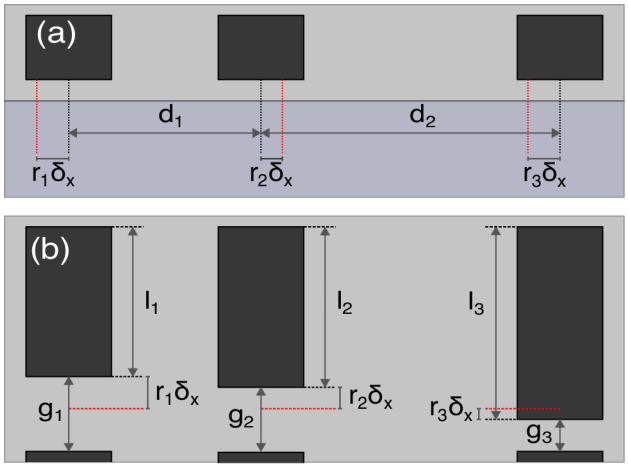

Figure 4.9: Schematic of the two types of disorder considered. (a) disorder in the spacing of the resonators. (b) disorder in the lengths l_i and g_i leading to a displaced cut-wire resonance.

of the array, thus decreasing the dissipative absorption. At the same time, the slope of the band is increased, thus decreasing the mismatch in group velocity between the modes of the array and the free waveguide modes, therby increasing the waveguide loss rate. This enables an increased outcoupling efficiency to the waveguide modes, at the cost of a decreased Q-factor. Whilst it is desirable to produce low-loss cavities, the ability to tune the individual loss channels is appealing for certain devices. For instance, if the cavity was used for a laser we would require some method of extracting the light, whereby the increased loss to the waveguide modes would become a benefit. Finally we note that Q-factors over 100 can be achieved even when the waveguide losses are as high as 87% of the total cavity loss.

4.6 The effect of disorder

As previously mentioned, the robustness of the modes and loss rates of the plasmonic CROW against disorder is of importance when considering its potential uses. There are many possible forms disorder and imperfection could take in our system and to investigate them all would be almost impossible. Therefore, in order to give a general idea of the effect of disorder, we have limited ourselves to considering disorder in two parameters, the spacing of the CROWs d and the resonant frequency of of the cut-wires (through parameters g and l). We can calculate how the fundamental mode of the system is altered when random disorder in these two parameters is incorporated.

Table 4.1: Effect of disorder on the frequency and decay rates of the fundamental CROW mode for n = 20 and g = 25nm. All quantities except Q are in units of rads^{-1}. The mode frequency is not shown as for all l = 80nm simulations it is $2.154 \times 10^{15} rads^{-2}$ and for all l = 88nm simulations it is $2.148 \times 10^{15} rads^{-1}$.

		Im[ω] [10^{11}]	γ_d [10^{11}]	γ_r [10^{11}]	γ_{wg} [10^{11}]	Q
	δ_y = 0nm	2.19	2.06	0.07	0.06	782
l = 80nm	δ_y = 1nm	2.76 ± 0.40	2.55 ± 0.35	0.14 ± 0.05	0.07 ± 0.01	635 ± 100
	δ_y = 2.5nm	3.42 ± 0.51	3.04 ± 0.39	0.32 ± 0.17	0.05 ± 0.02	513 ± 72
	δ_y = 0nm	3.94	1.43	0.48	2.03	434
l = 88nm	δ_y = 1nm	3.95 ± 0.06	1.44 ± 0.01	0.51 ± 0.03	2.01 ± 0.05	432 ± 7
	δ_y = 2.5nm	4.06 ± 0.19	1.47 ± 0.03	0.59 ± 0.08	1.99 ± 0.15	422 ± 20

Firstly we consider the random disorder in the resonator spacing. For an array of n_w = 20 each cut-wire would normally be spaced by a distance d. Now each resonator i is moved by a distance $r_i\delta$ where r_i is a random number between -1 and 1 and δ is a distance to be decided, as shown by figure 4.9 (a). 10 different random distributions were considered and the mean and standard deviation loss of the rates and Q factors are shown in table 4.1.

It is well known that the effect of disorder closer is highly dependent on the group velocity of the mode, and as the mode becomes slower the effects of disorder become much more pronounced [92]. Thus, as the detuning of the cut-wire from the array resonance alters the curvature of the band the effect of disorder will also depend on the relative detuning of the cut-wire from the array. To make sure this is considered, the disorder simulations were conducted for two separate cut-wire lengths l = 80nm and 88nm. This gives the fundamental frequencies of $\omega \approx \omega_s$ (l = 80nm) and a small detuning of $\omega = 0.997\omega_s$ (l = 88nm). From table 4.1 we can see that when the detuning is small, l = 80nm, the effect of disorder is relatively large, potentially increasing the uncertainty in the Q-factor of the resonance by roughly 20%, The disorder generally increases the loss rates but has a significant impact on the radiation loss leading to an increased scattering out of th array, it also strongly influences the disspipative loss. Interestingly the effect of disorder is drastically reduced for even small detunings of the frequencies. Even for a relatively large disorder range of $\pm$2.5nm the effect on the Q-factor is minimal and the loss rates are only slightly altered from the values of the perfectly organised array. The effect of structural disorder on the loss rates is also shown as error bars in figure 4.8 (a) (l = 80nm) and figure 4.8 (b) (l = 88nm).

When considering the disorder in the resonator frequency (i.e. the cut-wire dimensions) we

Table 4.2: Effect of disorder on the frequency and decay rates of the fundamental CROW mode for $n = 20$ and $d = 164$nm. All quantities except Q are in units of rads^{-1}.

		Im[ω] [10^{11}]	γ_d [10^{11}]	γ_r [10^{11}]	γ_{wg} [10^{11}]	Q
l = 80nm	δ_x = 0nm	2.19	2.06	0.07	0.06	782
	δ_x = 2.5nm	3.20 ± 0.71	2.25 ± 0.45	0.68 ± 0.20	0.23 ± 0.22	560 ± 114
l = 88nm	δ_x = 0nm	3.94	1.43	0.48	2.03	434
	δ_x = 2.5nm	3.95 ± 0.5	1.47 ± 0.06	0.67 ± 0.17	1.80 ± 0.46	440 ± 58

are slightly limited by the numerical simulations. The cut-wires are simulated only over a single segment and gap length with periodic boundary conditions. Thus in order to maintain the simulation size we require that the length $l_i + g_i$ remains constant for all wires. In order to accommodate for this, the disorder in the cut-wire resonance, a random length ($\delta_x r_i$), is added to l and also taken away from g thus maintaining $l_i + g_i$ = constant. This is shown visually in figure 4.9 (b). For this disorder we also consider the same two resonator tunings l = 80, 88nm and the results are shown in table 4.2. Note that this small change g and l, as limited by our simulation, means the effect of disorder is compounded as the small increase in l (g) causes a decrease in g (l); meaning the resultant blue-shift or red-shift is greater than what would be caused by a change in l or g alone. Whilst we would expect disorder in both l and g in our simulations, these two would not be correlated, and would not, in general, work together in compounding the frequency shift. As such the simulation setup is likely to overestimate the effect of resonator disorder.

Similar to the case of array disorder, resonator disorder leads to a large change in the overall loss rates and Q-factor in the case of l = 80nm, causing a drastic increase in radiative ($\times$10) and waveguide ($\times$ 3) losses. Furthermore, we find that for a resonator is has a slight detuning, a little away from the slow light point in the mode the disorder leads only to a larger range in the expectation of the losses and Q-factor, not directly to increased losses.

Overall, for both resonator and array disorder, the extrinsic losses due to small fabrication imperfections do not appear to drastically reduce the performance of the mode. We have seen that for a mode that is tuned at $\omega_0 = \omega_s$ that random disorder or $\pm$2.5 can cause an increase in overall modal losses of $70 - 100\%$ and reduce the Q-factor by up to a factor of 2. In contrast, for relatively small detunings, which could also be desirable due to the fact that a larger proportion of the mode energy is lost to waveguide modes. The losses are only increased by around 10%, with a correspondingly small decrease in the quality factors of the mode. As such, the high-quality

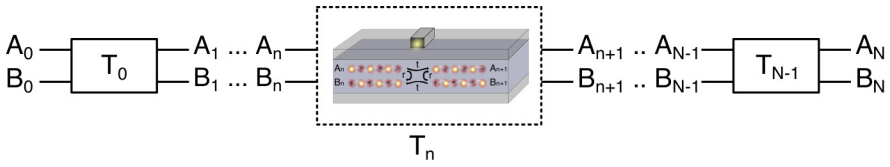

Figure 4.10: Schematic of the transfer matrix method for finite cut-wire arrays.

CROW modes of these cavities appear to be reasonably robust against disorder, and particularly robust for small detunings away from the waveguide resonance.

4.7 Transmission characteristics

Finally, we conclude our analysis of the finite cut-wire CROW structure by considering its applicability for applications. We do this by considering a passive structure, looking at transmission properties and the potential for use as a delay line or other slow-light device. The point here is not to provide an overall finished device but to test whether there are any reasons that such a device should be impractical.

As already stated, so far CROW designs have been suggested for integration as delay lines and optical buffers. To investigate these kind of applications we can extend the theoretical approach we used in the previous section to consider finite arrays of N resonators. In this method, the forward and backward propagating waveguide modes at the left hand side of the structure (A_0 and B_0) are propagated through the array by subsequent transfer matrices. Hence, the modes A_0 and B_0 are transferred into the modes A_1 and B_1 via the matrix $\mathbf{T}_0$; iterating this process throughout the array we find that

$$\begin{pmatrix} A_N \\ B_N \end{pmatrix} = \mathbf{T}_{N-1} \ldots \mathbf{T}_n \ldots \mathbf{T}_0 \begin{pmatrix} A_0 \\ B_0 \end{pmatrix} = \mathbf{T}_{tot} \begin{pmatrix} A_0 \\ B_0 \end{pmatrix} . \tag{4.7}$$

This is process is illustrated graphically in figure 4.10. If we input a waveguide mode of arbitrary amplitude 1 from the left ($A_0 = 1$) and assume that there is no field incident from the right ($B_N = 0$)

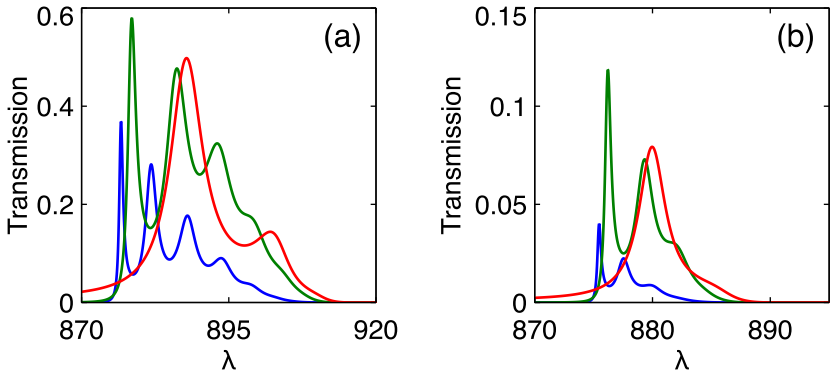

Figure 4.11: Transmission spectra of three different CROW structures; n=30 (blue line), n= 10 (red line) and n=30 adiabatically matched CROW (green line) for two different detunings $\omega_0 = 0.95\omega_s$ (a) and $\omega_0 = 0.98\omega_s$ (b).

then we can solve for the reflected (R) and transmitted (T) amplitudes as

$$\begin{aligned} R &= \frac{-T_{tot,21}}{T_{tot,22}}, \\ T &= T_{tot,11} - \frac{T_{tot,12}T_{tot,21}}{T_{tot,22}}. \end{aligned} \tag{4.8}$$

Note, when constructing the transfer matrix through the array the method can become numerically unstable, as small transmission coefficients in the denominator cause numerical errors, and lead to transmission and reflections coefficients of > 1. To overcome this the transfer matrix can be reformed as the scattering matrix [98].

For use with passive devices the losses of the plasmonic CROW need to small enough such that a large transmission efficiency can be achieved. When considering the transmission of a waveguide mode through the CROW there are two important loss channels; the intrinsic CROW losses and the coupling losses by transferring from a waveguide mode to the low group velocity CROW mode. To overcome the coupling difficulties encountered it is possible to use adiabatic coupling methods (whereby the group velocity of the mode is slowly changed) [99, 96] enabling high coupling into and out of the CROW mode.

Figures 4.11 (a) and (b) show the transmission spectra for two different cut-wire resonances $\omega_0 = 0.95, 0.98\omega_s$ corresponding to theoretical group velocities of $v_g = 0.05c$, $0.02c$ (as calculated from the derivative of equation 4.5 at $k_x = 29\pi/30d$). The parameters κ and γ' are set at $0.05\omega_0$ and $0.01\omega_0$ respectively (used to fit the infinite array band structure). We consider three different

arrays, one of length n = 10 cut-wires (red line), one of length n = 30 and one of length n = 10 but with an adiabatic matching period of n = 10 either side of the array (making a total length of 30 cut-wires). Within the adiabatic matching period the coupling strength κ is linearly reduced to zero. This could be done by steadily increasing the buffer height between the core layer and the cut-wires in the adiabatic regions. We can see that as the size of the array increases, despite the fact that the finite modes of the finite array have higher Q-factors, the overall transmission through these modes decreases (see red and blue lines). In fact, for the small detuning of $\omega_0 = 0.98\omega_s$ (figure 4.11 (a)) the transmission efficiency is less than 5% for an array of 30 wires close to the fundamental mode frequency. This can be increased by the adiabatic tuning of the coupling constant either side of the CROW to around 12% but it cannot be increased much further. When the detuning is a little larger (figure 4.11 (b)) the transmission efficiency with and without the adiabatic matching periods become 38% and 59% respectively.

The delay time of array of 30 cut-wires (without adiabatic matching period), detuned at $\omega = 0.98\omega_s$ is 79ps, at a wavelength of 875nm, has a transmission of approximately 4%. If we compare this to a recent study [100], tuned to communications wavelength 1550nm, a delay of 90ps is achieved with a transmission of only 10%, which is very comparable. Similarly the cut-wire CROW has a comparable bandwidth of 40GHz. From this, it appears that incorporating plasmonic resonators into CROW structures does not limit their potential applications for optical delay devices. However, this it not really a fair comparison as we are comparing theoretical results that do not include fabrication losses and losses due to array disordering to achieved experimental results. Thus, in a full experimental comparison where fabrication losses are present we would expect the performance of the plasmonic CROW to be reduced when compared with the theoretical calculation. Finally, it should be noted that by using the value of γ' that fits the band dispersion we have underestimated the total losses of the array as it neglects the scattering out to radiative modes. However, as γ' include both the radiative and dissipative losses, and as the dissipative losses dominate for the highest order mode (see figures 4.8 (a) and (b)) this should only result in a small change to the overall transmission of the array.

4.8 Summary

In this chapter we have investigated the array of cut-wires placed on top of a dielectric waveguide. Moreover, we have considered this system as a type of CROW and investigated how the dispersion bands can be tuned easily through the geometric parameters. As in the case of the WPP, the degeneracy of the bare waveguide modes at the edge of the FBZ enables the creation of a low-loss hybrid mode. Through the individual cut-wire resonance, we can tune the shape of the real part of the dispersion band, whilst the model losses are highly dependent on both position in the dispersion band (i.e. whether the mode is more cut-wire-like or waveguide-like) and also on the strength of the coupling, controlled through the buffer height.

When looking at finite systems, these arrays form Fabry-Perot type resonances that treat the ends of the array as mirrors. The modal losses of these cavity modes are not equal, with the highest order modes producing the lowest loss as they excite the least number of cut-wires. As the finite size of the array is increased the Q-factor of these modes increases sharply, providing cavity modes with Q-factors of 4000 and above, highly unusual for plasmonic resonators, and arising from the hybridised nature of the modes. Furthermore, the individual loss mechanisms of these finite CROWs can be tuned directly through the geometry, by changing the detuning between the cut-wire resonances and the bare waveguide modes at the edge of the FBZ. This allows the modal losses to be transferred from dissipative absorption to radiative waveguide modes, whilst also decreasing the Q-factor.

We have also considered briefly the effect of random disorder in both the array period and the resonator frequency. The modes are heavily affected by disorder, leading to an increase in losses of around 60% for modes with no detuning. Interestingly, by increasing the detuning slightly the modes become much more robust against disorder, barely increasing the overall loss rates. Finally, we have extended the theoretical model to consider whether using plasmonic cut-wire resonators instead of traditional dielectric resonators within the CROW impedes the performance for slow light devices.

5 Spoof plasmon polaritons in slanted geometries

5.1 Introduction

Since the middle of the last century it has been known that waves can propagate along a structured metallic surface. In 1950, Goubau [101] demonstrated that a cylindrical metal coated by a threaded dielectric enables a mechanism for the control and enhancement of the surface wave through the periodic corrugation (threading). Similarly, in 1973, Ulrich showed how a meshed conductor can support propagating TM surface waves along it's interface [102]. Despite these and other studies it wasn't until the last decade that the formalism of spoof plasmon polaritons was introduced. The discovery of EOT by Ebbesen in [13] was one of the key drivers here. Originally, EOT was observed at optical frequencies where propagating SPPs could be excited along the metal interface, and before long it was shown that SPPs play an important role in the resonant enhancement of light through subwavelength holes in a metal film [63]. However, when EOT was also observed in frequency regimes where no SPPs would be confined to the metal surface it was necessary to consider what other mechanism was taking over the role of the surface plasmon polariton. It is within this context that the spoof surface plasmon polariton was born. In 2004 Pendry and co-workers demonstrated that a periodic array of holes in a perfectly conducting surface would produce surface waves that mimicked the behaviour of surface plasmon polaritons [24]. It is the plasma frequency of metals (a predefined material property) that defines the frequency regime where the SPP becomes plasmon-like. Interestingly, with spoof SPPs an analogous plasma frequency can be defined (the spoof plasma frequency), one which now depends only on the geometric parameters of the system. In other words, here was a system with SPP like behaviour (the spoof SPP) where the spoof SPP characteristics depended only on the geometry of the surface.

Thus, spoof SPPs became an early example of the metamaterial paradigm, whereby the prop-

agation of light is controlled through the geometry. Importantly, the concept of a geometric plasma frequency means that the plethora of surface plasmon phenomena and physics can be transferred to perfectly conducting metals who have no natural plasma frequency, or real metals in frequency ranges far below their natural plasma frequency. Employing the metamaterial paradigm, the propagation of spoof SPPs on surface structures has been thoroughly explored theoretically for a range of structures including simple planar structures [103, 104, 105, 106], wires [107, 108], single grooves [109], wedges [110], metafilms and surfaces [111, 112]. Furthermore, there have been many experiments demonstrating the existence of spoof SPPs [113, 114, 115, 116, 117, 118, 119] and they have been suggested as a means of achieving slow-light [120], THz circuitry [121], broadband transparency [122], directional beaming [123], and non-reciprocal dispersion [124].

The theoretical works cited above have focused almost exclusively on rectangular corrugations (with the exception being the investigation of cylindrical indentations). Whilst the propagation of spoof SPPs along different geometries, such as wedges and wire structures, has been considered, the actual corrugation that leads to the spoof SPP has been altered very little, generally maintaining a rectangular cross-section that is perpendicular to the surface. Because of this, there remain questions over how the shape of the corrugation can affect the spoof plasmon characteristics. So far it has been the groove height, h, that determines the spoof SPP plasma frequency (with $\lambda_p = 4h$) with the justification that the indentations act as a type of cavity, which is closed at the bottom and open at the top. It remains to be seen whether the quantity h is the relevant quantity for a groove of arbitrary shape, or if in fact a relevant quantity can even be defined in such a case.

Unfortunately, it is difficult to have a tractable and manageable theoretical solution to the surface modes of an arbitrarily shaped corrugation. From a theoretical perspective we are constrained to produce a solution of the wave equation, where the appropriate boundary conditions define our mode. However, even if we confine ourselves to a function definition such as $z = f(x)$ along the boundary, using this to find the modes of the general modes of the system is difficult. Thus, instead of solving for an arbitrary groove shape, in this chapter we start with a simple small change to the standard spoof geometry to understand how changing the surface indentations affects the spoof SPP modes. We introduce the parameter θ which controls the angle at which the rectangular grooves are inserted into the surface of the metal, thereby adding a simple rotation to the grooves. By transforming the fields within the grooves we can still exploit the rectangular geometry when

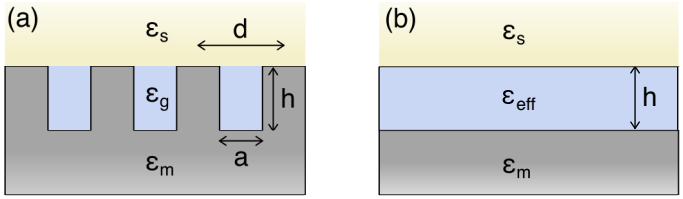

Figure 5.1: Schematic of the material layout for (a) mode matching and (b) effective index methods. In the effective index method the layer of the metal with corrugations is replaced by a medium with dielectric constant ε_{eff}.

deriving the solution to the wave equation, making the problem tractable. Such a set-up should allow us to probe the effect of changing the groove, and to consider more generally what are the relevant parameters in defining our spoof SPP plasma frequency. Also, by using a rotation we can consider the effect of asymmetry on both the spoof SPP dispersion relation and the EM fields of the modes. Finally, as a limiting case of the new model, we can also consider right-angled triangular indentations, a groove geometry very different from the standard rectangular shape.

It should be noted that the work presented in this chapter was begun during my masters project and continued during the beginning of my PhD [125]. In particular, during the masters thesis the theoretical formalism was developed and numerically solved with some preliminary results. After the submission of my masters thesis and at the beginning of my PhD this work was continued, reformulating the method in to the form presented here and gathering of the results which form the bulk of this chapter.

5.2 Spoof SPPs

To date, the theoretical investigations into spoof SPPs have been mainly focused on two areas, the effective medium method and the Coupled mode method (CMM). Both methods rely on first splitting the geometry into separate regions and then solving the Helmholtz equation in each region independently (as outlined in section 2.2). The basic difference between the two methods lies in the description of the surface corrugations. In the effective medium method the layer with the surface corrugations is replaced by a planar slab with refractive index n_{eff}, whereas in CMM the corrugation is retained and the fields are expanded as infinite sums over the (i) eigenmodes of the corrugation inside the groove and (ii) periodic Bloch modes above the grooves, see figures 5.1 (a) and (b). In the limit that the expanded fields within CMM are truncated at 0^{th} order it recovers the

same result for the spoof SPP modes as the effective medium method.

CMM falls into the broader category of modal expansion methods that include, amongst others, the rigorous coupled wave method [126], the transfer matrix [127] and scattering matrix [128] methods and the Fourier mode method [129]. These methods typically provide numerical solutions and have been used since the 1960's to analyse the transmission and reflection properties of gratings[130], and more recently plasmonic structures [15] and photonic crystals [131, 132] . An important difference of CMM is that the Bloch expansion of the fields is confined to the top layer and the fields within the grooves are expanded over local eigenmodes only. In other words, the fields within each corrugation are assumed to be independent of the other surface corrugations. It is this qualification, which separates the CMM method from the more general Bloch expansion where the fields within each layer are expanded in terms of Bloch waves. Then, by means of equation (2.6), the fields at each interface are matched, providing a process by which the fields can be transferred from one side of the interface to the other. This can be done sequentially for consecutive interfaces, allowing the fields to be calculated throughout the system and providing a direct way of calculating the transmission and reflection spectra.

Interestingly, Bloch expansion techniques can run into trouble when dealing with plasmonic systems, particularly when considering TM polarised light [133, 134]. This becomes a particular problem when there are large discontinuities in the dielectric function of the different regions and the truncation of the sum leads to spurious effects such as ringing or Gibbs phenomenon. It is possible to achieve better convergence with reformulated methods, e.g. the consideration of Laurent's rule [135, 136], but the accuracy of the reformulation depends on the particular structure under consideration, and therefore undermines the generality of the scattering matrix approach.

The version of CMM employed here has been used to previously study spoof SPP phenomena, see [14] and references therein, and considers the groove as a section of an infinite waveguide, expanding the fields as a sum over these waveguide modes. In contrast to the more general scattering matrix and Fourier mode approaches, CMM typically truncates the sum over eigenmodes inside the corrugations at 0^{th} order. This can be justified if only the 0^{th} order mode is the only propagating waveguide mode. The other, higher order, waveguide modes are evanescent within the corrugations and contribute very little towards the dispersion relation. It is this difference which makes CMM a powerful theoretical tool as the system of equations can be calculated analytically.

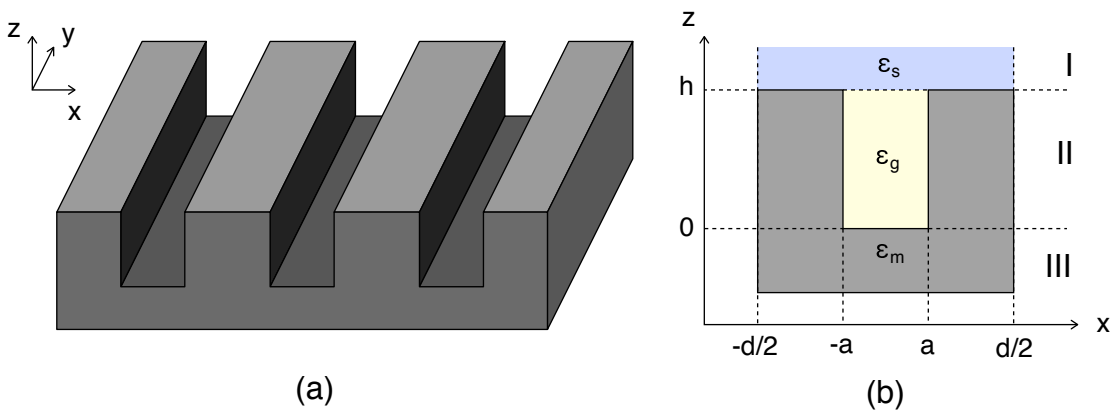

Figure 5.2: (a) 1D periodic corrugation of grooves. (b) Slice through the x-z plane labeling the important geometric and material quantities.

Finally, as with the effective index technique, in the subwavelength limit (where the wavelength is much greater than the period) CMM can provide an analytical dispersion relation. Whilst this relation is accurate only for a deep-subwavelength structure, it provides a solid qualitative basis for understanding the physics of the system and the effect of the geometric parameters on the wave characteristics.

5.2.1 Spoof SPPs in straight grooves

To demonstrate CMM and to illustrate the concept of spoof SPPs, we will look at one of the simplest structures that support spoof SPPs, the 1D array of rectangular grooves. The period of the corrugation is given by d and the height and width of the grooves by h and a respectively, as shown in figures 5.2 (a) and (b). The space is decomposed into three regions, I: $z \geq h$, II:$0 \leq z < h$ and III: $z < 0$. The dielectric constants of the system are ε_s in region I, ε_g inside the groove and $\varepsilon_m = -\infty$ inside the metal, treated as a perfect electric conductor (PEC).

In the region I the EM fields expanded in Bloch modes are given by

$$\begin{aligned} E_x^{\mathrm{I}} &= \sum_{n=-\infty}^{\infty} r_n \phi_n(x) e^{-g_n z}, \\ H_y^{\mathrm{I}} &= \sum_{n=-\infty}^{\infty} Y_n^{\mathrm{I}} r_n \phi_n(x) e^{-g_n z}, \end{aligned} \tag{5.1}$$

with the mode function $\phi_n = \exp[ik_n x]/\sqrt{d}$, the wavevectors along and perpendicular to the interface are $k_n = k_x + 2n\pi/d$ and $g_n = \sqrt{k_n^2 - \varepsilon_s k_0^2}$ respectively, the expansion coefficients r_n and the

admittance $Y_n^I = -i\omega\varepsilon_0\varepsilon_s/g_n$. In region II we expand the fields in terms of PEC waveguide modes. From the Helmholtz equation a solution of the wave equation can be derived as

$$E_x = (A\exp[iqx] + B\exp[-iqx])(C\exp[ipz] + D\exp[-ipz]), \tag{5.2}$$

where H_y and E_z are calculated using equation 2.3. Inside the groove the PEC condition means that the electrons within the metal react instantaneously to cancel any fields within the metal. This means that there are no electric fields inside the metal and also that the surface supports an infinite surface current. When considering the boundary conditions on the fields from equation 2.6 there are now no conditions on the parallel magnetic fields but all the parallel electric fields at the groove boundaries must be equal to zero, meaning that the general solution can be expressed as a sum over the eigenmodes

$$\begin{aligned} E_x^{\mathrm{II}} &= \sum_{m=0}^{\infty} C_m\chi_m(x)\sin(p_m z), \\ H_y^{\mathrm{II}} &= \sum_{m=0}^{\infty} Y_m^{\mathrm{II}} C_m\chi_m(x)\cos(p_m z), \end{aligned} \tag{5.3}$$

with $p_m = \sqrt{\varepsilon_g k_0^2 - q_m^2}$, the expansion coefficients C_m and the admittance $Y_m^{II} = -i\omega\varepsilon_0\varepsilon_g/p_m$. The mode function is $\chi_m = \Theta(a/2 - |x|)\sqrt{(2-\delta_{m0})/a}\cos(q_m(x + a/2))$ where δ_{ij} is the Kronecker delta and $\Theta(x)$ is the Heaviside function.

Matching the parallel electric and magnetic fields at the boundary between regions I and II yields two continuity equations, $E_x^{\mathrm{I}}(x,0) = E_x^{\mathrm{II}}(x,0)$ and $H_y^{\mathrm{I}}(x,0) = H_y^{\mathrm{II}}(x,0)$. The electric field continuity equation must hold across the whole interface from $-d/2 \leq x \leq d/2$ whereas the magnetic field continuity equation only needs to hold across the mouth of the groove, $-a/2 \leq x \leq a/2$. In order to remove the x-dependence of these equations, the Bloch modes ϕ_n and the waveguide modes χ_m are projected onto the two continuity equations which results in the following integrals;

$$\begin{aligned} \int_{-d/2}^{d/2} \phi_{n'}^*(x) E_x^{\mathrm{I}}(x,0)dx &= \int_{-d/2}^{d/2} \phi n'^*(x) E_x^{\mathrm{I}I}(x,0)dx, \\ \int_{-a/2}^{a/2} \chi_{m'}^*(x) H_y^{\mathrm{I}}(x,0)dx &= \int_{-a/2}^{a/2} \chi_{m'}^*(x) H_y^{\mathrm{II}}(x,0)dx, \end{aligned} \tag{5.4}$$

that can be combined into a set of linear algebraic equations

$$\sum_m (G_{mm'} - \epsilon_{mm'}) E_m = 0. \tag{5.5}$$

This is the master equation from CMM. The unknowns $E_m = C_m \sin(p_m h)$ can be interpreted as the amplitudes of the waveguide modes at the boundary between regions I and II. The term

$$G_{mm'} = \sum_n S^*_{nm'} S_{nm} Y^{\mathrm{I}}_n, \tag{5.6}$$

describes the indirect coupling of two different waveguide modes m and m' through the diffracted modes. A field within the groove with mode m couples its energy to all the diffracted modes n and this energy is then collected back into the mode m'. The function $S_{nm} = S^*_{nm} = \int_{-a/2}^{a/2} \phi^*_n \chi_m dx$ gives the overlap between the waveguide mode m and the diffracted mode n at the interface. Finally, the term

$$\epsilon_{mm'} = Y^{\mathrm{II}}_m \cot(p_m h) T_{mm'}, \tag{5.7}$$

describes the direct coupling of two different waveguide modes m and m'. For the case of straight rectangular indentations, $T_{mm'} = \int_{-a/2}^{a/2} \chi^*_{m'} \chi_m dx = \delta_{mm'}$. Hence, it is not possible for a mode m to excite a mode m'. In this case, equation (5.7) only describes the reflection of the waveguide mode m back onto itself at the interface.

Thus, solving the master equation for $k_x(k_0)$ yields the dispersion relation for spoof SPPs. It is also possible to derive an explicit analytic relation for the dispersion by taking the limit that the surface indentations are deep subwavelength, i.e. that $\lambda \gg a$. In this case the sum over the waveguide modes can be restricted to $m = 0$ only. The second, and more constricting, assumption is that the wavelengths under consideration are much longer than the period, $\lambda \gg d$, under which the sum over the diffracted modes can also be truncated to 0^{th} order. Employing these assumptions enables us to find the planar groove spoof SPP dispersion relation as

$$k_x = \sqrt{\varepsilon_s} k_0 \sqrt{1 + \frac{\varepsilon_s}{\varepsilon_g} \left(\frac{a}{d} \tan\left(\sqrt{\varepsilon_g} k_0 h \right) \right)^2}. \tag{5.8}$$

In the limit $k_x \to \infty$ we find the spoof SPP frequency, which occurs for $\sqrt{\varepsilon_g} k_0 h = \pi/2$. I.e. the

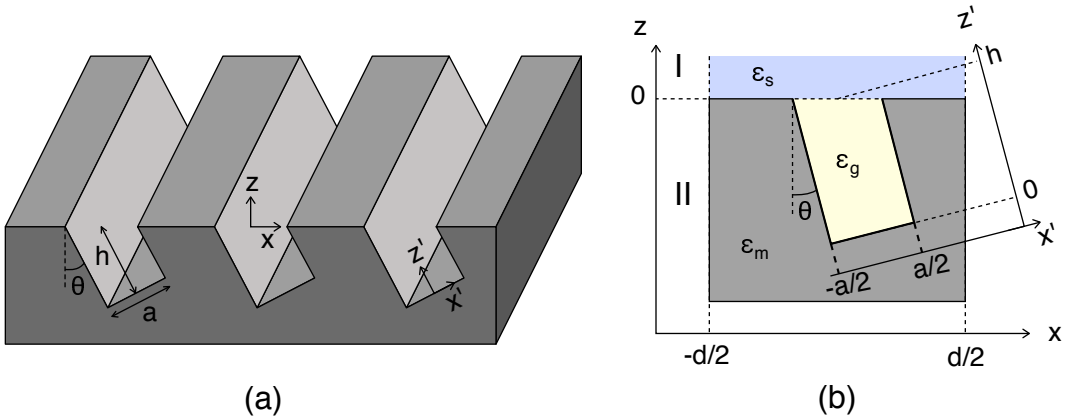

Figure 5.3: (a) 1D periodic corrugation of grooves indented at an angle θ. (b) Slice through the x-z plane labeling the important geometric and material. The primed co-ordinates (x', z') describe the groove geometry in region II and the unprimed co-ordinates (x, z) describe region I.

asymptotic frequency of the mode is controlled via the height of the groove, h, and occurs for $\lambda = 4h\sqrt{\varepsilon_g}$. The width of the groove, a, controls the speed at which the asymptote is approached.

5.3 Slanted grooves

Slanted gratings have been used within the photonics community, in particular for conventional waveguide coupling [137, 138, 139] and even for the excitation of surface plasmon polaritons [140]. However, the spoof plasmon characteristics of slanted gratings and, in particular, the effect of slant angle has yet to be investigated. To this end we again employ CMM and as before split the geometry into 2 regions, see figures 5.3 (a) and (b).

For the field expansion in region I, we use the unprimed co-ordinates (x, z), while, in region II, within the groove we use the primed co-ordinates (x', z'). Note that the origins of the two co-ordinate systems do not overlay one another. The transformation from the unprimed to the primed co-ordinates is given by

$$\begin{pmatrix} x' \\ y' \\ z' \end{pmatrix} = \mathbf{R} \begin{pmatrix} x \\ y \\ z \end{pmatrix} + \begin{pmatrix} 0 \\ 0 \\ h \end{pmatrix}, \tag{5.9}$$

where the rotation matrix **R** is given by

$$\mathbf{R} = \begin{pmatrix} \cos(\theta) & 0 & \sin(\theta) \\ 0 & 0 & 0 \\ -\sin(\theta) & 0 & \cos(\theta) \end{pmatrix}. \tag{5.10}$$

Here θ is the angle between the side wall of the groove and the surface normal (see figure 5.3). Importantly, the transformed Laplace operator, ∇^2, retains the same form for the unprimed and primed co-ordinates.

In region I the fields are expanded in the same Bloch modes that we used previously (see equation (5.1)). In region II the fields are the same as in the previous section except that they are now expressed using the primed co-ordinates:

$$\begin{aligned} E^{\mathrm{II}}_{x'} &= \sum_{m=0}^{\infty} C_m \chi_m(x') \sin(p_m z'), \\ H^{\mathrm{II}}_{y'} &= \sum_{m=0}^{\infty} Y^{\mathrm{II}}_m C_m \chi_m(x') \cos(p_m z'), \\ E^{\mathrm{II}}_{z'} &= \sum_{m=0}^{\infty} \eta_m Y^{\mathrm{II}}_m C_m \chi_m(x') \cos(p_m z') \tan(q_m(x' + a/2)), \end{aligned} \tag{5.11}$$

where $\eta_m = -iq_m/k_0$. At the interface between the fields, $z = 0$, and, thus, when we match the parallel electric and magnetic fields, we have in terms of the unprimed co-ordinates:

$$\begin{aligned} E^{\mathrm{I}}_x(x,0) &= \cos\theta E^{\mathrm{II}}_{x'}(\cos\theta x, h - \sin\theta x) - \sin\theta E^{\mathrm{II}}_{z'}(\cos\theta x, h - \sin\theta x), \\ H^{\mathrm{I}}_y(x,0) &= H^{\mathrm{II}}_{y'}(\cos\theta x, h - \sin\theta x), \end{aligned} \tag{5.12}$$

which now includes the z′-component of the electric field within the groove. After the projection of the Bloch and waveguide modes over the continuity equations we recover the master equation which is of the same form as before

$$\sum_m (G_{mm'} - \epsilon_{mm'}) E_{m'} = 0, \tag{5.13}$$

except that the important terms are now defined as

$$\begin{aligned} G_{mm'} &= \sum_n Y_n^{\mathrm{I}} S_{nm} [\cos\theta X_{nm'} - \sin\theta Z_{nm'}], \\ \epsilon_{mm'} &= \frac{Y_{m'}^{\mathrm{II}}}{\sin(p'_m h)} T_{mm'}, \end{aligned} \tag{5.14}$$

and the definition of E_m remains unchanged. Note that the exact definition of the overlap integrals S_{nm}, $X_{nm'}$, $Z_{nm'}$ and $T_{mm'}$ are given in appendix C. Importantly, we see that the term $G_{mm'}$, which governs the coupling the between different waveguide modes and grooves, now includes contributions from both the x' and z' fields in the groove. The contribution from each component is weighted by the slant angle θ. Interestingly, $T_{mm'}$ is no longer a Kronecker delta, since the eigenmodes $\chi_m(x')$ are not orthogonal when integrated along the x-axis, allowing the coupling of different modes within the groove. Importantly, in the limit that $\theta \to 0$ the terms collapse onto those of the straight groove recovering the standard results reported in section 5.2.1.

In the limit that a, $d \ll \lambda$ we can find an explicit analytical expression for the dispersion relation which is of the following form,

$$k_x = k_0 \sqrt{1 + \left(\frac{a}{d\,\mathrm{sinc}(k_0 a \tan\theta/2)} \right)^2 \tan(k_0 h)^2}. \tag{5.15}$$

From this equation we can get an intuitive picture of the effect of the angle θ on the dispersion relation. The asymptotic frequency of the mode is governed by the argument of the tangent function, which is independent of θ (and unchanged from equation (5.8)), and it is the dimension h which actually determines the spoof SPP behaviour. More precisely, it is not the depth of the indentation perpendicular to the PEC surface, but the optical length of the indentation that determines the spoof SPP frequency. This is an important result, as it suggests that it not the groove geometry itself that is important in defining the spoof SPP frequency, rather it is the optical length of the waveguide (which depends on the geometry).

Having said that, θ does change the factor in front of the tangent function. If we define the effective width of the groove, $a_{eff} = a\,\mathrm{sinc}^{-1}[(k_0 a/2)\tan\theta]$, such that it is brought into the same from as for straight indentations (see equation (5.15)), we can see that increasing the angle of the groove increases the effective width. This reflects the fact that the grooves are wider at the

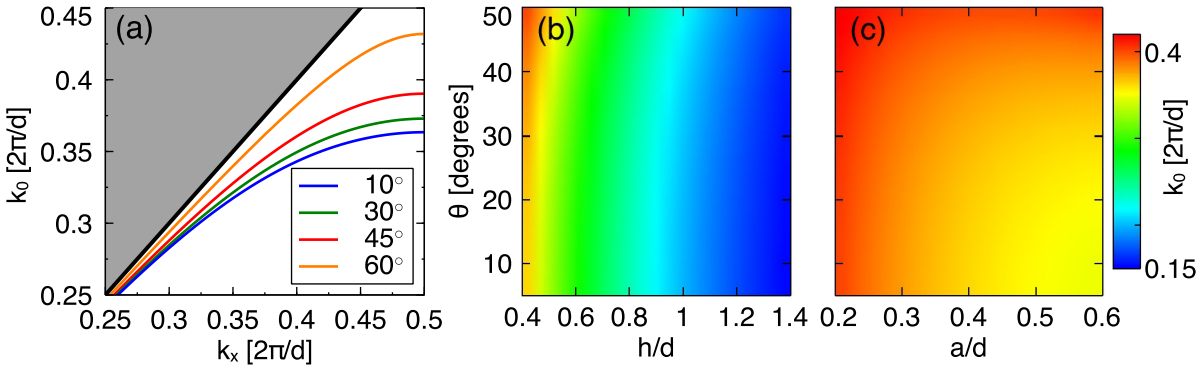

Figure 5.4: (a) The effect of groove angle on the dispersion relation of spoof SPPs with $a = 0.4d$ and $h = 0.4d$ for four different orientation angles. (b) Normalised spoof plasmon wavevector at the band edge ($k_x = \pi/d$) as a function of slant angle and groove height for $a = 0.4d$. (c) Same as before but as a function of groove width with $h = 0.4d$.

opening than at the bottom and that the spoof SPP characteristics are sensitive to the overall groove geometry. This sensitivity can also be seen in the overlap integrals with the appearance of terms of the form $h \pm a\tan\theta/2$, representing the lengths of the left and right hand sides of the grooves. Overall, we can see that despite the fact that the modal frequency $\omega(k_x \to \infty)$ is independent of the slant angle the curvature of the dispersion band is θ dependent.

In figure 5.4 (a) we can see how the dispersion relation is shifted with increasing slant angle, and that the frequency at the band edge is increased. This is anticipated from equation (5.15) where the increasing angle increases the speed at which the asymptote is approached. In figure 5.4 (b) and (c) we show that this effect is seen consistently over a whole range of geometries, irrespective the groove dimensions an increasing rotation of the groove with angle θ causes a blue shift of the spoof SPP resonance at the edge of the Brillouin zone. Interestingly, this effect is more pronounced for wider grooves. Taking the expansion of sinc(x) for small x we have that $a_{eff} \approx a(1 + \pi^2 a^2 \tan^2\theta/6\lambda^2)$[1] according to which the effective width increases with the square of $a\tan\theta/\lambda$, i.e. wider grooves are more sensitive to changes in θ than narrower grooves. Conversely, figures 5.4 (b) and (c) demonstrate that deeper grooves are less sensitive to changes of angle than shallower grooves. This can be intuitively understood from equation (5.15). For deep indentations, the term $\tan(k_0 h)$ dominates, but for shallower indentations the competition between the effective width and height effects causes the spoof SPPs to be more sensitive to changes in slant angle.

[1] Note that this expansion is valid for $(a/\lambda)^2 \ll 1$ (assuming that we do not approach extreme angles) which we have already assumed in the derivation of equation (5.15).

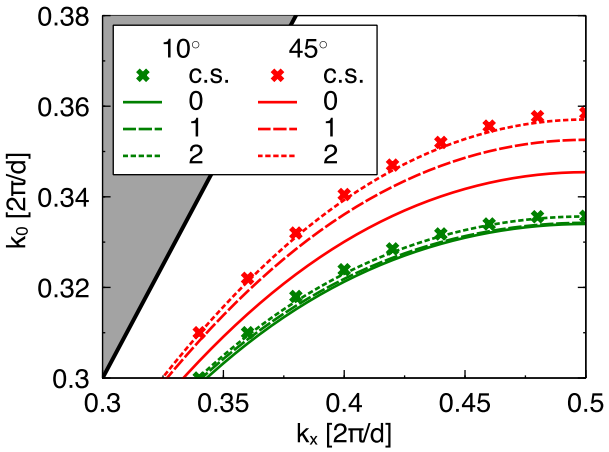

Figure 5.5: Convergence of the dispersion relation as the sum over waveguide modes is truncated at 0^{th} order (solid), 1^{st} order (dashed) and 2^{nd} order (dotted) lines for two different slant angles 10° (green line) and 45°. The crosses are the results from numerical simulations.

To check the validity of the analytical expressions, figure 5.5 compares the analytical results with the numerical FEM simulations for θ = 10° and θ = 45°. We calculated the analytical results by including up to the first 3 waveguide modes. For small angles we can see that the m = 0 approximation gives very good agreement to the numerical results, and only a very small adjustment is caused by the inclusion of higher order waveguide modes. However, for larger slant angles, more waveguide modes are required to achieve a good convergence to the numerical result. The validity of the m = 0 approximation arises as all the higher order waveguide modes are evanescent, and thus are vastly reduced in amplitude on their round trip up and down the groove, leading to a very small interaction with the other modes. However, when the grooves are highly slanted this approximation fails as it can no longer adequately describe the complex fields at the mouth of the groove, as evident from equations (5.14). Here the indirect interaction of waveguide modes (through $G_{mm'}$ via X_{nm} and Z_{nm}) is modified for large slant angles. The contribution of the $E_{z'}$ field becomes increasingly important at higher angles, and as this field component only arises for $m > 0$ it is not surprising that the higher order waveguide modes play an increasing role in the description of the mode. It also arises in the direct interaction of waveguide mode, $\epsilon_{mm'}$, which allows the cross-excitation of previously orthogonal (in the θ = 0 case) waveguide modes. Despite these limitations, we can see that using only the first 3 waveguide modes provides an excellent convergence to the numerical solution.

Figure 5.6 demonstrates the changes to the electric field profile at the edge of the FBZ for

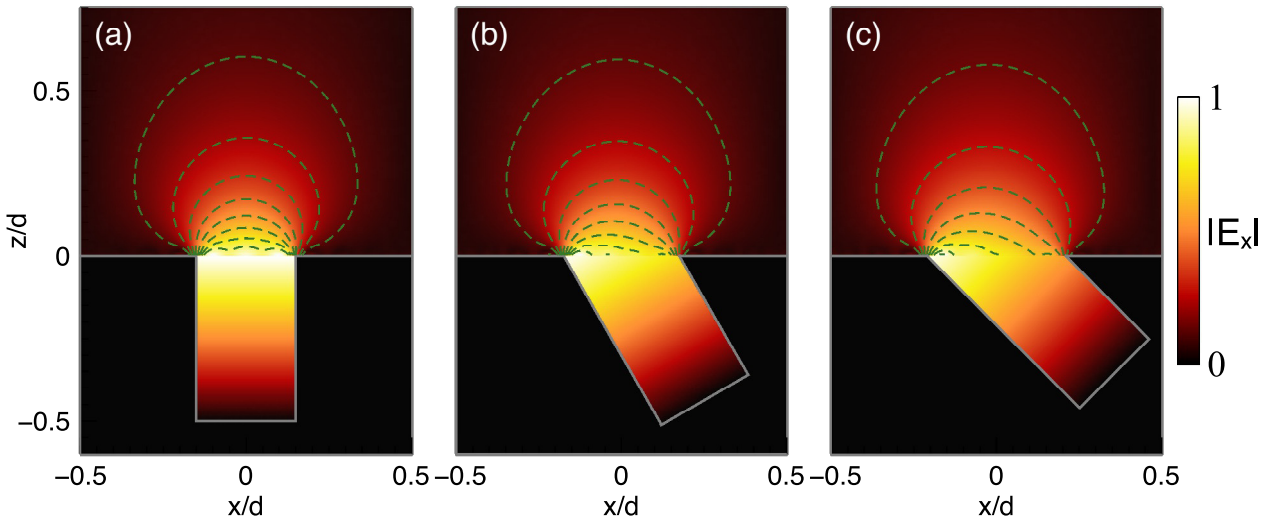

Figure 5.6: $|E_x|$ for a system of dimensions $a = 0.3d$, $h = 0.5d$ and (a) $\theta = 0°$, (b) $\theta = 30°$ and (c) $\theta = 45°$. Also plotted are the contour lines of constant field in the region I, above the grooves

different groove angles, with $a = 0.3d$ and $h = 0.5d$, calculated using $m_{max} = 0$. We can see from the contour lines that as θ is increased the field above the grooves becomes slightly asymmetric in the region close to the grooves, skewed towards one-side. It should be noted that as we increase the groove angle the frequency at the band edge blue-shifts and thus the fields at higher groove angles are evaluated at higher energies. Figure 5.6 also demonstrates some of the problems that can occur with these methods. Despite the fact that we have used $n_{max} = 10$ in the sum over Bloch modes, that shows a converged solution for the dispersion relation, there are still rippling effects due to the truncation of this sum that can be seen at the interface between regions I and II.

Furthermore, figure 5.6 also demonstrates the inadequacy of the $m = 0$ approximation at large θ. The field within the groove only undergoes a rotation as θ is increased, and the fields become increasingly mismatched at the interface between regions I and II, clearly indicating the failure of the approximation.

5.4 Triangular grooves and sawtooth surfaces

Finally, the model we have developed for slanted grooves can be applicable to one further limiting case. If the grooves are rotated such that the shortest side vanishes then it forms a triangular indentation into the metal. This is only possible if the opening of the groove between interfaces I

and II does not exceed the period of the array. Analysing such a system would allow us to consider the spoof SPP modes supported by right-angled triangular corrugations. The geometry of this system is substantially different to that of rectangular grooves and should provide us with further insights as to how differently shaped grooves affect the spoof SPP dispersion relation.

For our analysis it is convenient to define a new parameter $b = a\cos\theta$. The length of the shorter groove wall is given by $h - a\tan\theta/2$, so, in the limit that the shorter groove side vanishes we find

$$\theta = \arctan\left(\frac{2h}{a}\right). \tag{5.16}$$

From this we can see that $h = b\sin\theta/2$, and we are constrained to the case where $b < d$. The inset of figure 5.7 (a) demonstrates the geometries investigated and unsurprisingly shows that if we keep b fixed and alter θ the grooves modeled will trace out a semi-circle. From a quick analysis of equation 5.15 we see that using the effective medium approximation (where a, $d \ll \lambda$) the argument of the tangent function becomes $k_0 b\sin\theta/2$. Thus the spoof plasma wavelength is given by $\lambda = 2b\sin\theta$. Importantly, for our analysis, we see that λ gets larger (and thus k_0 smaller) for increasing θ, until $\theta = 90^\circ$. However, it is quite obvious that this cannot be true. The triangular grooves are symmetric in θ around $\theta = 45^\circ$, and as such the physics of a system with angle $45^\circ \pm \theta$ must be identical. One of the reasons for this error is the boundary condition we have used along the smaller groove wall, where the parallel electric fields are equal to zero. As the smaller groove wall no longer forms part of region II our expansion is erroneous, hence, we have to be very careful in our analysis. Therefore, in order to consider the model where it is most accurate we only use angles from $\theta = 0 - 50^\circ$, using $m_{max} = 2$, which provides a good convergence to numerical simulations (with the same accuracy as demonstrated in figure 5.5).

From figure 5.7 (a) we can see that increasing θ red-shifts the dispersion relation, as the groove depth perpendicular to the planar PEC interface increases with θ when groove width b remains fixed. In other words, the waveguide modes of the triangular groove penetrate a greater distance into the corrugated PEC surface and this leads to greater confinement. In figure 5.7 (b) we can see the spoof SPP mode frequency at the edge of the FBZ over all possible triangular grooves. Again, for all groves the normalised frequency is decreased as θ increase. Notably, despite the error in the method highlighted by the effective index approximation, the minimum modal frequency for a

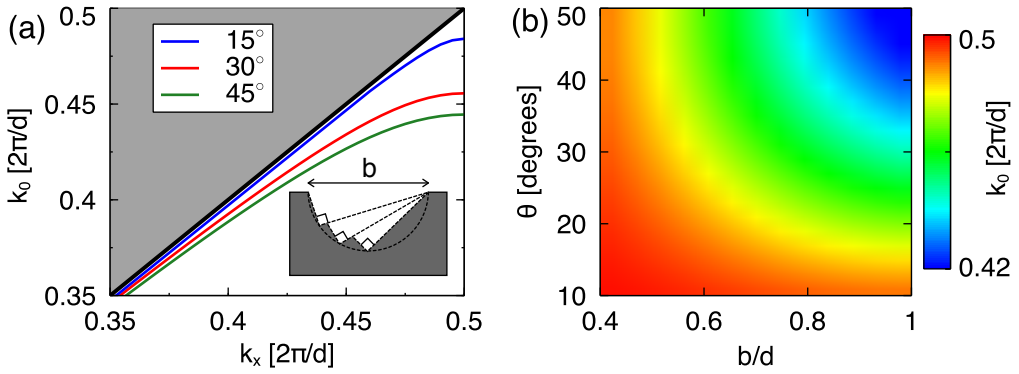

Figure 5.7: (a) Dispersion relation for triangular indentations with $b = 0.7d$ for angles of 15° (blue) 30° (red) and 45° (green). Inset: the schematic of the triangular shaped grooves. (b) Normalised spoof plasmon wavevector at the band edge ($k_x = \pi/d$) as a function of θ and b.

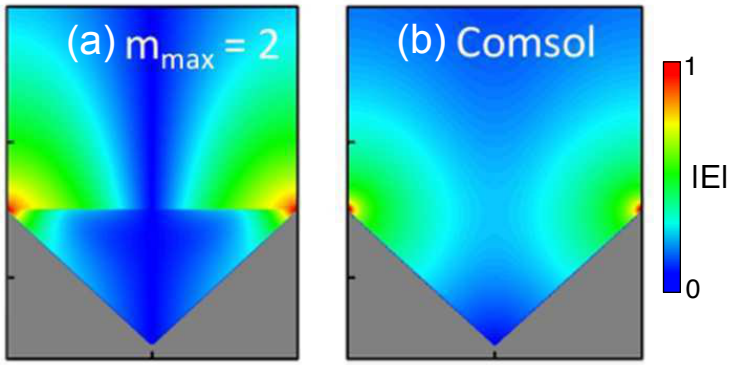

Figure 5.8: (a) Dispersion relation for triangular indentations with $b = 0.7d$ for angles of 15° (blue) 30° (red) and 45° (green). Inset: the schematic of the triangular shaped grooves. (b) Normalised spoof plasmon wavevector at the band edge ($k_x = \pi/d$) as a function of θ and b. Reprinted figure 4 with permission by Wood et al. [141]. Copyright 2012 American Physical Society.

fixed b is achieved at $\theta = 45°$ as it is at this point that the grooves have the greatest vertical depth away from the PEC surface.

Finally, by letting $b = d$ we end up with a completely triangular *sawtooth*-type surface, unlike those that are normally considered in connection with spoof SPPs. As we can see from figure 5.7(b), these are the spoof SPP modes that have the highest sensitivity to changes in the orientation angle, achieving the minimum λ/d, namely $\theta = 0.42$ at $\theta = 45°$. Figure 5.8 (a) shows the electric field profile at $k_x = \pi/d$, calculated with the first three waveguide modes and compared to the numerical simulated result (Figure 5.8 (b)) for $\theta = 45°$[2]. Interestingly, despite the fact that this

[2]In order the calculate the electric field profile we averaged the fields from the numerical results for $\theta = \pm 45°$. Note that due to the phase shift in the E_x fields they were averaged asymmetrically.

is an extreme case of our theoretical model, and the fact that only the first three waveguide modes were included, the analytical model was able to capture the majority of features in the electric field profiles, in particular, the strong field enhancements at the sharp points in the sawtooth surface. These sawtooth surfaces also show that spoof SPP modes can be supported in non-planar interfaces, raising the prospect that any periodic structure could support surface waves. Interestingly, these triangular indentations can be easier to fabricate, particularly on semi-conductor surfaces which can also display spoof SPP characteristics [142]. As such, the triangular groove geometry may be an attractive platform for spoof SPP applications.

5.5 Summary

In summary, we have attempted to consider the effect of the shape of the surface indentations on spoof SPPs. Firstly, by adapting the CMM, we were able to consider angled indentations. Notably, we found that, although the long wavelength limit (a, $d \ll \lambda$) gives no change in the spoof plasma frequency, the mode is significantly blue-shifted at the band-edge, an effect that accelerates with increasing θ. We showed that it is not the depth of the orientation that is important, only its optical length, in determining the spoof plasma frequency, and that the spoof SPP fields become asymmetric about the opening as the orientation angle is increased. Secondly, as a limiting case of our model, we were able to investigate right-angled triangular indentations, a completely different surface structure than those normally considered. These surfaces still maintain spoof SPP characteristics, with the surface waves being most confined for $\theta = 45^\circ$.

6 Spoof surface plasmon polaritons in real metals

6.1 Introduction

As the focus of the spoof plasmon community has been transferring the subwavelength confinement and highly localised EM fields of SPPs to lower frequencies naturally many of these works treat the metal as a PEC, a valid approximation at low frequencies. However, whilst metallic losses can be taken into account in numerical simulations and are intrinsically considered in experimental works, there have been very few theoretical works considering the effect of loss on spoof SPPs.

One approach to including the metallic losses is to treat the interface between the dielectric and metal using the surface impedance boundary condition (SIBC), whereby instead of the parallel electric fields going to zero at the surface of the metal (as in the PEC limit), there is a surface impedance condition [31] that requires

$$\mathbf{E}_{||} = Z_s \mathbf{n} \times \mathbf{H} \tag{6.1}$$

Taking the the surface normal **n** to be parallel to the z-axis this gives $E_x = -Z_s H_y$ and $E_y = Z_s H_x$ where Z_s is the surface impedance of the metal. The derivation and use of SIBCs is an interesting and rich topic in of itself [143], with many uses in numerical modeling of EM fields. However, this is beyond the scope of the work in this thesis, thus, we only state the result of the typical SIBC used within theoretical spoof SPP and EOT works, $Z_s = \sqrt{\mu_0/\varepsilon_0\varepsilon_m}^{-1}$ [26, 144, 145]. Within these works, the SIBCs are enforced at the horizontal interfaces between the metal and the dielectric, but not on the inner walls of the indentations, treating the waveguide fields inside the grooves as unchanged from the case of the PEC. Importantly, this neglects any change in the waveguide wavevector due to the penetration of the waveguide modes into the sidewalls which, as we shall see, can diverge

significantly from that of the wavevector derived under the PEC condition.

The other approach that has been applied is an effective medium method by Rusina et al. [27, 146]. In this method they consider the effects of the groove side walls by expressing the field within the groove using a metal-insulator-metal (MIM) waveguide mode. However, by using an effective medium approach their results are only valid when the wavelength of light is much greater than the groove period, i.e. $\lambda \gg d$. Furthermore, they fail to consider the effects of the metal at the bottom of the groove, considering it a PEC matching condition, and only use an approximate expression for the MIM wave-vector.

Therefore, there does not exist an accurate model of spoof SPPs that straddles both regimes, from perfectly conducting to lossy metals and from microwave to optical frequencies. Furthermore, the effect of the geometry on the spoof SPP mode (and on the spoof plasma frequency) is not fully understood for real metals. Finally, there has been little to no attention paid to the effects of the geometry on spoof plasmon losses. All in all, it is interesting that at low frequency regimes (THz and microwave,) where SPPs do not exist, we understand how to design surfaces to gives us an arbitrary plasma spoof frequency. Whereas, in high frequency regimes (I-R and optical), where SPPs exist, we do not have such knowledge. In this chapter we develop a theory of spoof SPPs valid from frequencies close to the plasma frequency and below. We use an extension the mode matching method outlined in chapter 5. From this we deduce an analytic dispersion relation that recovers both the SPP and spoof SPP in a PEC in the appropriate limits. We then consider the modal losses of spoof SPP modes and how these losses are interlinked to both the real part of the modal frequency and the geometry. Finally, we consider the effect of these lossy SPPs modes on the phenomenon of EOT in the optical and near I-R spectrum, and also the possibility of compensating the losses of spoof SPP modes.

6.2 Metal-insulator-metal waveguide modes

In order to utilise the CMM without sacrificing its useful features we need a different way of accounting for the real metal. One way to achieve this is to consider the effect of the metal dispersion on the guided modes within the grooves. Figure 6.1 (a) demonstrates the geometry of the slab MIM

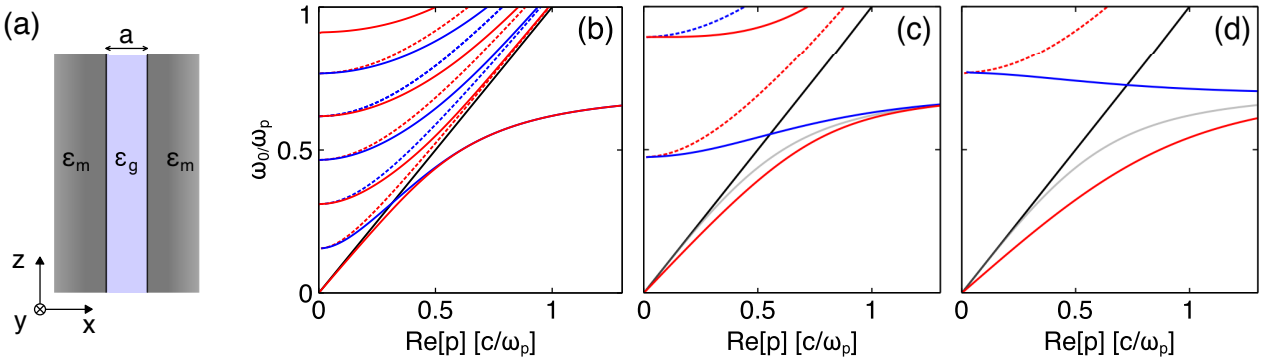

Figure 6.1: (a) Layout of the MIM waveguide. (b) Dispersion relations for a = 400nm, (c) a = 100nm and (d) a = 40nm. TM modes (solid lines), TE modes (dashed lines), odd modes (red) and even modes (blue) are shown, as are the light line within the groove (black line) and the SPP (grey line) for the metal dielectric interface.

waveguide. From section 2.5 we know that the TM modes in a slab waveguide obey the equation

$$\tan(qa/2) = \begin{cases} \frac{\alpha\varepsilon_d}{q\varepsilon_m} & \text{odd mode} \\ \frac{-q\varepsilon_m}{\alpha\varepsilon_d} & \text{even mode} \end{cases}, \tag{6.2}$$

where $q = \sqrt{\varepsilon_g k_0^2 - p^2}$ and $\alpha = \sqrt{p^2 - \varepsilon_m k_0^2}$ are the wavevectors of the modes parallel to the x-axis in the groove and metal regions, a is the width of the groove and p is the wavevector of the MIM mode [1].

Figure 6.1 (a) shows the layout of a MIM waveguide, whilst figure 6.1 (b), (c) and (d) show the modes of the MIM waveguide consisting of gold and air for three different thicknesses; 400, 100nm and 40nm respectively. Both the TM (solid) and TE (dashed) modes are plotted for both the odd (red) and even (blue) solutions, whilst the light line in the medium (black) and the SPP for a single interface (grey) are also plotted. The lowest odd TM mode is the only mode that displays no lower frequency cut-off, i.e. it is the only mode with a real wavevector p for lower frequencies. Only the lowest order odd and even TM modes are plasmon-like modes, also known as the "gap-plasmon" modes, corresponding to the two modes predicted for negative cladding by Prade et al. [147]. These modes tend towards the SPP mode at large wavevectors for all gap sizes. For all groove widths the TE modes only appear at higher frequencies than there TM counterparts. If we now consider that for PEC boundary conditions $p = \sqrt{\varepsilon_g k_0^2 - (m\pi/a)^2}$ where m = 0, 1, ..., we see that

[1] Note that often in textbooks p is denoted as β

the lowest order mode follows the medium light line $\sqrt{\varepsilon_g}k_0$. As such, for small groove widths where the MIM TM odd mode diverges significantly from the light line there is expected to be a large difference between the MIM waveguide mode and the PEC waveguide mode.

Using equation (2.12), the fields of the MIM TM waveguide modes can be re-written in terms of the modal function χ_m as

$$\chi_m = \frac{1}{2\sqrt{a}}\left(e^{iq_m x} + (-1)^m e^{-iq_m x}\right) \tag{6.3}$$

within the groove ($-a/2 \leq x \leq a/2$). We also need to define the mode outside the the groove as

$$\chi_m^+ = \chi_m(a/2)e^{-i\alpha_m(x-a/2)} \quad \text{for } x > a/2 \tag{6.4}$$

and

$$\chi_m^- = \chi_m(-a/2)e^{i\alpha_m(x+a/2)} \quad \text{for } x < -a/2, \tag{6.5}$$

where the index m runs from $m = 0, 1, \ldots, \infty$. Assuming that the modes within a single groove can be considered isolated from the modes within adjacent grooves then we can use the MIM modes to expand the fields within each groove within CMM. This assumption is valid as long as the distances between adjacent grooves does not approach the skin depth of the metal and will be analysed further in section 6.3.3.

6.3 1D array of grooves

The 1D array of grooves geometry is shown again in figure 6.2. We first split the geometry into three regions, I ($z > h$), II ($0 < z < h$) and III ($z < 0$). As before, in region I the fields are constructed in terms of diffraction modes

$$\begin{aligned} H_y^{\mathrm{I}} &= \sum_{n=-\infty}^{\infty} r_n \phi_n(x) e^{-g_n z}, \\ E_x^{\mathrm{I}} &= \sum_{n=-\infty}^{\infty} Z_n r_n \phi_n(x) e^{-g_n z}, \end{aligned} \tag{6.6}$$

where $\phi_n(x) = \exp(ik_n x)/\sqrt{d}$, $k_n = k_x + 2n\pi/d$, $g_n^2 + \varepsilon_s k_0^2 = k_x^2$ and the impedance $Z_n = ig_n/\omega\varepsilon_0\varepsilon_s$. In region II, the fields are constructed in terms of the MIM waveguide modes. Within the groove($-a/2 <$

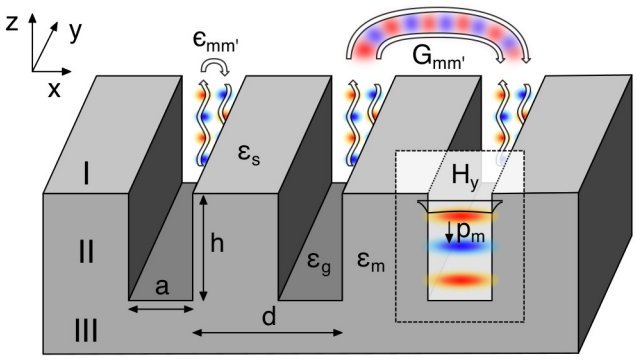

Figure 6.2: The 1D array of grooves, showing the relevant geometric parameters and the region I, II and III. The permittivities above and inside the grooves are given by ε_s and ε_g. Also shown is the magnetic field profile H_y of the lowest order TM waveguide mode p_m. Finally, the terms of the master equation $\varepsilon_{mm'}$ and $G_{mm'}$ are shown.

$x < a/2$), the fields can be expressed as:

$$H_y^{\mathrm{II}} = \sum_{m=0}^{\infty} \chi_m(x)(A_m e^{ipmz} + B_m e^{-ip_m z}), \tag{6.7}$$

where $p_m^2 + q_m^2 = \varepsilon_g k_0^2$. In region III, the fields are decaying into the surface of the metal (in the negative z-direction), whilst they still feel the effect of the MIM geometry in region II. As such, the modes are propagate along the interface in both regions (II and III) with the same wavevector, but decaying into the surface of the metal with a different wavevector. Hence, the fields in region III, (for $-a/2 \leq x \leq a/2$), are

$$H_y^{\mathrm{III}} = \sum_{m=0}^{\infty} \chi_m(x) C_m e^{\beta_m z}, \tag{6.8}$$

where $\beta_m = \sqrt{\varepsilon_m k_0^2 - p_m^2}$. In the above equations the symbols A_m, B_m, C_m and r_n all represent unknown expansion coefficients. Matching the fields at the interface between regions II and III, at $z = 0$, enables the expansion coefficients B_m to be written in terms of A_m as

$$B_m = A_m \frac{p_m \varepsilon_m + i\beta_m \varepsilon_g}{p_m \varepsilon_m - i\beta_m \varepsilon_g} \tag{6.9}$$

Therefore, we define the new parameter ν_m as

$$\nu_m = \frac{1}{2ih} \ln\left(\frac{p_m \varepsilon_m + i\beta_m \varepsilon_g}{p_m \varepsilon_m - i\beta_m \varepsilon_g}\right), \tag{6.10}$$

such that $B_m = A_m \exp(2i\nu_m h)$. This parameter, ν_m, is one of the major differences in the theoretical description when considering real metals. Considering the fact that in real metals the fields are expected to decay into the surface of the metal then we can intuitively anticipate that the height of the groove that is experienced by the light will be increased compared to a PEC boundary. Thus, the cavity mode created by the MIM waveguide can be expected to appear at longer wavelengths. This new parameter ν_m can be seen as the effective decrease of the wave-vector inside the groove, due to the fact that we are now dealing with a real metal instead of a PEC, or on the other hand, an effective increase in the height of the groove.

Using this, the fields in region II are

$$H_y^{\text{II}} = \sum_{m=0}^{\infty} A_m \cos(p_m z - \nu_m h) \begin{cases} \chi_m^+(x) & \text{for } x > a/2 \\ \chi_m(x) & \text{for } -a/2 < x < a/2 \\ \chi_m^-(x) & \text{for } x < -a/2 \end{cases}, \tag{6.11}$$

and

$$E_x^{\text{II}} = \sum_{m=0}^{\infty} A_m Z_m \sin(p_m z - \nu_m h) \begin{cases} \chi_m^+(x)\varepsilon_g/\varepsilon_m & \text{for } x > a/2 \\ \chi_m(x) & \text{for } -a/2 < x < a/2 \\ \chi_m^-(x)\varepsilon_g/\varepsilon_m & \text{for } x < -a/2 \end{cases}, \tag{6.12}$$

where $Z_m = ip_m/\omega\varepsilon_g\varepsilon_0$. Rewriting the fields in this way is a more compact form and expresses the effects of the real metal on the fields within region II, including both the MIM modes and the effect lower end of the waveguide. To proceed the fields are matched between the top two regions at $z = h$. In contrast to the PEC case, as we now have magnetic and electric fields defined across the whole unit cell both continuity equations will need to hold for $-d/a \leq x \leq d/2$. This results in the familiar master equation:

$$\sum_m E_m(G_{mm'} - \epsilon_{mm'}) = 0 \tag{6.13}$$

As in the PEC case the unknown amplitudes E_m are the amplitudes of the waveguide modes the interface between regions I and II. $G_{mm'}$ is the indirect coupling of the waveguide modes via the diffraction modes and $\epsilon_{mm'}$ is the direct coupling of the waveguide modes. They are shown

schematically in figure 6.2 and defined as

$$E_m = A_m Z_m \sin((p_m - \nu_m)h), \tag{6.14}$$

$$G_{mm'} = \sum_n \frac{1}{Z_n} S^E_{nm} S^H_{nm'}, \tag{6.15}$$

$$\epsilon_{mm'} = \frac{1}{Z_m} \cot((p_m - \nu_m)h)\, T_{mm'}, \tag{6.16}$$

where the overlap integrals are given as

$$\begin{aligned} S^E_{nm} = {} & \frac{\varepsilon_g}{\varepsilon_m} \int_{-d/2}^{-a/2} (\phi_n)^* \chi^-_m \, dx + \int_{-a/2}^{a/2} (\phi_n)^* \chi_m \, dx \\ & + \frac{\varepsilon_g}{\varepsilon_m} \int_{a/2}^{d/2} (\phi_n)^* \chi^+_m \, dx \end{aligned}, \tag{6.17}$$

$$\begin{aligned} S^H_{nm'} = {} & \int_{-d/2}^{-a/2} \phi_n (\chi^-_{m'})^* \, dx + \int_{-a/2}^{a/2} \phi_n (\chi_{m'})^* \, dx \\ & + \int_{a/2}^{d/2} \phi_n (\chi^+_{m'})^* \, dx \end{aligned}, \tag{6.18}$$

$$\begin{aligned} T_{mm'} = {} & \int_{-d/2}^{-a/2} \chi^-_m (\chi^-_{m'})^* \, dx + \int_{-a/2}^{a/2} \chi_m (\chi_{m'})^* \, dx \\ & + \int_{a/2}^{d/2} \chi^+_m (\chi^+_{m'})^* \, dx \end{aligned}, \tag{6.19}$$

and the evaluated expressions are given in appendix C.

6.3.1 Explicit dispersion relation

To produce an explicit dispersion relation we can assume that both the width of the slits and the period of the array are subwavelength ($a, d \ll \lambda$) allowing us to restrict our analysis to the lowest order waveguide ($m = 0$) and diffraction modes ($n = 0$) only. Furthermore, we assume that the relevant fields are concentrated inside the groove, and we drop the overlap integrals involving χ^+_m and χ^-_m from our equations. Under these assumptions we find that:

$$k_x = \sqrt{\varepsilon_s} k_0 \sqrt{1 + \frac{\varepsilon_s}{\varepsilon_g} \left(\frac{p_0}{\sqrt{\varepsilon_g} k_0} \frac{a}{d} \tan((p_0 - \nu_0)h) \right)^2}. \tag{6.20}$$

By defining the effective parameters a_{eff} and h_{eff} we can transform this into the PEC form of the equation,

$$k_x = \sqrt{\varepsilon_s}k_0\sqrt{1+\frac{\varepsilon_s}{\varepsilon_g}\left(\frac{a_{eff}}{d}\tan(\sqrt{\varepsilon_2}k_0h_{eff})\right)^2}, \tag{6.21}$$

where

$$a_{eff} = \frac{p_0}{\sqrt{\varepsilon_g}k_0}a, \tag{6.22}$$

$$h_{eff} = \frac{p_0}{\sqrt{\varepsilon_g}k_0}(1-\frac{\nu_0}{p_0})h, \tag{6.23}$$

and thus we can examine the effects of the real metal on the spoof SPP dispersion. Recall, also, that the z-component of the lowest order waveguide mode with PEC boundary conditions is $\sqrt{\varepsilon_g}k_0$. Thus, the effective width is altered by the ratio of the waveguide mode vectors for the real metal and PEC cases. As p_0 has no lower frequency cut-off and only appears below the medium light line we know that $p_0 \geq \varepsilon_g k_0$. In other words, the effect of the real metal is to make the effective width of the grooves larger.

When considering the effective height, it is increased by the same ratio that affected the effective width. Importantly, it is h_{eff} that ultimately determines the spoof plasma frequency that the mode tends towards at large wavevectors. As such the increase in the effective height is likely to have a much larger effect on the mode than the increase in effective width. The second factor that increases the effective height is the ratio of ν_0/p_0, but it should be noted that in general the factor of $(1-\nu_0/p_0) > 1$ and it causes an increase in the effective height. In figure 6.3 we can see the change in this ratio for (a) $h = a$ and (b) $h = 3a$ as the wavelength of the light and the width of the grooves is altered. Depending on the ratio of the groove height to width the effect of the real metal at the bottom of the groove can have a small or large effect. For tall grooves, when h is much larger than a, the effect of ν_0 is decreased and the relative increase in the height is small. For small grooves, when h is similar to a, this effect is increased. For all groove heights, as the frequency of light gets closer to the plasma frequency of the metal, the effect of ν_0/p_0 on the effective height is increased as the mode decays further into the metal surface. For instance, for a groove width of 50nm and a groove height of 150nm, at a wavelength of 1μm the effect of the real metal groove bottom is between a 5 and 10% increase in the effective height.

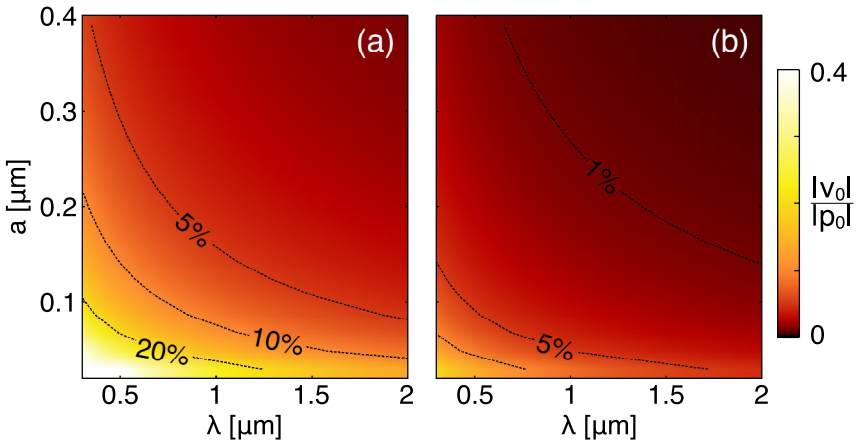

Figure 6.3: Change in the ratio ν_0/p_0 for $h = a$ (a) and $h = 3a$ (b) as both the groove width a and the wavelength of the mode λ are altered.

Overall, real metals cause both the effective width and height of the grooves to increase compared with the PEC case. These two effects both cause the dispersion relation to red-shift towards lower frequencies.

Before we proceed onto an analysis of the numerical dispersion relation and the effects of the real metal we can check our model by confirming it achieves the appropriate behaviour in limiting cases. First we consider whether equation (6.20) reproduces the spoof SPP dispersion relation for PEC boundary conditions if $\varepsilon_m \to \infty$. From a quick look at equation (6.10), and recalling that the parameter β_m is dependent on $\sqrt{\varepsilon_m}$, we see that the left hand terms in the numerator and denominator within the logarithm depend on ε_m whereas those on the right depend on $\sqrt{\varepsilon_m}$. As such the argument of the logarithm tends to 1 and $\nu_m \to 0$. Now when looking at equation (6.2), and noting that α_m is also dependent on $\sqrt{\varepsilon_m}$ then the mode equation becomes

$$\tan(q_m a) = \begin{cases} 0 & \text{odd modes} \\ \infty & \text{even modes} \end{cases} . \tag{6.24}$$

Thus, in the case of odd modes we have that $q = 2m\pi/a$ and in the case of even modes we have $q = (2m+1)\pi/a$. Combining them we find that $q = m\pi/a$. These are the modes used within the expansion for the PEC case, and taking only the mode $m = 0$ we recover the wavevector of the lowest order mode $p_0 = \varepsilon_g k_0$. By inserting this directly into equation (6.20) it is obvious that it exactly reproduces the spoof SPP dispersion relation.

Secondly, in the case where the area of the grooves $\to 0$ then equation (6.20) should recover the SPP mode for a single metal dielectric interface. Let us take the limit such that $a, d, h \to 0$. In terms of a and d, they only appear in ratio within equation (6.20), thus in this limit the ratio $a/d \to 1$. Taking $h \to 0$ the only term that remains in the argument of the tangent function becomes $-\nu_0 h$. Inserting equation (6.10) we find that $\tan(-\nu h) = -\beta_0 \varepsilon_g / p_0 \varepsilon_m$, and thus

$$k_x = \sqrt{\varepsilon_s} k_0 \sqrt{1 + \frac{\varepsilon_s \beta_0^2}{k_0^2 \varepsilon_m^2}}. \tag{6.25}$$

$\beta_0(k_0, q) = \sqrt{q^2 - \varepsilon_m k_0^2}$ is a function of both the free space wavevector and the x-direction wavevector in the groove. However, since the groove has vanished we can use the continuity of the magnetic fields to calculate $q(k_x)$. The continuity of the fields at $z = 0$ requires that

$$r_0 e^{ik_x x} = (A_0 e^{iq_0 x} + B_0 e^{-iq_0 x}). \tag{6.26}$$

This must hold along the boundary from $-\infty < x < \infty$. Thus, multiplying by $e^{-ik'_x x}$ and integrating yields

$$r_0 \delta(k_x - k'_x) = A_0 \delta(q_0 - k'_x) + B_0 \delta(q_0 + k'_x). \tag{6.27}$$

Thus, there is only a non-arbitrary solution when $q_0 = \pm k_x$. As such, we can rewrite the function $\beta^2 = k_x^2 - \varepsilon_m k_0^2$. From here the spoof SPP dispersion relation can be rearranged to find

$$k_x = k_0 \sqrt{\varepsilon_m \varepsilon_s / (\varepsilon_m + \varepsilon_s)}. \tag{6.28}$$

Hence, in the limit that the groove area approaches zero the spoof SPP dispersion of equation (6.20) relation recovers exactly the SPP dispersion relation.

Finally, it should also be mentioned that whilst equation 6.20 is useful for a qualitative understanding of the system behaviour the assumptions under which it is valid are very limiting and thus it should not be used to provide quantitative results or the system. In what follows we analyse the model using a general Drude-like response with ω_p = 9eV and γ = 0.05eV which are typical for plasmonic materials.

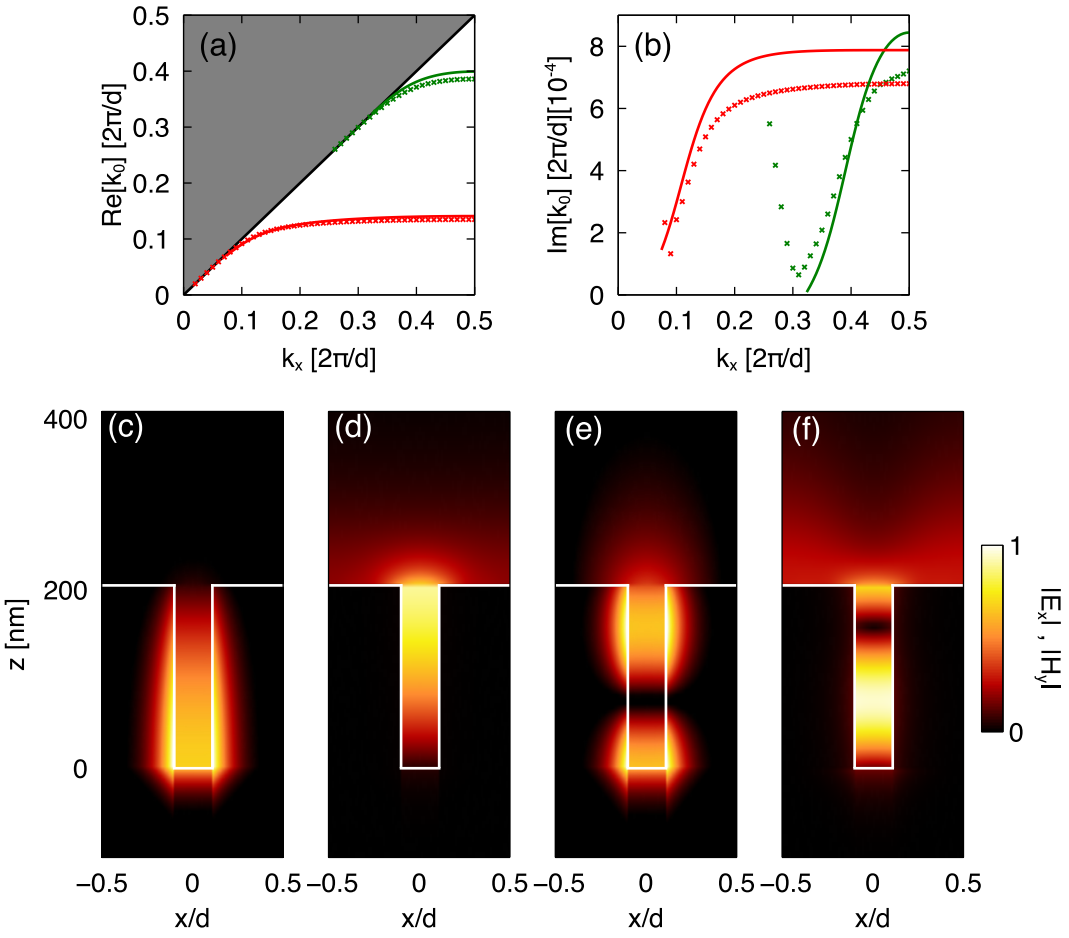

Figure 6.4: The real (a) and imaginary (b) parts of the dispersion relation for grooves of geometry d = 200nm, $a = 0.2d$ and $h = d$ comparing the theory (solid lines) with numerical simulations (crosses). (c) $|\mathbf{H}|$ and (d) $|\mathbf{E}|$ field profiles of the lower SPP band (red line) at the band edge. (e) $|\mathbf{H}|$ and (f) $|\mathbf{E}|$ field profiles of the upper SPP band (green line) at the band edge. All the fields are normalised such that the minimum and maximum amplitudes are at 0 and 1.

6.3.2 Results

Figures 6.4 (a) and (b) demonstrates the spoof SPP dispersion relations produced from equation (6.13) for d = 200nm, $a = 0.2d$ and $h = d$. The sums were truncated with $n_{max} = 10$ and $m_{max} = 0$, the number of modes needed to achieve convergence. Unless otherwise stated, all results in this section will use the same n_{max} and m_{max}. From the real part of the dispersion relation (figure 6.4 (a)) we can see the comparison of theoretical (solid lines) and numerical results (crosses) for the two spoof SPP modes present within the spectrum (at wavelengths of 1440nm (red line) and 501nm (green line)). There is a good agreement between the results, with small discrepancies arising in

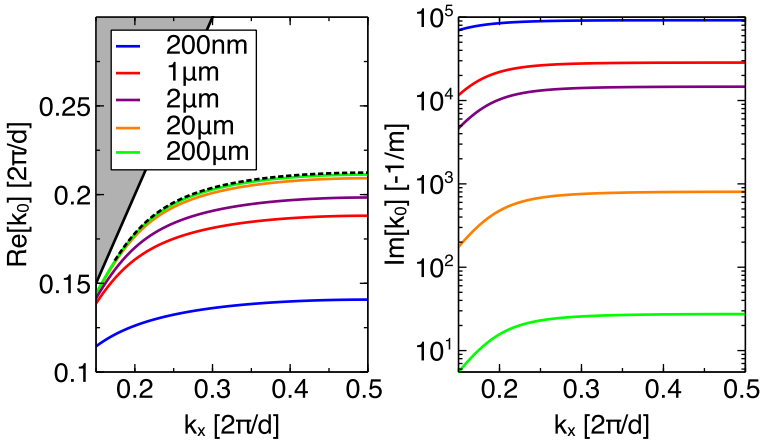

Figure 6.5: The change in the (a) real part of the dispersion relation and (b) the modal losses, with $a = 0.2d$ and $h = d$, as d is changed from 200µm to 200nm. Also plotted is the PEC dispersion relation (dashed line) and the light line (solid black line).

the upper mode. Figure 6.4 (b) demonstrates the modal losses (calculated using FDTD) in the two modes and interestingly the theoretical model appears to overestimate the losses of the modes by roughly $10 - 15\%$. This mismatch is consistent over the comparisons we have made with other geometries too. However, despite this mismatch, it still captures well the qualitative behaviour of the losses as the spoof SPP moves away from the light line and flattens. Interestingly, the modal losses are constant over the flattened SPP band.

The lower panels of figure 6.4 (c-f) show the magnitudes electric and magnetic fields, $|\mathbf{E}|$ and $|\mathbf{H}|$ of the two modes evaluated at $k_x = \pi/d$. The magnetic fields for the lower, (c), and upper, (e), modes demonstrate the penetration of the fields inside the sidewalls and groove bottom. In contrast, the penetration of the electric fields into the metal surfaces is very small, with the majority of the fields still residing in the slits. These field profiles also demonstrate that there are small field mismatches present in the magnetic field profiles, along the sidewalls for $z < 0$ and $|x| > a/2$ in (c) and (e). The mismatch along the sidewalls is an indication that the theory is not exact at this point, as demonstrated by the small discrepancy between simulations and fields in the green lines and crosses. The mismatches at the lower corners of the magnetic field profiles are actually an error in the model that is considered in more detail in section 6.3.3.

One important consequence of using the PEC boundary condition is that the resulting dispersion relations are dependent only on the geometric parameters and the spoof plasma frequency is scalable to all frequency regimes. Thus, to see the effect of a real metal on the spoof SPP

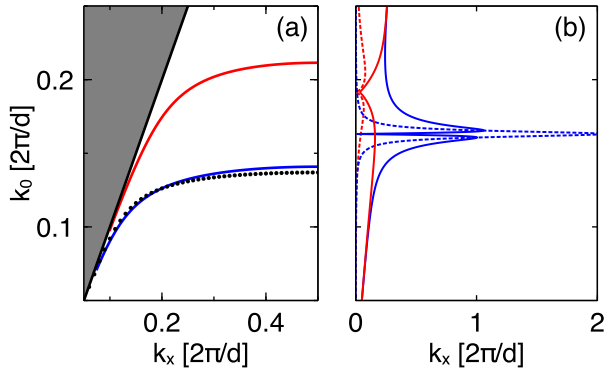

Figure 6.6: Comparison of the derived spoof SPP dispersion relation (blue lines) for a groove geometry of d = 200nm $a = 0.4d$ and $h = d$ with the (a) SIBC approach (red line) [26] including numerical simulations (black circles) and with the(b) effective medium MIM approach (red lines) [146], where both the real k_x (solid) and imaginary k_x (dotted) lines are shown.

dispersion relation we can keep the ratio of the of h/d and a/d constant and change d over several orders of magnitude. Figure 6.5 (a) shows how the dispersion relation changes for $a = 0.2d$, $h = d$ and d ranging from 200μm to 200nm. As the period d is decreased the modal frequency at the edge of the first Brillouin zone shifts away from $k_0 = 2\pi/d = 0.23$, the frequency of the PEC spoof plasmon, to lower values. This is consistent with our analysis within effective medium approximation whereby the effective width and height increase due to the real metal leading to a red shift of the mode. The shift becomes increasingly significant as we get to smaller and smaller periods, i.e. the modal frequency becomes closer to the plasma frequency of the metal. This is as to be expected as when we are closer to the plasma frequency, and as the width of the groove becomes smaller, the MIM wavevector diverges further from the light line increasing the red-shift of the mode. Note that for $d > 200\mu$m the dispersion is indistinguishable from the PEC case.

In figure 6.5 (b) we can see how the modal losses rise as the metal dispersion becomes increasingly important. For large d where the modal frequency is far from ω_p and the metal behaves similarly to a perfect conductor the losses remain low, but as d decreases the losses increase drastically in magnitude, as both the modal frequency is increasing and the width of the groove is narrowing, meaning that the MIM waveguide modes become more lossy (the loss for the PEC metal case is zero).

We can compare our analytical model to the previous attempts to incorporate the metal dispersion into the description of spoof SPPs, as shown in figures 6.6 (a) (where we compare to the

SIBC approach of Garcia-Vidal et al. [26]) and (b) (where we compare to the MIM mode approach of Rusina et al. [146]). We do this for d = 200nm, $a = 0.4d$ and $h = d$. Taking first the comparison to the SIBC approach (figure 6.6 (a)) we can see that our model (blue line) is a much better approximation to the numerical simulations (circles) than the SIBC approach (red line). From this we can see the importance of using the MIM wavevector within the groove, without which the optical length of the groove cavity mode is grossly underestimated at IR and optical wavelengths.

Secondly, we can compare against the propagation vector from the dispersion relation derived by Rusina et al. [146], where the effective medium approach is used to consider the propagation losses of a spoof SPP wave. Thus, in figure 6.6 (b) we compare equation (6.20) to equation (7) from [146] [2]. Comparing the equations we note that the only differences arise from the term ν_0 and from the low frequency approximation that Rusina and co-workers make for the MIM mode wavevector. In the low frequency limit our theory exactly reproduces the results shown in paper [146]. For d = 200nm, $a = 0.4d$ and $h = d$, both models show the mode back-bending, causing the mode to no longer reach the slow light point, and the losses becoming dominant. Notably, as the approximation applied by Rusina over-estimates the loss of the MIM mode in the optical regime (particularly for narrow grooves) it shows a mode that is completely washed out and shows no spoof plasmon like behaviour, whereas, the including the full MIM wavevector enables the mode to retain the spoof SPP characteristics, including the backbending of the mode which occurs once the propagation losses become greater than the wavevector ($\mathrm{Im}[k_x] > \mathrm{Re}[k_x]$). This displays the same type of behaviour as normal SPPs for complex propagation wavevectors [32].

Until now, as the modal losses of the spoof SPP have not been considered properly it has not been considered how these losses will vary with specific groove geometry. Firstly let us consider how the dispersion bands alter with changing height h. It is well established that the asymptotic frequency of the dispersion band is governed by the argument of the tangent function in equation (6.20) as the limit where $k_x \to \infty$ occurs for the argument of the tangent $\to \pi/2$. Thus in the PEC limit we have that $k_0 = \pi/2h$ whereas, for the MIM modes we have that $p_0 - \nu_0 = \pi/2h$. Therefore, we expect the asymptotic mode behaviour to have the same characteristics, red-shifting the modal frequency for an increase in h. Figure 6.7 (a) shows how the real part of the dispersion relation

[2] We cannot compare a full Bloch mode approach as Rusina and co-workers have solved for the wavevector k_x as a function of real k_0, i.e. a complex wavevector. For the full Bloch expansion k_x must be real, otherwise the Bloch theorem is not satisfied.

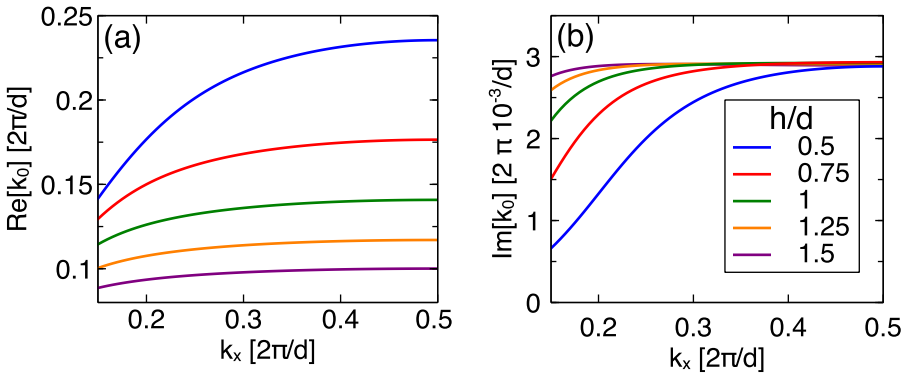

Figure 6.7: Change in the (a) real and (b) imaginary part of the spoof dispersion relation for d = 200nm and $a = 0.2d$ as the height of the groove is altered from $h = 0.5d$ to $h = 1.5d$.

changes for $a = 0.2d$, d = 200nm and for a range of heights. As we can see, the spoof SPP still retains this behaviour for the case of real metals, even if the actually modal resonance is shifted from $\lambda = 4h$, due to the increase in the effective height.

When looking at how the change in height affects the modal losses, figure 6.7 (b), we can see that as the height changes so does the curvature of the band, with the transition from low to high loss representing the transition from polariton to plasmon like states. For smaller grooves, the cross-over from polariton to plasmon type behaviour comes at a higher k_0. As with SPPs, it is the plasmon-like behaviour, highly confined fields to the metal surface, that causes the modal losses. Interestingly, the modal losses at the edge of the FBZ remain almost independent of height, despite the fact that the modes for smaller grooves show less confinement of the fields to the metal. Therefore, it appears that the modal loss at the band edge is not determined by the height of the groove and, as such, must come from the MIM wavevector.

Now, considering the changes in the dispersion relation for altering the groove width a. Figure 6.8 (a) shows how the real part of the dispersion changes for $h = d$ = 200nm and a range of groove widths. In the PEC limit the groove width has little effect on the modal frequency at the band edge, merely altering the curvature of the band, since the asymptotic frequency is determined by h. However, that is no longer the case for real metals. Whilst the width still affects the band curvature, with wider grooves having a steeper dispersion relation, the modal frequency is now drastically changed once a becomes small. If a is large the MIM wavevector p_0 follows the SPP dispersion relation, and so is independent of width. However, as a reduces the MIM wavevector alters, diverging further away from the SPP dispersion relation, see figure 6.1. As such, $p_0(a)$ and

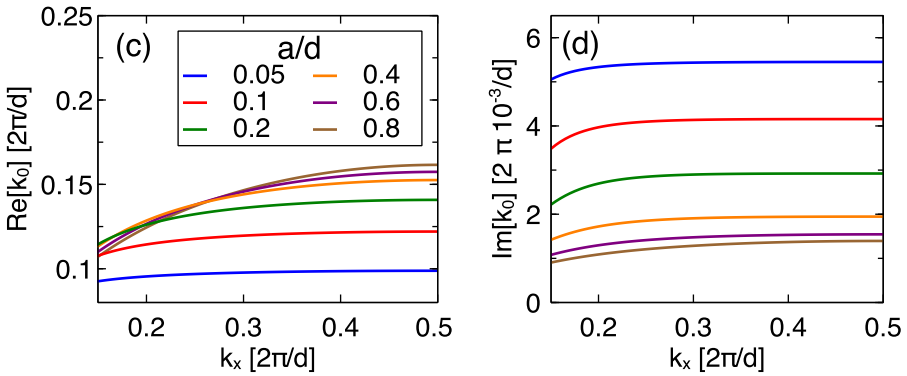

Figure 6.8: Change in the (a) real and (b) imaginary part of the spoof dispersion relation for d = 200nm and $h = d$ as the width of the groove is altered from $a = 0.05d$ to $a = 0.8d$.

thus the asymptotic frequency is strongly affected by a. For narrower slits we find that the mode is red-shifted and flattened out.

The strong dependence of p_0 on a for narrow grooves is also reflected in the modal losses illustrated in figure 6.8 (b). For wide grooves a small change in the width only slightly increases the modal loss. However, as the grooves become narrow the increase in modal loss is accelerated, causing a greater than four fold increase as a goes from 160nm to 10nm. These trends can be understood from the MIM wavevector. As a decreases p_0 diverges further from the light line, and the modal losses of the MIM mode increase. In effect the electric field within the waveguide is being squeezed between two metal plates, causing the fields to penetrate further into the two metal surfaces and increasing the loss of the mode. When comparing this to figure 6.7 (b) we can see that the modal losses at the band edge are much more dependent on the groove width than the groove height. Modal losses also occur due to absorption at the bottom of the groove, as governed by the parameter ν_m which is a function of both p_0 and h. As we saw from figure 6.3, the relative size of ν_m is drastically increased for narrow grooves. As such, ν_m compounds the increase in modal losses observed by narrowing the grooves, and also contributes to the decrease in modal frequency observed in figure 6.8 (a).

6.3.3 Potential problems with the method

Before we move it is important to consider the potential problems with the method and where errors can arise. When deriving both the MIM mode equation and the factor ν_m we assume that the propagating fields on either side of the interface have the same wavevector. This can be shown

to be true for an extended interface stretching from $-\infty$ to ∞ (see equation (6.27)), but as the interfaces used at $x = \pm a/2$ and $z = 0$, h are not infinite in extent it is no longer true. This error manifests itself in the discontinuity of the fields in the corner regions for $|x| > a/2$ and $z < 0$, see figures 6.4 (c) and (e). As we have expanded the fields for $|x| > a/2$, $z > 0$ and for $|x| \leq a/2$, $z < 0$ we can (in theory) solve Maxwell's equations in the corner regions and match the fields at the boundaries. However, the two boundary conditions cannot be matched simultaneously[3], leading to a mismatch of the fields. In figures 6.4 (c) and (e) we have plotted the average of the two fields arising from the matching at the two boundaries $z = 0$ and $|x| = a/2$. Interestingly, this error seems to have only a small effect on the numerical accuracy of the dispersion relation. We hypothesise that this is probably due to the fact that, although the fields are incorrect in this region, the majority of the fields resides within the groove, and as such this error is only small. From this we would anticipate the problem becomes worse as the fields penetrate further and deeper into the metal surfaces.

A second potential source of error in this model is the assumption that the grooves are isolated and only coupled through the Bloch modes in region I. In essence, this assumes that the grooves adjacent to groove m cannot be felt directly through the metal walls of the grooves. However, as the penetration of the fields into the metal increases then so should the effect of other grooves. To consider this we can calculate the MIM mode wavevector for an alternating M-I-M-I-M-I-M structure (M - Metal, I - Insulator) thus in effect considering three adjacent grooves. From figure 6.9 we can see that the wavevector is indistinguishable until $d - a$, the thickness of the metal layers, becomes smaller than 30nm. At this point the MIM wavevector of the mode begins to change due to the presence of adjacent grooves, indicating that the model will break down close to this limit. Note that the smallest $d - a$ used in our results is 160nm, thus we are far away from this point.

A further point of discussion is the way our model does not account for the creation and excitation of SPPs between the interfaces of regions I and II. Although we recover the SPP dispersion relation from equation (6.20), this is due to the decaying fields we impose in region III. However, it is quite possible that the MIM waveguide modes could couple to SPPs propagating along the interface between regions I and II as well as the diffracted modes incorporated into our model.

We should also consider the validity of the $m_{max} = 0$ approximation we have used throughout

[3] An error of the method, not of Maxwell's equations.

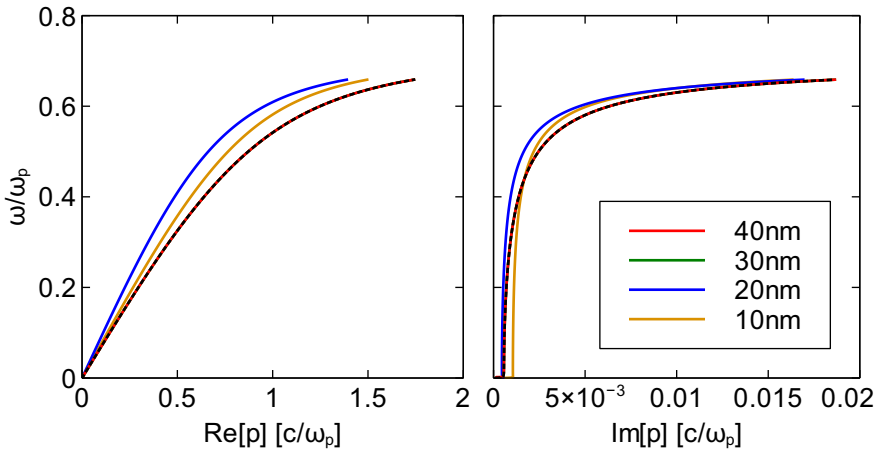

Figure 6.9: Alteration in the real (left) and imaginary (right) parts of the MIMIMIM mode wavevector p as the distance between adjacent grooves $d - a$ is decreased from 40nm to 10nm, also plotted is the MIM mode wavevector (dashed black). Note that the red (d = 40nm) and green (d = 30nm) lines overlap.

this section. For the geometries considered it is the only propagating mode within the grooves and as such dominates the interaction with the diffracted Bloch modes. As all the other modes are evanescent they die away very quickly when excited and have very little overall contribution to the confined spoof SPP surface mode. As for considering n_{max} = 10, this approximation is always checked to ensure that the mode has converged and an increasing number of Bloch modes does not alter the solution.

6.4 Extraordinary optical transmission

EOT was one of the drivers behind the discovery of spoof SPPs, given it is still an active area of research, and surface waves play an important role in the phenomena, our theory of spoof SPPs in real metals is certainly applicable. It can be used to improve the quantitative match between theory and numerical simulations/experiments, as well as providing an analysis of the loss mechanisms and how the structural variation influences these. In the following we provide a quick review of EOT before extending our CMM to consider the phenomenon, comparing with both previous theoretical considerations and numerical simulations, before also considering how the geometry affects the absorption and modal loss characteristics.

6.4.1 History of EOT

EOT is the the phenomenon whereby a surface containing a periodic array of holes (and which is otherwise opaque) has a higher transmission than could be expected by considering ray optics or the transmission of light through single apertures [14]. In the first paper by Ebbesen et al. [13], holes were milled in an optically thick metal layer (where the thickness is much greater than the skin depth), and hence the only way light could travel to the far side of the sheet was through the holes. Surprisingly, for certain wavelengths, they showed that this periodic array of holes transmits more light than one large hole with an equivalent area as all the small holes put together. Also, the transmission efficiency (the power transmitted divided by the power received) normalised to the hole area was sometimes greater than 1. Furthermore, this was doubly surprising as it was known that the efficiency of a single subwavelength hole was poor due to two factors; the small coupling between the modes inside and outside the hole [148] and the evanescent decay of the modes propagating in the hole [149].

The history of EOT is rich and extensive, covering individual one dimensions holes [63] two dimensional holes [13], holes surrounded by arrays of grooves [150, 151], finite arrays [152], quasi-periodic arrays [153] and even Penrose tilings [154]. Importantly, it is found that in general there are two mechanisms for the resonant transmission of light from one side of the film to the other; the coupling of the SPPs of either interface (either directly coupled if the film is thin or indirectly coupled via the the holes) and the excitation of resonant Fabry-Perot modes within the hole [14]. Note that although here we have defined them as two separate mechanisms they are not strictly uncoupled and as such EOT can be seen as arising from the interplay between of these two effects.

There have several works considering SIBCs [26, 145, 144] to approximate the metallic film within the EOT process. However, similar to the spoof plasmon case these works only enforce the SIBCs at the horizontal interfaces and not along the hole walls. As we have seen in the previous section this can lead to large discrepancies between theory and numerical simulations, as the propagating wavevector within the grooves is incorrect.

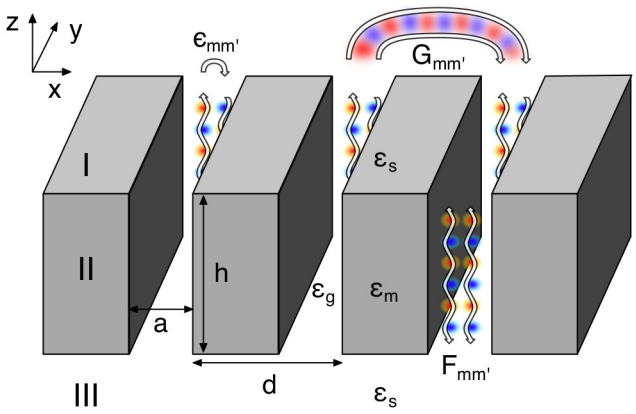

Figure 6.10: Layout of the 1D array of slits, including schematic depiction of the terms in equation (7.30).

6.4.2 Theory of EOT in real metals

The general structure of the 1D array of holes is shown in figure 6.10. As we are are dealing with a system that is under illumination we include an incident field term in the CMM and the magnetic field in region I ($z > h$) becomes

$$H_y^{\mathrm{I}} = I\phi_0 e^{-ig_0 z} + \sum_{n=-\infty}^{\infty} r_n \phi_n(x) e^{ig_n z}. \tag{6.29}$$

Note that now $Z_n = -g_n/\omega\varepsilon_0\varepsilon_s$, $g_n = \sqrt{\varepsilon_s k_0^2 - k_n^2}$ and I is the arbitrary constant determining the incident field amplitude. The magnetic field in region II ($0 \leq z \leq h$) is expanded over the same basis of MIM waveguide modes, as before, yielding

$$H_y^{\mathrm{II}} = \sum_{m=0}^{\infty} \left(A_m e^{ip_m z} + B_m e^{ip_m z} \right) \begin{cases} \chi_m^+(x) & x > a \\ \chi_m(x) & -a < x < a \\ \chi_m^-(x) & x < -a \end{cases} . \tag{6.30}$$

Finally in region III ($z < 0$) the magnetic field is again expanded in Bloch modes as

$$H_y^{\mathrm{III}} = \sum_{n=-\infty}^{\infty} t_n \phi_n(x) e^{-ig_n z}. \tag{6.31}$$

Applying the continuity equations and the matching procedure allows us to find the master equation for EOT. It is convenient to transform from the unknowns A_m and B_m into new constants $E_m^+ =$

$Z_m[A_m \exp(ip_m h) - B_m \exp(-ip_m h)]$ and $E_m^- = Z_m[A_m - B_m]$ which are the amplitudes of the MIM waveguide mode electric field at the top and bottom of the grooves. Finally, after some algebra, we find the system equations are

$$\begin{aligned} \sum_m E_m^+(G_{mm'} - \epsilon_{mm'}) + \sum_m E_m^- F_{mm'} &= I_{m'} \\ \sum_m E_m^-(G_{mm'} - \epsilon_{mm'}) + \sum_m E_m^+ F_{mm'} &= 0 \end{aligned}, \tag{6.32}$$

where $\epsilon_{mm'}$ and $G_{mm'}$ are defined as before (equations 7.12 and 7.13) except that now there is an extra factor of $-i$ included in the $G_{mm'}$ term, and we set $\nu_m = 0$ within the $\epsilon_{mm'}$ term. The new terms, $F_{mm'}$ and $I_{m'}$, are the coupling of the fields on one side of the groove with the other through the waveguide modes and the excitation of the waveguide modes via the incident fields respectively. They are defined as

$$F_{mm'} = \frac{Z_m}{\sin(p_m h)} T_{mm'}, \tag{6.33}$$

$$I_{m'} = I e^{-ig_0 h} S_{0m'}^H. \tag{6.34}$$

Combining equations (6.32) yields a matrix equation and, as with the CDA, there are two ways to solve the problem; either solving for the modes ($k_0(k_x)$) in the absence of an incident field or imposing a known field (in which case the incident field imposes the phase $kx = k_0 \sin\theta$ on the system) and calculating the transmission and reflection coefficients in dependence of the incident amplitude. To calculate the transmission through an array of slits we can use Poynting's theorem and calculate the power flux through an area below the slits across the unit cell, the transmission = transmitted power/incident power;

$$T = \frac{\frac{1}{2}\int_{-d/2}^{d/2} \mathrm{Re}\left[E_x^{III}(x, z_t) \times (H_y^{III}(x, z_t))^*\right] dx}{\frac{1}{2}\int_{-d/2}^{d/2} \mathrm{Re}\left[I\zeta_0\phi_0(x)e^{-ig_0 z_i} \times \left(I\phi_0(x)e^{-ig_0 z_i}\right)^*\right] dx}, \tag{6.35}$$

where the fields are calculated at positions $z = z_i$ and $z = z_t$, above and below the slits.

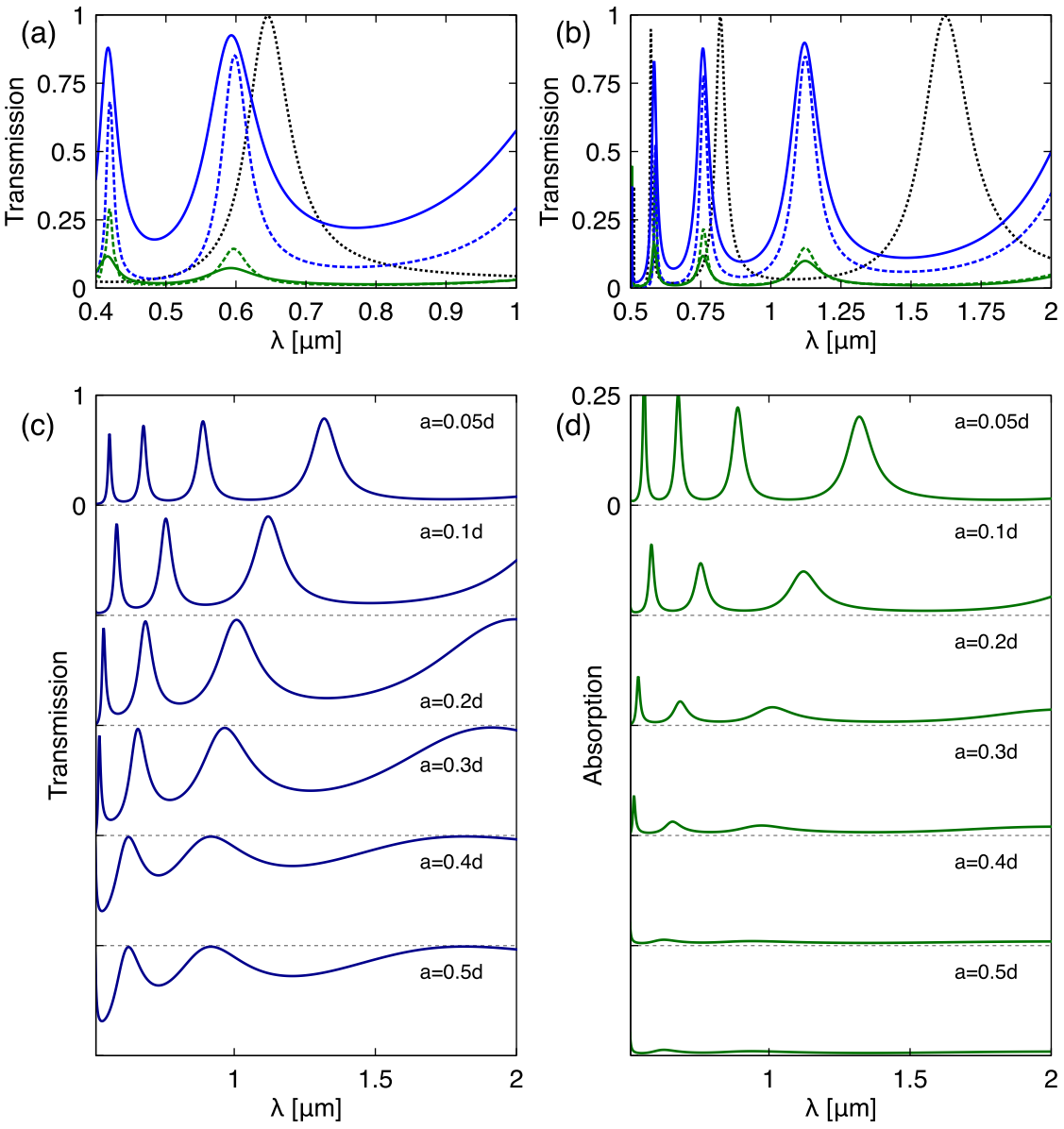

Figure 6.11: Upper section: comparison of the spectra produced by a 1D array of slits with dimensions (a) d = 500nm and (b) d = 200nm, where $a = 0.2d$ and $h = 1.5d$. The solid lines represent the CMM method derived in this chapter, the dashed lines FDTD simulations and the dotted line the SIBC method calculated from [26]. The blue lines represent the transmission spectra and the green lines the absoprtion spectra. Note that, to avoid confusion, only the transmission (black-dotted line) calculated from the SIBC method is shown.
Lower section: blue-shifting of the transmission (c) and absorption (d) spectra as a is decreased from $a = 0.05d$ to $a = 0.5d$ for d = 500nm and $h = 1.5d$.

6.4.3 Results

In figures 6.11 (a) and (b) our CMM method (solid lines) can be compared with numerical simulations (dashed lines) and previous methods using SIBCs (dotted black line) [26], showing both the transmission spectra (blue lines) and absorption spectra (green lines) for $a = 0.1d$, $h = 1.5d$ and $d = 200$nm (figures 6.11 (a)) and $d = 500$nm (figures 6.11 (b)). For clarity we have omitted the reflection spectra and only included the transmission spectra from the SIBC method. There is a marked difference between the CMM with the MIM modes and the SIBCs. The presence of the MIM modes within the slits causes the wavelength of the cavity resonances (of the slits) to be significantly red-shifted to longer values. We note that the transmission peak from the SIBC method in figure 6.11 (a) at around 650nm is red-shifted to wavelengths greater than 1μm in the MIM method.

As the transmission peaks are strongly associated to the coupling of the incident waves to the cavity resonances it is not surprising that the use of MIM waveguide modes causes a strong red-shift of the transmission peaks. Importantly, as shown in figures 6.11 (a) and (b), the comparison between numerical simulations and theory demonstrates that the CMM we have developed in this chapter is a much better fit than employing SIBCs.

There are discrepancies between the theoretical model and the numerical simulations. Perhaps most notably the size of the transmission spectrum is slightly overestimated by the theoretical model, meaning the dips in transmission are not as low. Despite the transmission peaks appearing at the incorrect spectral positions, the amplitude of the transmission dips is well recovered by using SIBCs. One major difference that occurs through the use of SIBCs is the potential to excite SPPs on the interfaces between regions I-II and II-III, something which our CMM model does not include. It seems likely that the admission of these extra loss channels is one of the reasons for the mismatches in the amplitude of the transmission spectra. Furthermore, the theory slightly underestimates the size of the red-shift for the visible transmission peaks, and underestimates the associated absorption. It seems likely that these effects could be due to the method neglecting the potential for exciting SPPs along the horizontal interfaces.

As we have already seen from the spoof SPP case, the groove width can have a large effect on both the modal frequency and the modal losses. In the context of EOT, despite the fact that

the geometric parameters have been extensively explored, there has been very little consideration of the effect of the groove width on the spectral response. In figures 6.11 (c) and (d) we consider the transmission and absorption ($A = 1 - T - R$, where T and R are the total transmission and reflection from the array) properties for a range of widths ($a = 0.05 - 0.5d$) with d = 500nm and $h = 1.5d$ as this will allow us to understand the effect of a on both the spectral position of the peaks and the system losses. We do this only for the d = 500nm case as this is where there is a very good match between theory and numerical simulations.

From figure 6.11 (c) we see that the transmission peaks significantly broaden and red-shift due to the decreasing slit width. Similarly, from figure 6.11 (d) the absorption peaks also red-shift and increase significantly in height as a is increased. Both of these effects are caused by the MIM wavevector within the slits. As a decreases, the MIM mode diverges further from the light-line, whilst also the decay of the waveguide mode Im[p_0] increases, causing both the red-shifting of the modes and the increased absorption. Once again, this highlights that the losses are not only dependent on the material parameters but also the particular geometry of the system.

The applications of EOT structures are numerous, including; sensing and spectroscopy [155, 156, 157], enhancement of photo-emitters [158] and detectors [159] and optical control [160, 161, 162]. Within this context the geometry of the holes has only been used to consider the spectral position (via h and d) and to control the broadness and height of the transmission peak [155]. As such, the effect that the hole geometry has on both the absorption and spectral position should be a valuable addition for the transfer of any applications to the small groove geometries that are necessary in the optical and near-IR regimes.

6.5 Loss compensation of spoof SPPs

As we have explained in the previous sections, one of the main benefits of our method is the ability to understand the modal loss of spoof SPPs directly through the theoretical model. Importantly, throughout the method we do not assume anything about the dielectric constant ε_m, thus any metal that can be assigned a dielectric constant (either via a Drude model, an interpolation of experimental data or other means) can be inserted into equation (6.13) and the modes solved. We have noted that the losses of spoof SPPs rise rapidly as the wavelengths under consideration

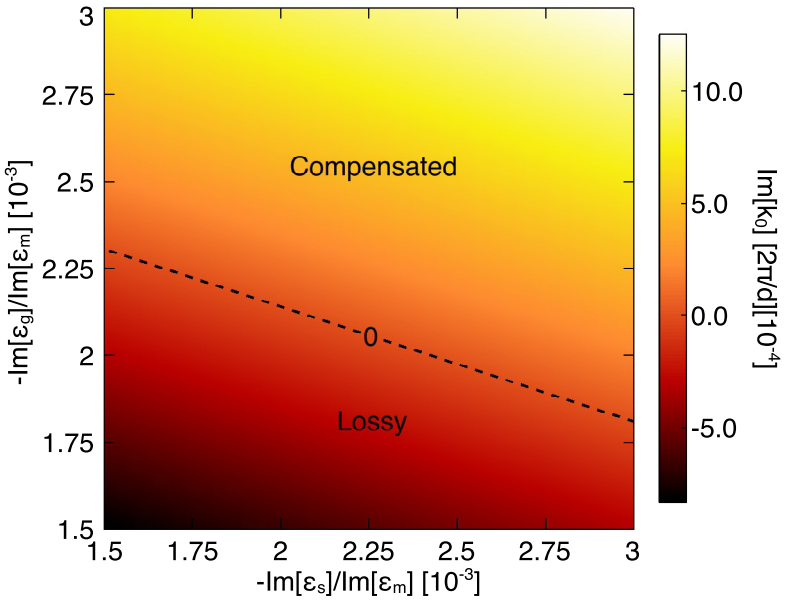

Figure 6.12: Variation of $Im[k0](k_x = \pi/d)$ as the imaginary components of ε_s and ε_g are altered. The dashed line indicates the point at which the mode becomes fully loss compensated.

enter the IR and optical spectral regimes, and that these losses are highly dependent on the geometry, in particular on the groove width. To provide a barometer of the effects of these losses on potential IR/optical spoof SPP applications, in this section, we consider whether these losses can be efficiently compensated.

One of the avenues by which the losses can be overcome is the direct incorporation of gain media into the structure to compensate for them at their source. To do this within the frequency domain CMM we consider a simple linear gain material, incorporated within the grooves and above them. Thus, the terms ε_g and ε_s become complex, with a negative imaginary component that leads to gain within these regions. Although this neglects the particular dynamics of gain materials, in particular the feedback between the carriers, polarisation and electric fields, what it should provide is a way to measure the effects of a linear gain media upon the modal losses of the system. Furthermore, such a study can provide us with estimates to the amount of gain necessary to fully compensate the losses, and how this can be optimised through the spoof SPP geometry.

Figure 6.12 demonstrates how the losses at the edge of the band ($k_x = \pi/d$) can be compensated for a structure with parameters $d = 200$nm, $a = 0.2d$ and $h = 1.125d$, giving $\mathrm{Re}[\lambda] = \mathrm{Re}[2\pi/k_0(k_x = \pi/d)] = 1.56\mu m$. The gain is varied through the imaginary components of ε_g

and ε_s, with both varying from -1.5 to -3 Im$[\varepsilon_m(ck_0(k_x = \pi/d))]$. Interestingly, the loss is more sensitive to the gain within the grooves than above them. The modal loss occurs due to the absorptive side walls of the grooves, whilst the electric fields are typically within the groove opening. Thus, it is at this point where the gain has the largest effect in compensating the modal losses. The overall modal loss, Im$[k_0]$, is linear with Im$[\varepsilon_g]$ and Im$[\varepsilon_s]$, and we can see that doubling Im$[\varepsilon_g]$ (Im$[\varepsilon_s]$) whilst keeping Im$[\varepsilon_s]$ (Im$[\varepsilon_g]$) constant leads to a shift in Im$[k_0]$ of $\sim 15 \times 10^{-4} 2\pi/d$ ($\sim 5 \times 10^{-4} 2\pi/d$). Therefore, the modal losses are ~ 3 times as sensitive to gain within the grooves than above them.

The dashed line in figure Figure 6.12 shows the transition of the mode from lossy to lossless. We can see that this appears around Im$[\varepsilon_g]$ = Im$[\varepsilon_s]$ = 2.25×10^{-3}Im$[\varepsilon_m]$. At telecommunications wavelength $\lambda \approx 1.55\mu$m the material loss of the Drude mode we have considered is Im$[\varepsilon_m]$ = 16.017 giving values for Im$[\varepsilon_g]$ and Im$[\varepsilon_s]$ of -0.036. When we compare this to recent work considering loss compensation of MIM waveguide modes [163] this gives a gain of approximately $420cm^{-1}$. Another way to consider the amount of gain required is to consider the losses per unit time. All our fields are assumed to oscillate $\propto \exp(-ik_0ct)$. For complex k_0, the modal losses lead to Im$[k_0] < 0$ and thus produce fields that decay over time. If we provide a gain material, this amplifies the power $\propto exp(GL)$ where G is the gain of the material per unit length and L is the distance the mode travels. Combing these together we find that, for loss compensation

$$2\text{Im}[k_0]ct + GL = 0. \tag{6.36}$$

Equating ct with the unit of length L allows us to describe the gain required, G in terms of the modal loss, Im$[k_0]$. The modal losses for $a = 0.2d$, $h = 1.125d$ and d = 200nm at the band edge are $-2.92 \times 10^{-3}[2\pi/d]$ which yields a required gain of $450cm^{-1}$. This is of the same order as the gain coefficient we calculated using [163]. This is well within the range of semiconductor gain media [164]. This gain will have to be provided per unit time, and, as we have equated $ct = 1cm$, this requires an amplification rate of $4.24 \times 10^{12}s^{-1}$. Whilst there are certainly multiple challenges in using gain as an efficient tool to compensate the losses of plasmonic systems [164, 165] these results suggest that the loss compensation of the spoof SPP is within the realms of possibility.

6.6 Summary

In this chapter we have presented a theory of spoof SPPs that is valid in metals from just below the plasma frequency to low frequencies where the metal behaves as a perfect conductor. The incorporation of the material properties into the spoof SPP model results in a new effective width and height of the groove through the parameters p_m, the MIM mode wavevector, and ν_m, the reflection of the fields at the bottom of the grooves. Importantly, our model recovers both the spoof SPP dispersion relation in the limit that the metal behaves as a PEC and the SPP in the limit that the groove area tends to zero, resulting in a flat interface. After comparison with previous attempts at modeling the spoof SPPs within a real metal we have found that our method is much more accurate, especially in the optical and near-IR frequency ranges. Furthermore, our model has enabled a proper analysis of the spoof SPP modal loss characteristics for the first time. We have found that the both the modal frequency and the modal losses are intrinsically tied to the geometric and material parameters and that the groove width a is key in determining the loss characteristics.

We have then extended our model to consider the 1D array of slits, a well know EOT structure. As in the case of grooves, the effect of the MIM wavevector causes the transmission peaks to red-shift as the groove width is decreased and also increases the associated modal absorption. Furthermore, the CMM method is able to reproduce the position of the transmission peaks through the system to a much higher accuracy than SIBC methods.

Finally we have considered the prospect of using a linear gain medium to compensate the losses of the spoof SPP modes. We have shown that the grooves have a much higher sensitivity to gain placed within them, than without, and that gain coefficients in the region of $400\text{cm}-1$ would be necessary to fully compensate the spoof plasmon modal losses.

7 Conclusions

Throughout this thesis we have studied the surface modes of structured plasmonic arrays. In the first half we have been concerned with the array of cut-wires coupled to a dielectric waveguide. We have considered the differences between TE and TM modes, noting that TE modes tend to have lower losses and lead to longer propagation distances when interacting with metallic surfaces. Considering the coupling, we have found that the hybridisation of the cut-wire modes with those of the waveguide leads to WPPs, and also a third low-loss EIT type mode. The transmission profile of incident light through the array is increased via this low-loss mode, and its spectral position and shape can be tuned through the array spacing and the waveguide buffer layer, enabling extremely narrow transmission peaks.

We have considered the cut-wire on waveguide array as CROW and investigated how the geometry can be used to tune the dispersion of the structure. At the edge of the FBZ the degeneracy of the waveguide modes, which results in the EIT peak, also causes a low-loss mode in the dispersion relation, where the interference of the waveguide modes avoids coupling to the cut-wires. This mode can be tuned directly through the cut-wire parameters and it exhibits extremely low losses at the edge of the FBZ. Next, we have looked into finite cut-wire arrays, finding that the structure supports Fabry-Perot type resonances and that the highest order cavity modes retain the avoided coupling to the cut-wires, causing them to have dramatically reduced losses. As such, Q-factors of 4000 and above can be created through the hybridisation of the plasmonic cut-wires and the photonic waveguide. Furthermore, we have demonstrated how the individual loss channels of the highest order mode can be tuned through the specific geometry of the system, enabling the transfer of losses from dissipative absorption to potentially useful propagating waveguide modes. We have briefly investigated disorder in the array period and found that through a small detuning of the cut-wire from the waveguide modes at the edge of the FBZ, the hybrid cavity modes can be made

to be robust, retaining their Q-factors in the presence of random disorder on the nanometre scale. Finally, we have considered the cut-wire device as a passive delay line and found that, despite the use of lossy cut-wire resonators, the side-coupled CROW scheme which enables the formation of loss low modes means the system has the same order of transmittivity as traditional dielectric based CROWs.

As for the future development of these ideas, it would be important to incorporate experimental evidence when analysing the cut-wire arrays. Whilst we have looked into random disorders of the order 2.5nm, which are within the range of EBL techniques, it is important to validate that these devices can be produced in the lab. The system is designed to be simple to fabricate, building metallic particles on industry standard dielectric wafers. There is also the potential to consider the cavity lasing of a finite CROW. The mode discrimination, due to the steep increase in loss as the mode order decreases, should lead to a single mode lasing device, which could be easily incorporated in the SOI platforms and has the additional benefit of emitting directly into waveguide modes, allowing the light to be funneled for use elsewhere.

In the second half of the thesis we have been concerned with the surface modes produced by periodically texturing a planar metallic layer. First, we reviewed the spoof SPP and then considered altering the traditional spoof rectangular indentations to analyse the affect on the spoof SPP characteristics. We employed the coupled mode method to consider the effect of incorporating a slant angle into the grooves, with the effect that the spoof SPP modes become less confined to the surface and blue-shift as the angle increases. Finally, we considered a limiting case of the model to investigate right-angled triangular indentations, a spoof geometry very different to those normally considered. Here we found that indentations with the largest perpendicular distance into the metal surface produced the highest confinement of the modes, and lowers the energy of the spoof SPP dispersion relation.

The design of the spoof SPP plasma frequency through geometric parameters enables the designer to tune both the position and shape of the dispersion band, tailoring the structure for their needs. Whilst this freedom of design exists for THz and lower frequency spoof SPPs, the metal dispersion at IR and optical frequencies means that existing theoretical descriptions do not accurately predict the spoof SPP characteristics for higher frequency regimes. In chapter 6, we extended the CMM to real metals by using MIM waveguide modes within the rectangular grooves. This method

recovers both; the spoof SPP dispersion relation for PECs in the limit that $\epsilon_m \to -\infty$ and the SPP dispersion relation as the groove area $\to 0$, leaving a planar metal dielectric interface, presenting an accurate method of spoof SPPs for optical frequencies and below. Importantly, this method also allows an analysis of the modal losses of spoof SPPs and their geometric dependence. We find that the groove width is an extremely important parameter in smaller structures, as the squeezing of the MIM model leads to a red-shifting of the mode and an increased modal loss, processes which accelerate as the width becomes smaller. Despite the good agreement between theory and simulations, the method is not applicable for very small distances between adjacent grooves ($\leq$ 40nm); then the grooves can no longer be considered isolated as the skin depth into the metal extends from the MIM mode into the grooves either side. Furthermore, the method leads to small discontinuities in the field profiles due to the treatment of the grooves as semi-infinite MIM waveguides. We have also considered the applicability of MIM modes to the EOT phenomena using the CMM, finding that MIM modes are necessary to get the required red-shifts of the transmission spectra at the optical and IR frequencies. However, the method underestimates significantly the absorption losses as it does not consider the direct excitation of SPPs on the horizontal interfaces. Finally, we have considered whether the losses of the spoof SPP modes can be overcome with gain media. Using a simple frequency domain analysis we find that the spoof SPP modes are much more susceptible to gain within the grooves than above them, and that, at λ = 1550nm, the gain required is well within the range of current semi-conductor materials.

Overall, the theoretical model we have presented means that the design and tuning of structural metallic surfaces in the IR and optical regime can be done quickly and semi-analytically rather than relying on intensive numerical calculations. Both our studies on slanted and real metal spoof SPP modes confirm that it is the optical path length of the surface indentations that is important when determining the spoof SPP characteristics rather than a specific geometric parameter. Hopefully, it should also provide an avenue whereby the losses of spoof plasmon devices in the THz and on the cusp of the IR spectral regions can be considered and even minimised via the geometric parameters. As for further work on these ideas, the incorporation of MIM modes into the CMM formalism means that if should be straightforward to transfer other spoof SPP designs into dispersive materials. Recently, there has been interest in using defect modes within spoof plasmon structures to produce novel toroidal resonances that exhibit small mode volumes and high Q-factors through

the use of a two dimensional groove metal array [166]. Such a defect mode would be highly desirable for plasmonic systems which, whilst providing small mode volumes, do not typically have high Q-factors. However, extending the theory to 2D modes and defects is non-trivial due to the problems when describing 3D dielectric waveguide modes where exact analytical solutions are rare. Although methods exist to describe these modes (for instance see Marcatili's method [167]) these are approximate and do not generally apply to a high index contrast between the cladding and core, which is the case of MIM waveguides. As such, in these cases, it may be more appropriate to apply the CMM as a general guide to the expected spoof SPP characteristics before optimising with numerical tools.

Publications

The following publications are as a result of the work presented within this thesis

1. J. J. Wood, L. Tomlinson, O. Hess, S. Maier and A. Fernandez-Dominguez, *Spoof plasmon polaritons in slanted geometries.* Physical Review B **85** 075441 (2012).

2. J. J. Wood, L. Lafone, J. M. Hamm, O. Hess and R. F. Oulton, *Plasmonic CROWs for tunable dispersion and high quality cavity modes.* Scientific Reports **5** 17724 (2015).

Bibliography

[1] Sommerfeld, A. *Ueber die Fortpflanzung elektrodynamischer Wellen längs eines Drahtes*. Annalen der Physik **303**, 2 233 (1899).

[2] Zenneck, J. *Über die Fortpflanzung ebener elektromagnetischer Wellen längs einer ebenen Leiterfläche und ihre Beziehung zur drahtlosen Telegraphie*. Annalen der Physik **328**, 10 846 (1907).

[3] Wood, R. *A suspected case of the electrical resonance of minute metal particles for light-waves. A new type of absorption*. Proceedings of the Physical Society of London **18**, 1 166 (1902).

[4] Fano, U. *The theory of anomalous diffraction gratings and of quasi-stationary waves on metallic surfaces (Sommerfelds waves)*. JOSA **31**, 3 213 (1941).

[5] Ritchie, R. *Plasma losses by fast electrons in thin films*. Physical Review **106**, 5 874 (1957).

[6] Ritchie, R., Arakawa, E., Cowan, J. & Hamm, R. *Surface-plasmon resonance effect in grating diffraction*. Physical Review Letters **21**, 22 1530 (1968).

[7] Kretschmann, E. & Raether, H. *Notizen: Radiative Decay of Non Radiative Surface Plasmons Excited by Light*. Zeitschrift für Naturforschung A **23**, 12 2135 (1968).

[8] Barnes, W. L., Dereux, A. & Ebbesen, T. W. *Surface plasmon subwavelength optics*. Nature **424**, 6950 824 (2003).

[9] Ebbesen, T. W., Genet, C. & Bozhevolnyi, S. I. *Surface-plasmon circuitry*. Physics Today **61**, 5 44 (2008).

[10] Pendry, J. B., Holden, A. J., Robbins, D. & Stewart, W. *Magnetism from conductors and enhanced nonlinear phenomena*. Microwave Theory and Techniques, IEEE Transactions on **47**, 11 2075 (1999).

[11] Pendry, J. B. *Negative refraction makes a perfect lens*. Physical review letters **85**, 18 3966 (2000).

[12] Schurig, D., Mock, J., Justice, B., Cummer, S. A., Pendry, J. B., Starr, A. & Smith, D. *Metamaterial electromagnetic cloak at microwave frequencies*. Science **314**, 5801 977 (2006).

[13] Ebbesen, T. W., Lezec, H. J., Ghaemi, H. F., Thio, T. & Wolff, P. A. *Extraordinary optical transmission through sub-wavelength hole arrays*. Nature **391** 667 (1998).

[14] Garcia-Vidal, F. J., Martin-Moreno, L., Ebbesen, T. & Kuipers, L. *Light passing through subwavelength apertures*. Reviews of Modern Physics **82**, 1 729 (2010).

[15] Christ, A., Tikhodeev, S. G., Gippius, N. A., Kuhl, J. & Giessen, H. *Waveguide-Plasmon Polaritons: Strong Coupling of Photonic and Electronic Resonances in a Metallic Photonic Crystal Slab*. Phys. Rev. Lett. **91** 183901 (2003).

[16] De Abajo, F. G. *Colloquium: Light scattering by particle and hole arrays*. Reviews of Modern Physics **79**, 4 1267 (2007).

[17] Liu, H. & Lalanne, P. *Microscopic theory of the extraordinary optical transmission*. Nature **452**, 7188 728 (2008).

[18] Valentine, J., Zhang, S., Zentgraf, T., Ulin-Avila, E., Genov, D. A., Bartal, G. & Zhang, X. *Three-dimensional optical metamaterial with a negative refractive index*. Nature **455**, 7211 376 (2008).

[19] Zou, S., Janel, N. & Schatz, G. C. *Silver nanoparticle array structures that produce remarkably narrow plasmon lineshapes*. The Journal of chemical physics **120**, 23 10871 (2004).

[20] Kravets, V., Schedin, F., Kabashin, A. & Grigorenko, A. *Sensitivity of collective plasmon modes of gold nanoresonators to local environment*. Optics letters **35**, 7 956 (2010).

[21] Hess, O., Pendry, J., Maier, S., Oulton, R., Hamm, J. & Tsakmakidis, K. *Active nanoplasmonic metamaterials*. Nature materials **11**, 7 573 (2012).

[22] Hess, O. & Tsakmakidis, K. L. *Metamaterials with quantum gain*. nanoscale **1** 2 (2013).

[23] Oulton, R. F., Sorger, V. J., Genov, D., Pile, D. & Zhang, X. *A hybrid plasmonic waveguide for subwavelength confinement and long-range propagation*. Nature Photonics **2**, 8 496 (2008).

[24] Pendry, J. B., Martn-Moreno, L. & Garcia-Vidal, F. J. *Mimicking Surface Plasmons with Structured Surfaces*. Science **305**, 5685 847 (2004).

[25] Pors, A., Moreno, E., Martin-Moreno, L., Pendry, J. B. & Garcia-Vidal, F. J. *Localized spoof plasmons arise while texturing closed surfaces*. Physical review letters **108**, 22 223905 (2012).

[26] Garcia-Vidal, F. & Martin-Moreno, L. *Transmission and focusing of light in one-dimensional periodically nanostructured metals*. Physical Review B **66**, 15 155412 (2002).

[27] Rusina, A., Durach, M., Nelson, K. A. & Stockman, M. I. *Nanoconcentration of terahertz radiation in plasmonic waveguides*. Optics express **16**, 23 18576 (2008).

[28] Moller, P. *Electric Fish*. BioScience **41**, 11 794 (1991).

[29] Seeman, B. & Barry, J. E. *The Story of Electricity and Magnetism* (Harvey House, 1967).

[30] Maxwell, J. C. *A Dynamical Theory of the Electromagnetic Field*. Philosophical Transactions of the Royal Society of London **155** 459 (1865).

[31] Jackson, J. D. *Classical Electrodynamics*. 3rd edition (Wiley, 1999).

[32] Maier, S. A. *Plasmonics: fundamentals and applications* (Springer Science & Business Media, 2007).

[33] Bohren, C. F. & Huffman, D. R. *Absorption and scattering of light by small particles* (John Wiley & Sons, 2008).

[34] Ashcroft, N. W. & Mermin, N. D. *Solid State Physics* (Saunders College, 1976).

[35] Johnson, P. B. & Christy, R. W. *Optical Constants of the Noble Metals*. Phys. Rev. B **6** 4370 (1972).

[36] Hu, J. & Menyuk, C. R. *Understanding leaky modes: slab waveguide revisited*. Advances in Optics and Photonics **1**, 1 58 (2009).

[37] Martín-Moreno, L., García-Vidal, F. J., Lezec, H. J., Pellerin, K. M., Thio, T., Pendry, J. B. & Ebbesen, T. W. *Theory of Extraordinary Optical Transmission through Subwavelength Hole Arrays*. Phys. Rev. Lett. **86** 1114 (2001).

[38] Zhou, W., Dridi, M., Suh, J. Y., Kim, C. H., Co, D. T., Wasielewski, M. R., Schatz, G. C., Odom, T. W. *et al. Lasing action in strongly coupled plasmonic nanocavity arrays*. Nature nanotechnology **8**, 7 506 (2013).

[39] Wuestner, S., Pusch, A., Tsakmakidis, K. L., Hamm, J. M. & Hess, O. *Overcoming losses with gain in a negative refractive index metamaterial*. Physical review letters **105**, 12 127401 (2010).

[40] Hentschel, M., Saliba, M., Vogelgesang, R., Giessen, H., Alivisatos, A. P. & Liu, N. *Transition from isolated to collective modes in plasmonic oligomers*. Nano letters **10**, 7 2721 (2010).

[41] Brongersma, M. L., Hartman, J. W. & Atwater, H. A. *Electromagnetic energy transfer and switching in nanoparticle chain arrays below the diffraction limit*. Physical Review B **62**, 24 R16356 (2000).

[42] Maier, S. A., Kik, P. G. & Atwater, H. A. *Optical pulse propagation in metal nanoparticle chain waveguides*. Physical Review B **67**, 20 205402 (2003).

[43] Zou, S., Janel, N. & Schatz, G. C. *Silver nanoparticle array structures that produce remarkably narrow plasmon lineshapes*. The Journal of chemical physics **120**, 23 10871 (2004).

[44] Maier, S. A., Kik, P. G., Atwater, H. A., Meltzer, S., Harel, E., Koel, B. E. & Requicha, A. A. *Local detection of electromagnetic energy transport below the diffraction limit in metal nanoparticle plasmon waveguides*. Nature materials **2**, 4 229 (2003).

[45] Markel, V. *Coupled-dipole approach to scattering of light from a one-dimensional periodic dipole structure*. Journal of Modern Optics **40**, 11 2281 (1993).

[46] Weber, W. & Ford, G. *Propagation of optical excitations by dipolar interactions in metal nanoparticle chains*. Physical Review B **70**, 12 125429 (2004).

[47] Koenderink, A. F. & Polman, A. *Complex response and polariton-like dispersion splitting in periodic metal nanoparticle chains*. Physical Review B **74**, 3 033402 (2006).

[48] Fung, K. H. & Chan, C. *Plasmonic modes in periodic metal nanoparticle chains: a direct dynamic eigenmode analysis*. Optics letters **32**, 8 973 (2007).

[49] Park, S. Y. & Stroud, D. *Surface-plasmon dispersion relations in chains of metallic nanoparticles: An exact quasistatic calculation*. Physical Review B **69**, 12 125418 (2004).

[50] Zou, S. & Schatz, G. C. *Narrow plasmonic/photonic extinction and scattering line shapes for one and two dimensional silver nanoparticle arrays*. The Journal of chemical physics **121**, 24 12606 (2004).

[51] Citrin, D. *Plasmon-polariton transport in metal-nanoparticle chains embedded in a gain medium*. Optics letters **31**, 1 98 (2006).

[52] Alu, A. & Engheta, N. *Theory of linear chains of metamaterial/plasmonic particles as subdiffraction optical nanotransmission lines*. Physical Review B **74**, 20 205436 (2006).

[53] Brandl, D. W., Oubre, C. & Nordlander, P. *Plasmon hybridization in nanoshell dimers*. The Journal of Chemical Physics **123**, 2 024701 (2005).

[54] Belov, P. A. & Simovski, C. R. *Homogenization of electromagnetic crystals formed by uniaxial resonant scatterers*. Physical Review E **72**, 2 026615 (2005).

[55] Sheikholeslami, S. N., García-Etxarri, A. & Dionne, J. A. *Controlling the interplay of electric and magnetic modes via Fano-like plasmon resonances*. Nano letters **11**, 9 3927 (2011).

[56] Jenkins, S. D. & Ruostekoski, J. *Theoretical formalism for collective electromagnetic response of discrete metamaterial systems*. Physical Review B **86**, 8 085116 (2012).

[57] Courant, R. *et al. Variational methods for the solution of problems of equilibrium and vibrations*. Bull. Amer. Math. Soc **49**, 1 1 (1943).

[58] Yee, K. S. *et al. Numerical solution of initial boundary value problems involving Maxwells equations in isotropic media*. IEEE Trans. Antennas Propag **14**, 3 302 (1966).

[59] Joannopoulos, J. D., Johnson, S. G., Winn, J. N. & Meade, R. D. *Photonic crystals: molding the flow of light* (Princeton university press, 2011).

[60] Prodan, E., Radloff, C., Halas, N. J. & Nordlander, P. *A hybridization model for the plasmon response of complex nanostructures*. Science **302**, 5644 419 (2003).

[61] Shalaev, V. M., Cai, W., Chettiar, U. K., Yuan, H.-K., Sarychev, A. K., Drachev, V. P. & Kildishev, A. V. *Negative index of refraction in optical metamaterials*. Optics letters **30**, 24 3356 (2005).

[62] Liu, N., Langguth, L., Weiss, T., Kästel, J., Fleischhauer, M., Pfau, T. & Giessen, H. *Plasmonic analogue of electromagnetically induced transparency at the Drude damping limit*. Nature materials **8**, 9 758 (2009).

[63] Porto, J., Garcia-Vidal, F. & Pendry, J. *Transmission resonances on metallic gratings with very narrow slits*. Physical review letters **83**, 14 2845 (1999).

[64] Luk'yanchuk, B., Zheludev, N. I., Maier, S. A., Halas, N. J., Nordlander, P., Giessen, H. & Chong, C. T. *The Fano resonance in plasmonic nanostructures and metamaterials*. Nature materials **9**, 9 707 (2010).

[65] Zentgraf, T., Zhang, S., Oulton, R. F. & Zhang, X. *Ultranarrow coupling-induced transparency bands in hybrid plasmonic systems*. Phys. Rev. B **80** 195415 (2009).

[66] Zhang, S., Genov, D. A., Wang, Y., Liu, M. & Zhang, X. *Plasmon-induced transparency in metamaterials*. Physical Review Letters **101**, 4 047401 (2008).

[67] Davies, P. M. Z., Hamm, J. M., Sonnefraud, Y., Maier, S. A. & Hess, O. *Plasmonic Nanogap Tilings: Light-Concentrating Surfaces for Low-Loss Photonic Integration*. ACS Nano **7**, 8 7093 (2013).

[68] Anker, J. N., Hall, W. P., Lyandres, O., Shah, N. C., Zhao, J. & Van Duyne, R. P. *Biosensing with plasmonic nanosensors*. Nature materials **7**, 6 442 (2008).

[69] Zhang, X., Ma, X., Dou, F., Zhao, P. & Liu, H. *A biosensor based on metallic photonic crystals for the detection of specific bioreactions*. Advanced Functional Materials **21**, 22 4219 (2011).

[70] Utikal, T., Zentgraf, T., Tikhodeev, S. G., Lippitz, M. & Giessen, H. *Tailoring the photonic band splitting in metallodielectric photonic crystal superlattices*. Physical Review B **84**, 7 075101 (2011).

[71] Yariv, A., Xu, Y., Lee, R. K. & Scherer, A. *Coupled-resonator optical waveguide:?a proposal and analysis*. Opt. Lett. **24**, 11 711 (1999).

[72] Mookherjea, S. & Yariv, A. *Kerr-stabilized super-resonant modes in coupled-resonator optical waveguides*. Phys. Rev. E **66** 046610 (2002).

[73] Smith, D. D., Chang, H., Fuller, K. A., Rosenberger, A. T. & Boyd, R. W. *Coupled-resonator-induced transparency*. Phys. Rev. A **69** 063804 (2004).

[74] Scheuer, J., Paloczi, G. T., Poon, J. K. S. & Yariv, A. *Coupled Resonator Optical Waveguides: Toward the Slowing and Storage of Light*. Opt. Photon. News **16**, 2 36 (2005).

[75] Yanik, M. F. & Fan, S. *Stopping Light All Optically*. Phys. Rev. Lett. **92** 083901 (2004).

[76] Yanik, M. F. & Fan, S. *Stopping and storing light coherently*. Phys. Rev. A **71** 013803 (2005).

[77] Vlasov, Y., Green, W. M. J. & Xia, F. *High-throughput silicon nanophotonic wavelength-insensitive switch for on-chip optical networks*. Nat. Phot. **2** 242 (2008).

[78] Little, B., Chu, S., Absil, P., Hryniewicz, J., Johnson, F., Seiferth, F., Gill, D., Van, V., King, O. & Trakalo, M. *Very high-order microring resonator filters for WDM applications*. Photonics Technology Letters, IEEE **16**, 10 2263 (2004).

[79] Xia, F., Green, W. M. J. & Vlasov, Y. *Ultracompact optical buffers on a silicon chip*. Nat. Phot. **1** 65 (2006).

[80] Kurt, H. & Citrin, D. S. *Coupled-resonator optical waveguides for biochemical sensing of nanoliter volumes of analyte in the terahertz region*. Applied Physics Letters **87**, 24 241119 (2005).

[81] Morichetti, F., Ferrari, C., Canciamilla, A. & Melloni, A. *The first decade of coupled resonator optical waveguides: bringing slow light to applications*. Laser & Photonics Reviews **6**, 1 74 (2012).

[82] Maier, S. A., Kik, P. G. & Atwater, H. A. *Observation of coupled plasmon-polariton modes in Au nanoparticle chain waveguides of different lengths: Estimation of waveguide loss*. Applied Physics Letters **81**, 9 1714 (2002).

[83] Maier, S. A., Kik, P. G., Atwater, H. A., Meltzer, S., Harel, E., Koel, B. E. & Requicha, A. A. G. *Local detection of electromagnetic energy transport below the diffraction limit in metal nanoparticle plasmon waveguides*. Nat. Mat. **2** 229 (2003).

[84] Xu, Y., Li, Y., Lee, R. K. & Yariv, A. *Scattering-theory analysis of waveguide-resonator coupling*. Phys. Rev. E **62** 7389 (2000).

[85] Weiss, O. & Scheuer, J. *Side coupled adjacent resonators CROW - formation of mid-band zero group velocity*. Opt. Express **17**, 17 14817 (2009).

[86] Heebner, J. E., Boyd, R. W. & Park, Q.-H. *SCISSOR solitons and other novel propagation effects in microresonator-modified waveguides*. J. Opt. Soc. Am. B **19**, 4 722 (2001).

[87] E. Heebner, J., Boyd, R. W. & Park, Q.-H. *Slow light, induced dispersion, enhanced nonlinearity, and optical solitons in a resonator-array waveguide*. Phys. Rev. E **65** 036619 (2002).

[88] Yanik, M. F., Suh, W., Wang, Z. & Fan, S. *Stopping Light in a Waveguide with an All-Optical Analog of Electromagnetically Induced Transparency*. Phys. Rev. Lett. **93** 233903 (2004).

[89] Petrov, A. Y. & Eich, M. *Zero dispersion at small group velocities in photonic crystal waveguides*. Applied physics letters **85**, 21 4866 (2004).

[90] McMillan, J. F., Yang, X., Panoiu, N. C., Osgood, R. M. & Wong, C. W. *Enhanced stimulated Raman scattering in slow-light photonic crystal waveguides*. Optics letters **31**, 9 1235 (2006).

[91] Baba, T. *Slow light in photonic crystals*. Nature photonics **2**, 8 465 (2008).

[92] Kuramochi, E., Notomi, M., Hughes, S., Shinya, A., Watanabe, T. & Ramunno, L. *Disorder-induced scattering loss of line-defect waveguides in photonic crystal slabs*. Physical Review B **72**, 16 161318 (2005).

[93] Mookherjea, S., Park, J. S., Yang, S.-H. & Bandaru, P. R. *Localization in silicon nanophotonic slow-light waveguides*. Nature Photonics **2**, 2 90 (2008).

[94] Zhang, Z.-Q. *Light amplification and localization in randomly layered media with gain*. Physical Review B **52**, 11 7960 (1995).

[95] Fan, S. *Sharp asymmetric line shapes in side-coupled waveguide-cavity systems*. Applied Physics Letters **80**, 6 908 (2002).

[96] Momeni, B. & Adibi, A. *Adiabatic matching stage for coupling of light to extended Bloch modes of photonic crystals*. Applied Physics Letters **87**, 17 171104 (2005).

[97] Feng, L., Wong, Z. J., Ma, R.-M., Wang, Y. & Zhang, X. *Single-mode laser by parity-time symmetry breaking*. Science **346**, 6212 972 (2014).

[98] Bachiller, C., Gonzalez, H., Esbert, V., Martinez, A. & Morro, J. *Efficient Technique for the Cascade Connection of Multiple Two-Port Scattering Matrices*. Microwave Theory and Techniques, IEEE Transactions on **55**, 9 1880 (2007).

[99] Xu, Y., Lee, R. K. & Yariv, A. *Adiabatic coupling between conventional dielectric waveguides and waveguides with discrete translational symmetry*. Opt. Lett. **25**, 10 755 (2000).

[100] Melloni, A., Canciamilla, A., Ferrari, C., Morichetti, F., O'Faolain, L., Krauss, T., De La Rue, R., Samarelli, A. & Sorel, M. *Tunable delay lines in silicon photonics: coupled resonators and photonic crystals, a comparison*. Photonics Journal, IEEE **2**, 2 181 (2010).

[101] Goubau, G. *Surface Waves and Their Application to Transmission Lines*. Journal of Applied Physics **21**, 11 1119 (1950).

[102] Ulrich, R. & Tacke, M. *Submillimeter waveguiding on periodic metal structure*. Applied Physics Letters **22**, 5 251 (1973).

[103] Garcia-Vidal, F. J., Martn-Moreno, L. & Pendry, J. B. *Surfaces with holes in them: new plasmonic metamaterials*. Journal of Optics A: Pure and Applied Optics **7**, 2 S97 (2005).

[104] Qiu, M. *Photonic band structures for surface waves on structured metal surfaces*. Opt. Express **13**, 19 7583 (2005).

[105] Hendry, E., Hibbins, A. P. & Sambles, J. R. *Importance of diffraction in determining the dispersion of designer surface plasmons*. Phys. Rev. B **78** 235426 (2008).

[106] Shen, J. T., Catrysse, P. B. & Fan, S. *Mechanism for Designing Metallic Metamaterials with a High Index of Refraction*. Phys. Rev. Lett. **94** 197401 (2005).

[107] Maier, S. A., Andrews, S. R., Martín-Moreno, L. & García-Vidal, F. J. *Terahertz Surface Plasmon-Polariton Propagation and Focusing on Periodically Corrugated Metal Wires*. Phys. Rev. Lett. **97** 176805 (2006).

[108] Fernndez-Domnguez, A. I., Williams, C. R., Garca-Vidal, F. J., Martn-Moreno, L., Andrews, S. R. & Maier, S. A. *Terahertz surface plasmon polaritons on a helically grooved wire*. Applied Physics Letters **93**, 14 141109 (2008).

[109] Fernández-Domínguez, A. I., Moreno, E., Martín-Moreno, L. & García-Vidal, F. J. *Guiding terahertz waves along subwavelength channels*. Phys. Rev. B **79** 233104 (2009).

[110] Fernández-Domínguez, A. I., Moreno, E., Martín-Moreno, L. & García-Vidal, F. J. *Terahertz wedge plasmon polaritons*. Opt. Lett. **34**, 13 2063 (2009).

[111] Navarro-Cía, M., Beruete, M., Agrafiotis, S., Falcone, F., Sorolla, M. & Maier, S. A. *Broadband spoof plasmons and subwavelength electromagnetic energy confinement on ultrathin metafilms*. Opt. Express **17**, 20 18184 (2009).

[112] Martin-Cano, D., Quevedo-Teruel, O., Moreno, E., Martin-Moreno, L. & Garcia-Vidal, F. J. *Waveguided spoof surface plasmons with deep-subwavelength lateral confinement*. Opt. Lett. **36**, 23 4635 (2011).

[113] Zhu, W., Agrawal, A. & Nahata, A. *Planar plasmonic terahertz guided-wave devices*. Opt. Express **16**, 9 6216 (2008).

[114] Lockyear, M. J., Hibbins, A. P. & Sambles, J. R. *Microwave Surface-Plasmon-Like Modes on Thin Metamaterials*. Phys. Rev. Lett. **102** 073901 (2009).

[115] Zhao, W., Eldaiki, O. M., Yang, R. & Lu, Z. *Deep subwavelength waveguiding and focusing based on designer surface plasmons*. Opt. Express **18**, 20 21498 (2010).

[116] Williams, C. R., Misra, M., Andrews, S. R., Maier, S. A., Carretero-Palacios, S., Rodrigo, S. G., Garcia-Vidal, F. J. & Martin-Moreno, L. *Dual band terahertz waveguiding on a planar metal surface patterned with annular holes*. Applied Physics Letters **96**, 1 011101 (2010).

[117] Kim, S.-H., Kim, T.-T., Oh, S., Kim, J.-E., Park, H. & Kee, C.-S. *Experimental demonstration of self-collimation of spoof surface plasmons*. Phys. Rev. B **83** 165109 (2011).

[118] Brock, E. M. G., Hendry, E. & Hibbins, A. P. *Subwavelength lateral confinement of microwave surface waves*. Applied Physics Letters **99**, 5 051108 (2011).

[119] Jiang, T., Shen, L., Wu, J.-J., Yang, T.-J., Ruan, Z. & Ran, L. *Realization of tightly confined channel plasmon polaritons at low frequencies*. Applied Physics Letters **99**, 26 261103 (2011).

[120] Gan, Q., Fu, Z., Ding, Y. J. & Bartoli, F. J. *Ultrawide-Bandwidth Slow-Light System Based on THz Plasmonic Graded Metallic Grating Structures*. Phys. Rev. Lett. **100** 256803 (2008).

[121] Martin-Cano, D., Nesterov, M. L., Fernandez-Dominguez, A. I., Garcia-Vidal, F. J., Martin-Moreno, L. & Moreno, E. *Domino plasmons for subwavelengthterahertz circuitry*. Opt. Express **18**, 2 754 (2010).

[122] Huang, X.-R., Peng, R.-W. & Fan, R.-H. *Making Metals Transparent for White Light by Spoof Surface Plasmons*. Phys. Rev. Lett. **105** 243901 (2010).

[123] Liu, Y., Shi, H., Wang, C., Du, C. & Luo, X. *Multiple directional beaming effect of metallic subwavelength slit surrounded by periodically corrugated grooves*. Optics express **16**, 7 4487 (2008).

[124] Khanikaev, A. B., Mousavi, S. H., Shvets, G. & Kivshar, Y. S. *One-Way Extraordinary Optical Transmission and Nonreciprocal Spoof Plasmons*. Phys. Rev. Lett. **105** 126804 (2010).

[125] Wood, J. *Spoof SPPs and santed geometries*. Master's thesis, Imperial College London, UK (2011).

[126] Moharam, M. & Gaylord, T. *Rigorous coupled-wave analysis of planar-grating diffraction*. JOSA **71**, 7 811 (1981).

[127] Pendry, J. & MacKinnon, A. *Calculation of photon dispersion relations*. Physical Review Letters **69**, 19 2772 (1992).

[128] Whittaker, D. & Culshaw, I. *Scattering-matrix treatment of patterned multilayer photonic structures*. Physical Review B **60**, 4 2610 (1999).

[129] Lalanne, P. & Silberstein, E. *Fourier-modal methods applied to waveguide computational problems*. Optics Letters **25**, 15 1092 (2000).

[130] Galindo, V. & Wu, C. *Numerical solutions for an infinite phased array of rectangular waveguides with thick walls*. Antennas and Propagation, IEEE Transactions on **14**, 2 149 (1966).

[131] Tikhodeev, S. G., Yablonskii, A., Muljarov, E., Gippius, N. & Ishihara, T. *Quasiguided modes and optical properties of photonic crystal slabs*. Physical Review B **66**, 4 045102 (2002).

[132] Sauvan, C., Lecamp, G., Lalanne, P. & Hugonin, J. *Modal-reflectivity enhancement by geometry tuning in photonic crystal microcavities*. Optics Express **13**, 1 245 (2005).

[133] Li, L. & Haggans, C. W. *Convergence of the coupled-wave method for metallic lamellar diffraction gratings*. JOSA A **10**, 6 1184 (1993).

[134] Li, L. *Use of Fourier series in the analysis of discontinuous periodic structures*. JOSA A **13**, 9 1870 (1996).

[135] Li, L. *New formulation of the Fourier modal method for crossed surface-relief gratings*. JOSA A **14**, 10 2758 (1997).

[136] Popov, E. & Nevière, M. *Grating theory: new equations in Fourier space leading to fast converging results for TM polarization*. JOSA A **17**, 10 1773 (2000).

[137] Wang, B., Jiang, J. & Nordin, G. *Compact slanted grating couplers*. Optics express **12**, 15 3313 (2004).

[138] Wang, B., Jiang, J. & Nordin, G. P. *Embedded slanted grating for vertical coupling between fibers and silicon-on-insulator planar waveguides*. Photonics Technology Letters, IEEE **17**, 9 1884 (2005).

[139] Levola, T. & Laakkonen, P. *Replicated slanted gratings with a high refractive index material for in and outcoupling of light*. Optics express **15**, 5 2067 (2007).

[140] Bonod, N., Popov, E., Li, L. & Chernov, B. *Unidirectional excitation of surface plasmons by slanted gratings*. Optics express **15**, 18 11427 (2007).

[141] Wood, J. J., Tomlinson, L. A., Hess, O., Maier, S. A. & Fernández-Domínguez, A. I. *Spoof plasmon polaritons in slanted geometries*. Phys. Rev. B **85** 075441 (2012).

[142] Li, S., Jadidi, M. M., Murphy, T. E. & Kumar, G. *Terahertz surface plasmon polaritons on a semiconductor surface structured with periodic V-grooves*. Optics express **21**, 6 7041 (2013).

[143] Yuferev, S. V. & Ida, N. *Surface Impedance Boundary Conditions: A Comprehensive Approach* (CRC Press, 2009).

[144] de León-Pérez, F., Brucoli, G., García-Vidal, F. & Martín-Moreno, L. *Theory on the scattering of light and surface plasmon polaritons by arrays of holes and dimples in a metal film*. New Journal of Physics **10**, 10 105017 (2008).

[145] López-Tejeira, F., García-Vidal, F. & Martín-Moreno, L. *Scattering of surface plasmons by one-dimensional periodic nanoindented surfaces*. Physical Review B **72**, 16 161405 (2005).

[146] Rusina, A., Durach, M. & Stockman, M. *Theory of spoof plasmons in real metals*. Applied Physics A **100**, 2 375 (2010).

[147] Prade, B., Vinet, J. Y. & Mysyrowicz, A. *Guided optical waves in planar heterostructures with negative dielectric constant*. Phys. Rev. B **44** 13556 (1991).

[148] Bethe, H. *Theory of diffraction by small holes*. Physical Review **66**, 7-8 163 (1944).

[149] Roberts, A. *Electromagnetic theory of diffraction by a circular aperture in a thick, perfectly conducting screen*. JOSA A **4**, 10 1970 (1987).

[150] Thio, T., Pellerin, K., Linke, R., Lezec, H. & Ebbesen, T. *Enhanced light transmission through a single subwavelength aperture*. Optics Letters **26**, 24 1972 (2001).

[151] Lezec, H. J., Degiron, A., Devaux, E., Linke, R., Martin-Moreno, L., Garcia-Vidal, F. & Ebbesen, T. *Beaming light from a subwavelength aperture*. Science **297**, 5582 820 (2002).

[152] Bravo-Abad, J., García-Vidal, F. & Martín-Moreno, L. *Resonant transmission of light through finite chains of subwavelength holes in a metallic film*. Physical review letters **93**, 22 227401 (2004).

[153] Mei, S., Jie, T., Zhi-Yuan, L., Bing-Ying, C., Dao-Zhong, Z., Ai-Zi, J. & Hai-Fang, Y. *The role of periodicity in enhanced transmission through subwavelength hole arrays*. Chinese Physics Letters **23**, 2 486 (2006).

[154] Przybilla, F., Genet, C. & Ebbesen, T. *Enhanced transmission through Penrose subwavelength hole arrays*. Applied physics letters **89**, 12 121115 (2006).

[155] Coe, J. V., Heer, J. M., Teeters-Kennedy, S., Tian, H. & Rodriguez, K. R. *Extraordinary transmission of metal films with arrays of subwavelength holes*. Annu. Rev. Phys. Chem. **59** 179 (2008).

[156] Gordon, R., Sinton, D., Kavanagh, K. L. & Brolo, A. G. *A new generation of sensors based on extraordinary optical transmission*. Accounts of chemical research **41**, 8 1049 (2008).

[157] Sinton, D., Gordon, R. & Brolo, A. G. *Nanohole arrays in metal films as optofluidic elements: progress and potential*. Microfluidics and Nanofluidics **4**, 1-2 107 (2008).

[158] Hsu, S.-Y., Lee, M.-C., Lee, K.-L. & Wei, P.-K. *Extraction enhancement in organic light emitting devices by using metallic nanowire arrays*. Applied Physics Letters **92**, 1 013303 (2008).

[159] Collin, S., Pardo, F. & Pelouard, J.-L. *Resonant-cavity-enhanced subwavelength metal–semiconductor–metal photodetector*. Applied physics letters **83**, 8 1521 (2003).

[160] Hendry, E., Garcia-Vidal, F., Martin-Moreno, L., Rivas, J. G., Bonn, M., Hibbins, A. P. & Lockyear, M. J. *Optical control over surface-plasmon-polariton-assisted THz transmission through a slit aperture*. Physical review letters **100**, 12 123901 (2008).

[161] Dintinger, J., Robel, I., Kamat, P. V., Genet, C. & Ebbesen, T. W. *Terahertz All-Optical Molecule-Plasmon Modulation*. Advanced Materials **18**, 13 1645 (2006).

[162] Porto, J., Martin-Moreno, L. & Garcia-Vidal, F. *Optical bistability in subwavelength slit apertures containing nonlinear media*. Physical Review B **70**, 8 081402 (2004).

[163] Babicheva, V. E., Kulkova, I. V., Malureanu, R., Yvind, K. & Lavrinenko, A. V. *Plasmonic modulator based on gain-assisted metal–semiconductor–metal waveguide*. Photonics and Nanostructures-Fundamentals and Applications **10**, 4 389 (2012).

[164] Leosson, K. *Optical amplification of surface plasmon polaritons: review*. Journal of Nanophotonics **6**, 1 061801 (2012).

[165] Khurgin, J. B. *How to deal with the loss in plasmonics and metamaterials*. Nature nanotechnology **10**, 1 2 (2015).

[166] Kim, S.-H., Oh, S. S., Kim, K.-J., Kim, J.-E., Park, H. Y., Hess, O. & Kee, C.-S. *Subwavelength localization and toroidal dipole moment of spoof surface plasmon polaritons*. Physical Review B **91**, 3 035116 (2015).

[167] Marcatili, E. A. *Dielectric rectangular waveguide and directional coupler for integrated optics*. Bell System Technical Journal **48**, 7 2071 (1969).

Appendices

A Poyntings theorem

When considering the dispersion of the material for Poynting's theorem we follow the derivation of Jackson [31]. Poynting's theorem states that

$$-\frac{\partial u}{\partial t} = \nabla \cdot \mathbf{S} + \mathbf{J} \cdot \mathbf{E} \tag{A.1}$$

To calculate the energy from the FEM numerical simulation software we use the time-averaged values. Considering the spatial extent of the modes and fields it is necessary to integrate the fields over the total modal volume, V, which is bound by the surface S. By using Stoke's theorem we arrive at

$$-\int_V \left\langle \frac{\partial u}{\partial t} \right\rangle dV = \int_S \langle \mathbf{S} \rangle \cdot dS + \int_V \langle \mathbf{J} \cdot \mathbf{E} \rangle \, dV, \tag{A.2}$$

where all the fields are real. u is the energy density and is equal to

$$u = \mathbf{E} \cdot \frac{\partial \mathbf{D}}{\partial t} + \mathbf{H} \cdot \frac{\partial \mathbf{B}}{\partial t}. \tag{A.3}$$

Transforming the fields into the Fourier domain and assuming that we are dealing with linearly dispersive media we have from the constitutive relations that

$$\begin{aligned} \mathbf{D}(\mathbf{r}, \omega) &= \varepsilon(\omega)\mathbf{E}(\mathbf{r}, \omega), \\ \mathbf{B}(\mathbf{r}, \omega) &= \mu(\omega)\mathbf{H}(\mathbf{r}, \omega). \end{aligned} \tag{A.4}$$

Taking the electric part of the energy density we can rewrite

$$\begin{aligned} \mathbf{E}(\mathbf{r}, t) \cdot \frac{\partial \mathbf{D}(\mathbf{r}, t)}{\partial t} &= \int d\omega \mathbf{E}(\mathbf{r}, \omega) e^{-i\omega t} \cdot \frac{\partial}{\partial t} \int d\omega' \mathbf{E}(\mathbf{r}, \omega') e^{-i\omega' t}, \\ &= \int d\omega d\omega' (-i\omega') \varepsilon(\omega') \mathbf{E}(\mathbf{r}, \omega) \cdot \mathbf{E}(\mathbf{r}, \omega') e^{-i(\omega+\omega')t}. \end{aligned} \tag{A.5}$$

As $\mathbf{E}(\mathbf{r}, t) = \mathbf{E}^*(\mathbf{r}, t)$, i.e. the time-dependent fields (and material functions) are all real, $\mathbf{E}(\mathbf{r}, \omega)e^{-i\omega t}$ can be replaced with $\mathbf{E}^*(\mathbf{r}, \omega)e^{i\omega t}$. Due to the same condition we also have that $\mathbf{E}^*(\mathbf{r}, \omega) = \mathbf{E}(\mathbf{r}, -\omega)$. Thus the above expression can be altered to

$$\mathbf{E}(\mathbf{r}, t) \cdot \frac{\partial \mathbf{D}(\mathbf{r}, t)}{\partial t} = \int d\omega d\omega' (-i\omega')\varepsilon(\omega')\mathbf{E}^*(\mathbf{r}, \omega) \cdot \mathbf{E}(\mathbf{r}, \omega')e^{-i(\omega-\omega')t}. \tag{A.6}$$

By splitting the integral in two and letting ω, $\omega' \to -\omega'$, $-\omega$ this can be rearrange further to

$$\mathbf{E}(\mathbf{r}, t) \cdot \frac{\partial \mathbf{D}(\mathbf{r}, t)}{\partial t} = \frac{1}{2} \int d\omega d\omega' \mathbf{E}^*(\mathbf{r}, \omega') \cdot \mathbf{E}(\mathbf{r}, \omega) \left[(-i\omega)\varepsilon(\omega) + i\omega'\varepsilon(\omega')\right]. \tag{A.7}$$

Assuming that the relevant electric field terms are contained in a relatively small frequency range (around ω_0), over which $\varepsilon(\omega)$ does not vary significantly, we can expand the term $i\omega'\varepsilon^*(\omega')$ via a Taylor series around the point ω yielding that

$$i\omega'\varepsilon(\omega') \approx i\omega\varepsilon(\omega)^*\varepsilon(\omega') + \frac{d}{d\omega}(i\omega\varepsilon^*(\omega))(\omega' - \omega) \tag{A.8}$$

And therefore

$$\begin{aligned}(-i\omega)\varepsilon(\omega) + i\omega'\varepsilon(\omega') &\approx i\omega(\varepsilon^*(\omega) - \varepsilon(\omega)) - + \frac{d}{d\omega}(i\omega\varepsilon^*(\omega)) \\ &= 2\omega \mathrm{Im}[\varepsilon(\omega)] - i(\omega - \omega')\frac{d}{d\omega}(\omega\varepsilon^*(\omega))\end{aligned} \tag{A.9}$$

Ultimately this allows the rate of change of the electric component of the energy density to be re-formulated as:

$$\begin{aligned}\mathbf{E}(\mathbf{r}, t) \cdot \frac{\partial \mathbf{D}(\mathbf{r}, t)}{\partial t} = &\int d\omega d\omega' \omega \mathrm{Im}[\varepsilon(\omega)]\mathbf{E}^*(\mathbf{r}, \omega') \cdot \mathbf{E}^*(\mathbf{r}, \omega)e^{-i(\omega-\omega')t} \\ &+ \frac{1}{2}\frac{\partial}{\partial t} \int d\omega d\omega' \left[\frac{d}{dx}(x\varepsilon^*(x))\right]_{x=\omega} \mathbf{E}^*(\mathbf{r}, \omega') \cdot \mathbf{E}^*(\mathbf{r}, \omega)e^{-i(\omega-\omega')t}\end{aligned} \tag{A.10}$$

The first term in the equation is the energy dissipated by the material due to the fact that the permittivity has an imaginary component. As we are treating the metal as a dielectric there is no free current and hence $\mathbf{J}$ in equation A.1 is equal to zero. However, there is still energy dissipated/absorbed by the material. The second part is our amended rate of change of the electric energy density for linearly dispersive media. Note that in the limit ε is real and dispersion-less it recovers precisely the standard result of $\mathbf{E}(\mathbf{r}, t) \cdot \partial \mathbf{D}(\mathbf{r}, t)/\partial t = \varepsilon_0 |\mathbf{E}|^2/2$. Taking the time average

yields

$$\left\langle \mathbf{E}(\mathbf{r},t)\cdot\frac{\partial \mathbf{D}(\mathbf{r},t)}{\partial t}\right\rangle = \omega_0 \mathrm{Im}[\varepsilon(\omega_0)]\left\langle \mathbf{E}(\mathbf{r},t)\cdot\mathbf{E}(\mathbf{r},t)\right\rangle + \frac{\partial}{\partial t}\frac{1}{2}\mathrm{Re}\left[\frac{d(\varepsilon(\omega)\omega)}{d\omega}\right]_{\omega_0}\left\langle \mathbf{E}(\mathbf{r},t)\cdot\mathbf{E}(\mathbf{r},t)\right\rangle, \quad \text{(A.11)}$$

where we have assumed $\varepsilon(\omega)$ to be the permittivity of a Drude type metal. A similar expression can be derived for the magnetic term in equation (A.3). Thus, after taking the time averages of the fields we find that equation (A.2) becomes (for a Drude type metal, with no magnetic response)

$$U = R + D \quad \text{(A.12)}$$

where U, R and D correspond to the energy stored within the system, the energy radiated from the system and the energy dissipated by the system respectively. They are defined as

$$U = 2\mathrm{Im}[\omega_0]\int_V \left[\frac{\mu_0|\mathbf{H}|^2}{4} + \frac{\varepsilon_0 \mathrm{Re}[\varepsilon(\omega_0)]|\mathbf{E}|^2}{4} + \frac{\varepsilon_0|\mathbf{E}|^2}{4}\frac{\omega_p^2(2\omega_0 + i\gamma)}{\omega_0(\omega_0+i\gamma)^2}\right] dV, \quad \text{(A.13)}$$

$$R = -\int_S \frac{\mathrm{Re}[\mathbf{E}\times\mathbf{H}^*}{2}]dS, \quad \text{(A.14)}$$

$$D = -\omega_0\int_V \mathrm{Im}[\varepsilon(\omega_0)]\frac{1|\mathbf{E}|^2}{2}dV. \quad \text{(A.15)}$$

Finally, the proportion of the energy lost to each decay channel is given by the relevant ratios

$$\gamma_r = \mathrm{Im}[\omega_0]\frac{R}{U}, \quad \text{(A.16)}$$

$$\gamma_d = \mathrm{Im}[\omega_0]\frac{D}{U}, \quad \text{(A.17)}$$

$$\quad \text{(A.18)}$$

where γ_r and γ_d are the radiative and dissipative decay rates.

B Mode hybridisation theory: two waveguide modes

As before, each cut-wire resonator is treated as a harmonic oscillator (p) driven by the a time harmonic electric field, in this case the sum of two waveguide modes, thus

$$\ddot{p} + \gamma\dot{p} + \omega_0^2 p = g_1 E_1 e^{-i\omega t} + g_2 E_2 e^{-i\omega t}, \tag{B.1}$$

where g_1 and g_2 are the coupling of each waveguide mode to the oscillator. Solving for the oscillator p we find that

$$p = \frac{g_1 E_1 + g_2 E_2}{\omega_0^2 - \omega^2 - i\gamma\omega} e^{-i\omega t}. \tag{B.2}$$

Now let us split the losses into three channels, $\gamma \rightarrow \gamma' + \kappa_1 + \kappa_2$ where $\kappa_{1,2}$ are the decays into the 1st and 2nd order waveguide modes. As the scattered electric field is related to the oscillator through $g_m E_s = -\kappa_m \dot{p}$ we find that the field scattered into each waveguide mode is

$$g_m E_s = g_m \left(\frac{i\kappa_m \omega}{\omega_0^2 - \omega^2 - i\gamma\omega} E_m + \frac{g_n}{g_m} \frac{i\kappa_n \omega}{\omega_0^2 - \omega^2 - i\gamma\omega} E_n \right) e^{-i\omega t} \quad = g_m (r_{mm} E_m + r_{mn} E_n) e^{-i\omega t}, \tag{B.3}$$

where m and n are equal to either 1 and 2 or 2 and 1. Thus, r_{mn} is the reflection of waveguide mode m onto waveguide mode n via the cut wire resonator. As the field is scattered into both directions equally we find that $t_{nn} = 1 + r_{nn}$ and that $t_{nm} = r_{nm}$. Now that we have all of our scattering coefficients we can construct the transfer matrix to propagate the fields through the unit cell. The waveguide modes $A_n^{(1)}$, $A_n^{(2)}$, $B_{n+1}^{(1)}$ and $B_{n+1}^{(2)}$ enter the unit cell from the left and right, where the A and B depict forwards and backwards propagating modes and the superscripts 1 and 2 list the order of the waveguide mode. They propagate towards the cut-wire acquiring a phase dependent on their waveguide mode order, $\exp(ik_{wg}^{(1)} d/2)$ and $\exp(ik_{wg}^{(2)} d/2)$, where $k_{wg}^{(n)} = n_{eff}^{(m)} \omega / c$ and $n_{eff}^{(m)}$ is the effective index of the slab for waveguide mode m. Once they reach the cut-wire the fields are

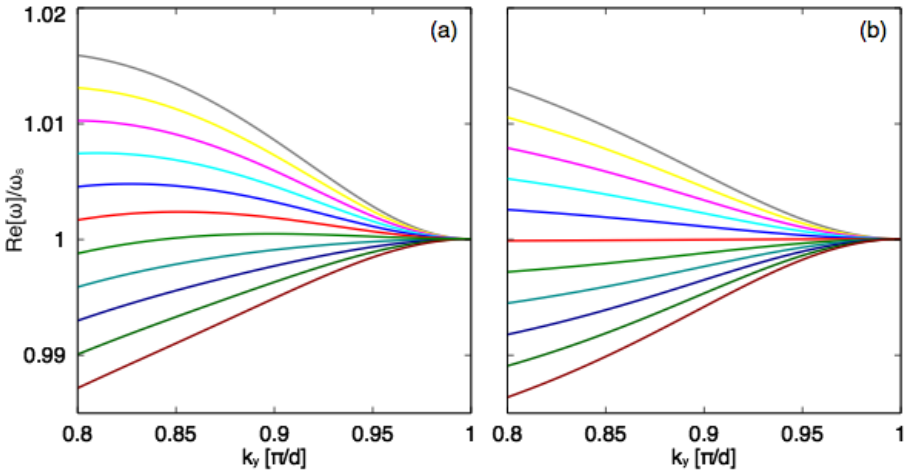

Figure B.1: Comparison of the dispersion relations calculated using (a) two waveguide modes - equation (B.5) and (b) one waveguide mode - equation (4.5) for a range of different cut-wires resonances, ranging from $\omega_0 = 0.975\omega_s$ (dark red line) to $\omega_0 = 1.025\omega_s$ (grey line), at intervals of $0.005\omega_s$

either reflected, transmitted or absorbed within the losses of the resonator. Finally the waveguide modes acquire anther phase of $\exp(ik_{wg}^{(m)}d/2)$ before exciting the unit cell as modes $A_{n+1}^{(1)}$, $A_{n+1}^{(2)}$, $B_n^{(1)}$ and $B_n^{(2)}$. Writing this in matrix form we have

$$\begin{pmatrix} A_{n+1}^{(1)} \\ B_{n+1}^{(1)} \\ A_{n+1}^{(2)} \\ B_{n+1}^{(2)} \end{pmatrix} = \frac{1}{t'} \begin{pmatrix} (1-r_{11})e^{2u} & -r_{11} & -r_{21}e^{u+v} & -r_{21}e^{u-v} \\ r_{11} & (1+r_{11})e^{-2u} & r_{21}e^{-(u-v)} & r_{21}e^{-(u+v)} \\ -r_{12}e^{u+v} & -r_{12}e^{u-v} & (1-r_{22})e^{2v} & -r_{22} \\ r_{12}e^{-(u-v)} & r_{12}e^{-(u+v)} & r_{22} & (1+r_{22})e^{-2v} \end{pmatrix} \begin{pmatrix} A_n^{(1)} \\ B_n^{(1)} \\ A_n^{(2)} \\ B_n^{(2)} \end{pmatrix}, \tag{B.4}$$

where $u = ik_{wg}^{(1)}d/2$, $v = ik_{wg}^{(2)}d/2$ and $t' = 1 - t_{11} - t_{22}$. Applying the Bloch bound conditions that $A_{n+1}^{(i)} = A_n^{(i)}\exp(ik_y d)$ and $B_{n+1}^{(i)} = B_n^{(i)}\exp(ik_y d)$ allows us to calculate the dispersion relation as:

$$\begin{aligned} (\cos[k_y d] - \cos[k_{wg}^{(2)}d])(\cos[k_y d] - \cos[k_{wg}^{(1)}d] + i\frac{r_{11}}{t'}\sin[k_{wg}^{(1)}d]) \\ = i\frac{r_{22}}{t'}(\cos[k_y d] - \cos[k_{wg}^{(1)}d])\sin[k_{wg}^{(2)}d] \end{aligned}, \tag{B.5}$$

where once again we can use this to fit our results by varying the harmonic oscillator parameters. Interestingly, the coupling terms g_n do not appear in the dispersion relation, and although we have introduced a new rate, κ_2, this must still remain part of the resonator losses. Importantly this model

also recovers the previous dispersion in the limit that $\kappa_2 \to 0$ as the right hand side of equation (B.5) $\to 0$.

An example of the dispersion relations that can be modeled by this dispersion relation is shown in figure B.1 (a). For comparison those with only a single waveguide mode are shown in figure B.1 (b). From the figure it is clear that only when the second waveguide modes are included do the dispersion relations reproduce the proper curvature of the central CROW mode, and importantly it cannot produce a band that is flat across the whole FBZ. Thus, the theory of mode hybridisation with two waveguide modes reproduces the bands in the same shape as figure 4.5.

C Overlap integrals

In this Appendix the explicit overlap integrals that are needed to solve the spoof SPP master equations are given, as are there approximate form under the assumption that the wavelength is much greater than the groove width

C.1 Straight grooves

The two overlap integrals from equation (5.5) are S_{nm} and T_{mm} and they are defined as

$$\begin{aligned} S_{nm} &= \int_{-a/2}^{a/2} \phi_n^*(x)\chi_m(x)dx = \sqrt{\frac{2-\delta_{m0}}{ad}} \int_{-a/2}^{a/2} e^{-ik_n x}\cos(q_m(x+a/2))dx, \\ &= \sqrt{\frac{2-\delta_{m0}}{ad}} \frac{ik_n}{k_n^2 - q_m^2} \left[e^{-ik_n a/2} - (-1)^m e^{ik_n a/2} \right], \end{aligned} \tag{C.1}$$

and

$$\begin{aligned} T_{mm'} &= \int_{-a/2}^{a/2} \chi_{m'}^*(x)\chi_m(x)dx, \\ &= \sqrt{\frac{(2-\delta_{m0})(2-\delta_{m'0})}{a^2}} \int_{-a/2}^{a/2} \cos(q_m(x+a/2))\cos(q_{m'}(x+a/2))dx = \delta_{mm'}. \end{aligned} \tag{C.2}$$

Finally we also have that $S_{nm} = S_{nm}^*$. Under the assumption that $\lambda >> a$ the overlap integrals $S_{nm} \approx \sqrt{a/d}$, allowing equation (5.5) to be rearranged as the explicit dispersion relation, equation (5.8).

C.2 Slanted grooves

The overlap integrals that form equation (5.13), the slanted spoof SPP master equation, are defined as

$$
\begin{aligned}
S_{nm} &= \int_{-a\sec\theta/2}^{a\sec\theta/2} \phi_n(x)\chi_m^*(x\cos\theta)\cos\theta dx, \\
&= \sqrt{\frac{2-\delta_{m0}}{ad}}\cos\theta \int_{-a\sec\theta/2}^{a\sec\theta/2} e^{-ik_n x}\cos(q_m(\cos\theta x + a/2))dx, \\
&= \sqrt{\frac{2-\delta_{m0}}{ad}}\frac{i\cos\theta}{kn^2 - q_m^2\cos^2\theta}\left[e^{-ik_n\sec\theta a/2} - (-1)^m e^{ik_n\sec\theta a/2}\right],
\end{aligned}
\tag{C.3}
$$

$$
\begin{aligned}
X_{nm} &= \frac{1}{\sin(p_m h)}\int_{-a\sec\theta/2}^{a\sec\theta/2} \phi_n^*(x)\sin(p_m(h-\sin\theta x))\chi_m(x\cos\theta)dx, \\
&= \frac{1}{\sin(p_m h)}\sqrt{\frac{2-\delta_{m0}}{ad}}\int_{-a\sec\theta/2}^{a\sec\theta/2} e^{-ik_n x}\sin(p_m(h-\sin\theta x)\cos(q_m(\cos\theta x + a/2))dx, \\
&= \frac{1}{\sin(p_m h)}\sqrt{\frac{2-\delta_{m0}}{ad}}\left[e^{ik_n\sec\theta a/2}\left(\frac{(p_m\sin\theta - q_m\cos\theta)\cos(p_m h_l) - ik_n\sin(p_m h_l)}{k_n^2 - (p_m\sin\theta - q_m\cos\theta)^2}\right.\right. \\
&+ \left.\frac{(p_m\sin\theta + q_m\cos\theta)\cos(p_m h_l) - ik_n\sin(p_m h_l)}{k_n^2 - (p_m\sin\theta + q_m\cos\theta)^2}\right) \\
&- (-1)^m e^{-ik_n\sec\theta a/2}\left(\frac{(p_m\sin\theta - q_m\cos\theta)\cos(p_m h_s) - ik_n\sin(p_m h_s)}{k_n^2 - (p_m\sin\theta - q_m\cos\theta)^2}\right. \\
&+ \left.\left.\frac{(p_m\sin\theta + q_m\cos\theta)\cos(p_m h_s) - ik_n\sin(p_m h_s)}{k_n^2 - (p_m\sin\theta + q_m\cos\theta)^2}\right)\right],
\end{aligned}
\tag{C.4}
$$

$$
\begin{aligned}
Z_{nm} &= \frac{\eta_m Y_m^{\mathrm{II}}}{\sin(p_m h)}\int_{-a\sec\theta/2}^{a\sec\theta/2} \phi_n^*(x)\cos(p_m(h-\sin\theta x))\chi_m(x\cos\theta)\tan(q_m(x\cos\theta + a/2))dx, \\
&= \frac{\eta_m Y_m^{\mathrm{II}}}{\sin(p_m h)}\sqrt{\frac{2-\delta_{m0}}{ad}}\int_{-a\sec\theta/2}^{a\sec\theta/2} e^{-ik_n x}\cos(p_m(h-\sin\theta x)\sin(q_m(\cos\theta x + a/2))dx, \\
&= \frac{\eta_m Y_m^{\mathrm{II}}}{\sin(p_m h)}\sqrt{\frac{2-\delta_{m0}}{ad}}\left[(-1)^m e^{-ik_n\sec\theta a/2}\left(\frac{(q_m\cos\theta - p_m\sin\theta)\cos(p_m h_s) + ik_n\sin(p_m h_s)}{k_n^2 - (q_m\cos\theta - p_m\sin\theta)^2}\right.\right. \\
&+ \left.\frac{(p_m\sin\theta + q_m\cos\theta)\cos(p_m h_s) - ik_n\sin(p_m h_s)}{k_n^2 - (p_m\sin\theta + q_m\cos\theta)^2}\right) \\
&- e^{ik_n\sec\theta a/2}\left(\frac{(q_m\cos\theta - p_m\sin\theta)\cos(p_m h_l) + ik_n\sin(p_m h_l)}{k_n^2 - (q_m\cos\theta - p_m\sin\theta)^2}\right. \\
&+ \left.\left.\frac{(p_m\sin\theta + q_m\cos\theta)\cos(p_m h_s) - ik_n\sin(p_m h_s)}{k_n^2 - (p_m\sin\theta + q_m\cos\theta)^2}\right)\right],
\end{aligned}
\tag{C.5}
$$

and

$$\begin{aligned}
T_{mm'} &= \int_{-a\sec\theta/2}^{a\sec\theta/2} \chi_m(x\cos\theta)\cos(p'_m(h-\sin\theta x))\chi^*_m(x\cos\theta)\cos\theta dx, \\
&= \cos\theta\frac{\sqrt{(2-\delta_{m0})(2-\delta_{m'0})}}{a} \\
&\times \int_{-a\sec\theta/2}^{a\sec\theta/2} \cos(q_m(x\cos\theta+a/2))\cos(p'_m(h-\sin\theta x))\cos(q_{m'}(x\cos\theta+a/2))dx \\
&= \frac{p_{m'}\sin\theta\cos\theta\sqrt{(2-\delta_{m0})(2-\delta_{m'0})}\left(\sin(p_{m'}h_s)(-1)^{m+m'}-\sin(p_{m'}h_l)\right)}{a((q_m+q_{m'})^2\cos^2\theta-p^2_{m'}\sin^2\theta)} \\
&\times \frac{((q^2_m+q^2_{m'})\cos^2\theta-p^2_{m'}\sin^2\theta)}{((q_m-q_{m'})^2\cos^2\theta-p^2_{m'}\sin^2\theta)},
\end{aligned} \tag{C.6}$$

where h_s and h_l are the lengths of the longer and shorter side of the rotated groove respectively. They are given as

$$\begin{aligned}
h_s &= h-\frac{a\tan\theta}{2}, \\
h_l &= h+\frac{a\tan\theta}{2}.
\end{aligned} \tag{C.7}$$

Within the assumption that $\lambda \gg a$ the lowest order overlap integrals become $S_{00} \approx \sqrt{a/d}$, $X_{00} \approx \sqrt{a/d}\sec\theta$, $Z_{00} = 0$ and $T_{00} = \mathrm{sinc}[k_0 a\tan\theta/2]$. Thus equation (5.13) can be transformed into equation (5.15).

C.3 Real metal grooves

The overlap integrals given by equations (7.17), (7.18) and (7.19) are

$$\int_{-d/2}^{-a/2}\phi^*_n\chi^-_m dx = \frac{\chi_m(-a/2)}{\sqrt{d}}\left(\frac{e^{ik_n a/2}-e^{ik_n d/2}e^{-\alpha_m(d-a)/2}}{\alpha_m-ik_n}\right), \tag{C.8}$$

$$\int_{-a/2}^{a/2}\phi^*_n\chi_m dx = \frac{1}{\sqrt{ad}}\left[\frac{\sin((q_m-k_n)a/2)}{q_m-k_n}+(-1)^{\sigma_m}\frac{\sin((q_m+k_n)a/2)}{q_m+k_n}\right], \tag{C.9}$$

$$\int_{a/2}^{d/2}\phi^*_n\chi^+_m dx = \frac{\chi_m(a/2)}{\sqrt{d}}\left(\frac{e^{-ik_n a/2}-e^{-ik_n d/2}e^{-\alpha_m(d-a)/2}}{\alpha_m+ik_n}\right), \tag{C.10}$$

$$\int_{-d/2}^{-a/2}\phi_n\chi^{-*}_m dx = \frac{\chi_m(a/2)}{\sqrt{d}}\left(\frac{e^{-ik_n a/2}-e^{-ik_n d/2}e^{-\alpha_m(d-a)/2}}{\alpha_m+ik_n}\right), \tag{C.11}$$

$$\int_{a/2}^{d/2}\phi_n\chi^{+*}_m dx = \frac{\chi_m(-a/2)}{\sqrt{d}}\left(\frac{e^{ik_n a/2}-e^{ik_n d/2}e^{-\alpha_m(d-a)/2}}{\alpha_m-ik_n}\right), \tag{C.12}$$

$$\int_{-d/2}^{-a/2} \chi^{*}_{m'} \chi_m dx = \frac{1}{a} \begin{cases} \frac{sin((q_m - q_{m'})a/2)}{q_m - q_{m'}} + (-1)^m \frac{sin((q_m + q_{m'})a/2)}{q_m + q_{m'}}, & \text{for } (-1)^{m+m'} = 1 \\ 0, \quad \text{otherwise} \end{cases}, \tag{C.13}$$

$$\int_{a/2}^{d/2} \chi^{+*}_{m'} \chi^{+}_{m} dx = \chi_m(-a/2)\chi_{m'}(a/2) \frac{1 - e^{-(\alpha_m + \alpha_{m'})(d-a)/2}}{\alpha_m + \alpha_{m'}}, \tag{C.14}$$

$$\int_{-a/2}^{a/2} \chi^{*-}_{m'} \chi^{-}_{m} dx = \chi^{-}_{m}(a/2)\chi_{m'}(-a/2) \frac{1 - e^{-(\alpha_m + \alpha_{m'})(d-a)/2}}{\alpha_m + \alpha_{m'}}. \tag{C.15}$$

To find equation (6.20) we assume that the fields are concentrated within the groove and thus we can ignore the integrals given by equations (C.8), (C.9-12) and (C.14-15). Under the assumption that $\lambda \gg a$, equation (C.9) $\approx \sqrt{a/d}$ and equation (C.12) ≈ 1. Using this it is possible to rearrange equation (6.13) to find equation (6.20).

AMERICAN PHYSICAL SOCIETY LICENSE TERMS AND CONDITIONS

Dec 15, 2015

This Agreement between John Wood ("You") and American Physical Society ("American Physical Society") consists of your license details and the terms and conditions provided by American Physical Society and Copyright Clearance Center.

License Number	3765140265321
License date	Dec 09, 2015
Licensed Content Publisher	American Physical Society
Licensed Content Publication	Physical Review B
Licensed Content Title	Spoof plasmon polaritons in slanted geometries
Licensed Content Author	J. J. Wood et al.
Licensed Content Date	Feb 29, 2012
Licensed Content Volume Number	85
I would like to...	Thesis/Dissertation
Requestor type	Student
Format	Print, Electronic
Portion	chart/graph/table/figure
Number of charts/graphs/tables/figures	1
Portion description	Figure 4
Rights for	Main product
Duration of use	Life of current edition
Creation of copies for the disabled	no
With minor editing privileges	no
For distribution to	Worldwide
In the following language(s)	Original language of publication
With incidental promotional use	no
The lifetime unit quantity of new product	0 to 499
The requesting person/organization is:	John Wood
Order reference number	None
Title of your thesis / dissertation	Theory of surface modes in structured plasmonic arrays
Expected completion date	Dec 2015
Expected size (number of pages)	150
Requestor Location	John Wood 24 Milan House None None St Albans, United Kingdom AL1 3NT Attn: John J Wood
Billing Type	Invoice

Billing Address	John J Wood 24 Milan House None None St Albans, United Kingdom AL1 3NT Attn: John J Wood
Total	**0.00 GBP**
Total	**0.00 GBP**

Terms and Conditions

Terms and Conditions

The American Physical Society (APS) is pleased to grant the Requestor of this license a non-exclusive, non-transferable permission, limited to [**print** and/or **electronic** format, depending on what they chose], provided all criteria outlined below are followed.

1. For electronic format permissions, Requestor agrees to provide a hyperlink from the reprinted APS material using the source material's DOI on the web page where the work appears. The hyperlink should use the standard DOI resolution URL, http://dx.doi.org/{DOI}. The hyperlink may be embedded in the copyright credit line.
2. For print format permissions, Requestor agrees to print the required copyright credit line on the first page where the material appears: "Reprinted (abstract/excerpt/figure) with permission from [(FULL REFERENCE CITATION) as follows: Author's Names, APS Journal Title, Volume Number, Page Number and Year of Publication.] Copyright (YEAR) by the American Physical Society."
3. Permission granted in this license is for a one-time use and does not include permission for any future editions, updates, databases, formats or other matters. Permission must be sought for any additional use.
4. Use of the material does not and must not imply any endorsement by APS.
5. Under no circumstance does APS purport or intend to grant permission to reuse materials to which it does not hold copyright. It is the requestors sole responsibility to ensure the licensed material is original to APS and does not contain the copyright of another entity, and that the copyright notice of the figure, photograph, cover or table does not indicate that it was reprinted by APS, with permission from another source.
6. The permission granted herein is personal to the Requestor for the use specified and is not transferable or assignable without express written permission of APS. This license may not be amended except in writing by APS.
7. You may not alter, edit or modify the material in any manner.
8. You may translate the materials only when translation rights have been granted.
9. You may not use the material for promotional, sales, advertising or marketing purposes.
10. The foregoing license shall not take effect unless and until APS or its agent, Copyright Clearance Center (CCC), receives payment in full in accordance with CCC Billing and Payment Terms and Conditions, which are incorporated herein by reference.
11. Should the terms of this license be violated at any time, APS or CCC may revoke the license with no refund to you and seek relief to the fullest extent of the laws of the USA. Official written notice will be made using the contact information provided with the permission request. Failure to receive such notice will not nullify revocation of the permission.
12. APS reserves all rights not specifically granted herein.
13. This document, including the CCC Billing and Payment Terms and Conditions, shall be the entire agreement between the parties relating to the subject matter hereof.

Other Terms and Conditions